© 2018

Sruthi Murlidaran

ALL RIGHTS RESERVED

MECHANISMS UNDERLYING EFFECTS OF GENETIC VARIANCE AND GENERAL ANESTHETICS ON PENTAMERIC LIGAND GATED ION CHANNELS.

BY

SRUTHI MURLIDARAN

A dissertation submitted to the
Graduate School—Camden
Rutgers, The State University of New Jersey
in partial fulfillment of the requirements
for the degree of
Doctor of Philosophy
Graduate Program in Computational And Integrative Biology

Written under the direction of
Dr Grace Brannigan
and approved by

Dr Grace Brannigan

Dr Joseph Martin

Dr Hao Zhu

Dr Vincenzo Carnevale

Camden, New Jersey
May 2018

ABSTRACT OF THE DISSERTATION

Mechanisms underlying effects of genetic variance and general anesthetics on Pentameric Ligand Gated Ion channels.

by SRUTHI MURLIDARAN

Dissertation Director:
Dr Grace Brannigan

Two main projects involving molecular dynamics simulation of $\mathrm{GABA_AR}$ and a collaborative project involving simulations of GLIC receptor are presented in this thesis. The first project involves analyzing and comparing the conformational and functional changes between WT and K289M $\mathrm{GABA_AR}$ receptor. The second project involves calculating binding affinity for propofol, an intravenous anesthetic, at sites identified experimentally and verified using MD simulations in $\mathrm{GABA_AR}$ receptor. With comparatively lesser experimental knowledge for binding sites of sevoflurane, we use flooding simulation in addition to MD simulations to find exact binding sites and understand the pathway of binding. The third project involved running MD simulations of a prokaryotic pLGIC, GLIC,a bacterial proton-gated homolog, to understand how the lipid-facing M4 helix modulates channel function.

Pentameric ligand-gated ion channels mediate chemical transmission of nerve signals, when an agonist binds the ECD of the channel, leading to pore opening in the TMD. While various crystal structure of these channels has provided extensive information regarding the neurotransmitter binding sites, open/close conformations, it is still challenging to understand the microscopic interaction that drives this allosteric transition between the ECD to TMD. Molecular dynamics is an effective technique in guiding us to take a closer look at the residue level interactions. Using MD, we show how the difference in electrostatic interactions at the ECD-TMD in $\mathrm{GABA_A R}$ interface causes the channel to open in case of the WT and destabilize the open state in case of the K289M. Similar computational approaches reveal lipid penetration disrupting the interactions within the TMD helices of the 5ALA-GLIC mutant receptor which validates the reduced channel function in these receptors, as identified by experimentalists. In addition to traditional MD simulations, biased computational techniques, like AFEP helped us isolate putative binding sites, and quantify and rank binding affinities for two commonly used intravenous (Propofol) and inhalational (Sevoflurane) anesthetic, that has experimentally shown to target $\mathrm{GABA_A R}$ receptors. Furthermore, we are able to compare and explain the protein-anesthetic interactions that cause their affinities to different binding sites in the receptor.

Acknowledgements

Firstly, I would like to express my sincere gratitude to my advisor Prof. Dr Grace Brannigan for the continuous support of my Ph.D study, for her patience, thoughtfulness, motivation, and immense knowledge. Her guidance helped me in all the time of research and writing of this thesis. I could not have imagined having a better advisor and mentor for my Ph.D study.

Besides my advisor, I also thank Dr Jerome Henin and Dr Reza Salari for providing excellent guidance in all my projects, and Dr John Baezinger, and Dr. Roderic Eckenhoff for sharing their experimental results and providing me with an opportunity to validate their findings computationally.

My sincere thanks also goes to the rest of my thesis committee: Prof. Dr Joseph Martin, Prof. Dr Hao Zhu, and Prof. Dr Vincenzo Carnevale, for their insightful comments and encouragement that helped me widen my research from various perspectives.

I thank my fellow labmates, Ruchi Lohia, Liam Sharp for all the stimulating discussions and the fun we have had in the last six years.

Last but not the least, I would like to thank my family for their encouraging and reassuring words throughout my PhD study and my life in general and Mani for his constant support throughout the final and the most difficult phase of my study.

Dedication

To my parents and all my teachers who instilled in me, the love for science at a very young age.

Table of Contents

Abstract ii

Acknowledgements iv

Dedication v

List of Figures viii

1. Introduction 1

2. Physical Accuracy Leads to Biological Relevance: Best Practices For Simulating Ligand-Gated Ion Channels Interacting With General Anesthetics. 7

2.1. Abstract 7

2.2. Introduction 8

2.3. Material and Methods 13

2.4. Results and Dicussion 17

2.5. Conclusion 26

2.6. Supporting Methods 29

2.7. Supporting Theory 32

3. Physical Accuracy Leads to Biological Relevance: Best Practices For Simulating Ligand-Gated Ion Channels Interacting With General Anesthetics. 48

3.1. Abstract 48

3.2. Introduction 48

3.3. MD simulation involving pLGICs 49
3.4. Discovery of Candidate Sites 51
3.5. Calculation of Binding Affinities 68
3.6. Summary 74

4. Relative affinities of general anesthetics for pseudo-symmetric intersubunit binding sites of heteromeric GABA(A) receptors . . 76

4.1. Abstract 76
4.2. Introduction 77
4.3. Results 79
4.4. Conclusion 89

Appendix 91

.1. Appendix A: Role of the Fourth Transmembrane a Helix in the Allosteric Modulation of Pentameric Ligand-Gated Ion Channels . 91
.2. Appendix B: A novel bifunctional alkylphenol anesthetic allows characterization of GABA_AR subunit binding selectivity in synaptosomes. 107

Bibliography 122

List of Figures

1.1. **Structure of pentameric Ligand-gated Ion Channel** 4

2.1. **$\mathrm{GABA_AR}$ pore with relevant multibody interactions.** . . . 11

2.2. **Evolution of the interfacial band and pore oscillator in one replica of the WT system at 315K.** 15

2.3. **Evolution of pore oscillator and interfacial band during spontaneous opening event.** 19

2.4. **Correlations between shape of interfacial band, pore radius, and salt-bridging between interfacial band and pore oscillator for multiple replicas and temperatures.** 22

2.5. **Potential of mean force** 23

2.6. **Theory variables** 34

2.7. **Distribution of δ_ϕ** 35

2.8. **Conserved residues within $\mathrm{GABA_AR}$ subunits.** 36

2.9. **Water density along the pore.** 37

2.10. **Evolution of the interfacial band and pore oscillator in one replica of the WT system at 300K.** 38

2.11. **Evolution of the interfacial band and pore oscillator in second replica of the WT system at 300K.** 39

2.12. **Evolution of the interfacial band and pore oscillator in one replica of the WT system at 315K.** 40

2.13. **Evolution of the interfacial band and pore oscillator in one replica of the K289M system at 300K.** 41

2.14. **Evolution of the interfacial band and pore oscillator in second replica of the K289M system at 300K.** 42
2.15. **Evolution of the interfacial band and pore oscillator in one replica of the K289M system at 315K.** 43
2.16. **Evolution of the interfacial band and pore oscillator in second replica of the K289M system at 315K.** 44
2.17. **Poisson-Boltzmann profile.** 45
2.18. **Steered Molecular Dynamics.** 46
2.19. **Potential of Mean force.** 47
2.20. **ABF sample and gradient plots.** 47
3.1. **Flowchart describing the sequential steps involved in performing.** 51
3.2. **View of the TM domain, looking down on the membrane from the extracellular region.** 59
3.3. **View of the TM domain, looking down on the membrane from the extracellular region.** 60
3.4. **Screenshot of Autodock tools screen depicting a dialogue box describing.** 61
3.5. **Low and high energy conformation of Propofol** 61
3.6. **Side view of the sevoflurane in the β-α interface of the GABA(A) receptor system.** 64
3.7. **Cross-sectional view of the Sevoflurane flooded GABA(A) receptor system with the TMD aligned along POPC lipid membrane(colored by name) and placed in a box of explicit water (molecules not shown, represented as a blue box).** 65

3.8. **View from the extracellular domain, of a Sevoflurane flooded GABA(A) receptor system.** 66

3.9. **Propofol bound to an intersubunit site.** 67

3.10. **Flowchart for FEP.** 68

3.11. $\Delta\Delta G_i$ **variations.** 73

4.1. **View of the TMD of $\mathbf{GABA_A R}$ from the ECD** 80

4.2. **Flooding simulation of $\mathbf{GABA_A R}$ with sevoflurane.** 81

4.3. bf Protein-anesthetic interactions in intersubunit sites. 82

4.4. **Free energy of binding for Propofol and sevoflurane.** 83

4.5. **Water, lipid interactions at intersubunit sites.** 83

4.6. **Trajectory of propofol at subunit interface.** 89

Chapter 1

Introduction

One of the common signaling mechanisms across cell-membranes is the flow of ions in and out of the cell. This transmission of signals, i.e., flow of ions is mediated by the action of ion channels. These ion channels are called Ligand-gated receptors, when flow of ions across the cell membrane occurs upon ligand binding and opening the channel. The ligands that activate the receptors in the neurons are neurotransmitters, released from storage vesicles in the presynaptic membrane. This ion flux over the postsynaptic membrane subsequently triggers excitatory or inhibitory postsynaptic potentials. The nAChR and the 5-HT3, receptors are selective for cations (and hence excitatory), whereas GABA receptors and glycine receptors are selective for anions (and are thus inhibitory). These receptors have a similar transmembrane topology and contain three domains: extracellular, transmembrane, and intracellular. The structural features that define these receptors are a ligand-binding domain, generally in the extracellular region, formed by the ≈200 amino acid N-terminal domain that contains the disulfide-linked Cys-loop. The four helical transmembrane segments (M1, M2, M3, M4) form the ion channel. They are connected by two short loops, one is intracellular between M1 and M2, and the other extracellular between M2 and M3 and a long cytosolic loop between M3 and M4 (Figure **??**). The intra-cellular domain is formed by the long M3-M4 loop.

Identifying the structure of Acetylcholine Binding protein(**?**) and the electron density map of a cationic-selective receptor, nAChR(**??**), gave a wealth of information regarding the different domains of the receptor and the ligand protein interactions. Initially pLGICs were thought to be expressed only in the eukaryotic organisms. Subsequently, a genome search identified various bacterial homologues of the cys-loop receptor family (**?**) and among them, the study of the expression and function of a homologous protein from cyanobacterium *Gloeobacter violaceus*, gave insights into the prokaryotic origin of the family (**?**). Following this, X-ray structure of the prokaryotic channels, GLIC(**??**) and ELIC(**?**) were identified, thus providing models for investigations on ion permeation, ligand binding and gating in the channel. Both orthologous channels are cation selective, while GLIC channels are pH gated, ELIC is known to be activated by GABA.

The first structure of an eukaryotic, anion-selective Cys-loop receptor, the *Caenorhabditis elegans* glutamate-gated chloride channel a homopentamer (GluCl) (**?**), was reported to be in a potentially 'open' state, providing insights into potential mechanisms of interaction with orthosteric ligands and allosteric modulators. Subsequently, an apo and lipid-bound GluCl were crystalized(**?**) and on comparison with the potentially open state GluCl, revealed the possible tilting motion in the M2 helices of the TMD leading to the transition between apo and open states. The recently identified crystal structure of GABA(A) receptor in $\beta 3$ homopentamer form, had a unique M2 helix conformation, describing it to be in desensitized state. Despite identifying various eukaryotic and prokaryotic homologous crystal structures,in either a closed/resting, open/activated or closed/desensitized states, it has been challenging to understand the complex mechanism by which the ligand binding in ECD is coupled to the channel opening in TMD. One of the main challenges is the inability to explain the subtle interaction/dynamics of the channels , experimentally.

Molecular dynamics simulation gives us an opportunity to visualize these channel dynamics in a native-like membrane environment. While it might be unfeasible to observe complete transition between open to closed states using unbiased simulations, various biased simulations techniques have been used to identify barriers

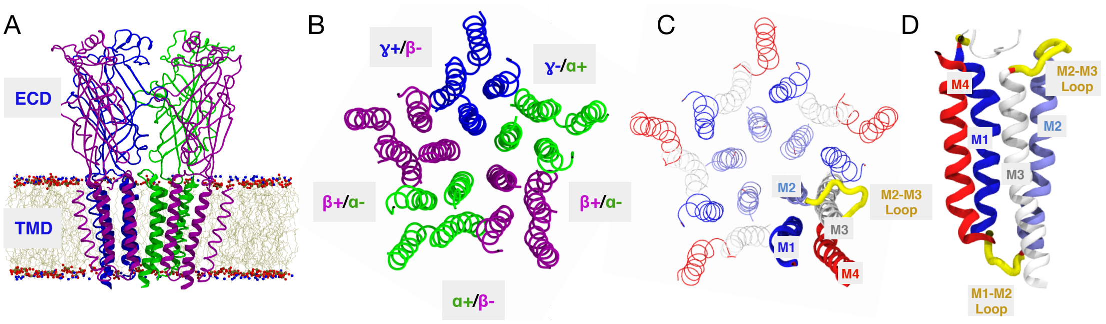

Figure 1.1: **Structure of pentameric Ligand-gated Ion Channel.** (A) Receptor is colored by subunit; aligned along the lipid membrane is the Transmembrane domain; the domain above the lipid membrane is the Extracellular domain. View of the TMD from the ECD; (B)receptor colored by subunits; (C) Receptor colored by occupancy, showing the individual helices comprising each subunit. (D) Cross-section view of the one of the subunits of the channel showing the four helices within a subunit.

in ion permeation, understand pore opening and closing and finding minimum free energy pathway between open and closed states (**?????**). These computational approaches in addition to the experimental information would help us explain the complex structure-to-function relationship. As a part of my PhD study, I performed simulations of the major inhibitory channel, $\alpha1\beta1\gamma2$ GABA(A) receptors and compared its dynamics with the mutant receptor, $\alpha1\beta1\gamma2$K289M GABA(A), that is known to cause febrile seizures.We show that at higher temperature (315 K), that channel spontaneously opens, explained by a classic Monod-Wyman-Changeux model of allostery. We further show how the cross-pore repulsions among the conserved basic residues on M2-M3 loop of all subunits and the interaction between these residues and charged residues on M2-helix of the TMD domain, can be crucial for stabilizing open conformation at higher temperature. Similar traditional MD approach was utilized to analyze the interactions between

M4 and M1/M3 helices in the TMD of GLIC receptor. With experimental results showing that the aromatic residues at the M4-M1/M3 interface is crucial for channel function, we simulated and compared the dynamics of Wild-type GLIC and 5-Ala-GLIC. 5-Ala-GLIC system involved GLIC receptor with 5 aromatic residues mutated to ALA residues at the M4-M1-M3 interface. As described in Appendix 1, these simulations revealed how the lipid penetration at this interface in 5-Ala-GLIC weaken the interactions between M4 and M1/M3 helices, thus disrupting the M4-Cys-loop interactions.

Similar challenges also occur in identifying the binding sites of the modulators of the ion channels. These ionotropic receptors, are also known to be modulated and in certain cases, directly activated by by certain exogenous and endogenous modulators. Among the various exogenous modulators are the general anesthetics. The mechanism of action of anesthesia is debated over a century since first usage in a surgery(**?**). Initial hypothesis of their mechanism , the 'Lipid-theory', identifies anesthetics as lipophilic molecules, and suggested its binding site to be the cell-membrane consisting of phospholipid bi-layer. While this theory failed to explain the molecular mechanisms that causes anesthesia, the subsequently postulated "protein-theory", suggested the different ion-channels and membrane proteins as a potential targets (**????**). Decades of research that followed have identified pentameric ligand-gated ion channels as being one of the main targets (**??**). Experimental techniques like mutagenesis(**?**), electrophysiology(**?**) and photolabelling(**?**)have consistently identified binding in the TMD of the protein. Furthermore crystal structures of GluCl(**?**) reveal ivermectin, bound to the upper TMD of the receptor, thus revealing possible binding sites in the inter-subunit regions of the upper-TM domain.Several experimental studies have identified putative binding site residues for Propofol in the β_α - α_γ, β_γ - α_β, α_β - β_α, interfaces (**?????????**) in GABA$_\mathrm{A}$R. For sevoflurane and volatile anesthetics in general, residues in α subunit has been shown to affect anesthetic modulation of the receptor (**??**). Despite the information regarding the binding sites residue, it has been difficult to define specific location of a site and clinical concentration at which a site is occupied. These experimental results are inconclusive due to the presence of multiple binding sites for an anesthetic in a receptor and different sites are occupied at different concentrations of the anesthetic. Specific computational technique, free energy perturbation molecular dynamics (FEP/MD) simulations can be used to compare the binding affinity of anesthetic for each site (**???**). Unlike docking, FEP/MD takes into account the protein's native membrane, influence of solvent , ligand and protein flexibility. This feature of the computational approach makes it more accurate, expensive and time consuming than docking. In addition, full convergence of the simulation is necessary for accurate results.

As described in Appendix 2, we used a similar approach to validate the experimental study, utilizing a novel chemically active alkylphenol anesthetic for quantitative affinity-based protein profiling (ABPP) of propofol. In accordance with the study, we were able to show that α_β - β_α and β_α - α_γ sites have higher affinity due to more amphiphilic nature of the site compared to the γ containing subunit interfaces. In addition, the last phase of my work involved calculating the isolated affinities of sevoflurane in GABA$_\mathrm{A}$R, rank the sites based on the affinity and also compare these values of propofol and sevoflurane.

.

Chapter 2

Physical Accuracy Leads to Biological Relevance: Best Practices For Simulating Ligand-Gated Ion Channels Interacting With General Anesthetics.

2.1 Abstract

GABAA receptors are critical for proper transmission of inhibitory signals in the central nervous system, and are common targets of anesthetic and anxiolytic drugs. They are also members of the widely-studied pentameric ligand-gated ion channel family (pLGIC). Here we use a slightly increased temperature to, for the first time, observe a stable spontaneous opening event of a pLGIC in molecular simulation. We find the opening event reflects interactions in two rings of homologous charges in the receptor transmembrane domain, an "interfacial band" containing five basic residues at M2 24' in the M2-M3 loop, and the "pore oscillator" composed of two acidic residues and one basic residue at 20' on the two β and one γ M2 helices respectively. The pore oscillator is shown to drive fluctuations in pore radius, by switching between attractive and repulsive cross-pore electrostatic interactions, consistent with a classic Coulomb charge-dipole arrangement. A conformational change of the interfacial band from an asymmetric to a symmetric state locks the pore oscillator in a repulsive (open) configuration. The γ_2 K289M mutation is a rare mutation (rs121909672) that causes seizures with fever and also neutralizes the γ_2 residue in the interfacial band. The electrostatic energy of an interfacial band with only four charges is shown to be more

sensitive to random shape fluctuations, which increase with higher temperature. Our simulation results indicate these effects are also transmitted to the pore. Temperature-enhanced fluctuations could thus cause rapid gating in these mutant receptors, consistent with flickering observed previously in single-channel recordings.

2.2 Introduction

Gamma-aminobutyric acid ($\mathrm{GABA_AR}$) receptors are inhibitory ionotropic receptors, critical to proper function of the mammalian central nervous system (CNS) and targets of numerous drugs aiming to depress CNS activity, such as benzodiazepines(**?**), and inhalational and intravenous general anesthetics.(**???**) They are members of the well-studied family of pentameric ligand-gated channels (pLGICs), which includes several other receptors common to CNS membranes, such as the nicotinic acetylcholine receptor (nAChR), 5HT-3 receptor, and glycine receptor. The larger family is found in a range of organisms, including prokaryotes, and exhibits high sequence and function diversity. Surprisingly, high resolution x-ray structures have revealed a common structure that is extremely well-conserved across the family, (**??????????**) which has made it particularly challenging to identify a universal group of interactions that drive gating.

Molecular simulation is a powerful technique for identifying subtle differences in interactions. It has been unfeasible to directly observe transitions to stable open states even in long molecular simulations of pLGICs, and pLGIC open state structures reliably close upon unbiased simulation, even under conditions in which they're expected to be stable. (**????**) Identifying opening pathways, therefore, requires an artificial bias or selection process to drive the receptor toward an open conformation. The pH-sensitive prokaryotic pentameric GLIC channel has been crystallized at high resolution in multiple conformations, and at pH corresponding to both resting and active states,(**???**); probable pathways between conformations have been determined using increasingly sophisticated molecular dynamics algorithms.(**????**) Such studies have identified collective motions common to the gating pathway, with Lev et al(**?**) recently identifying a sequence of collective events common to pathways generated using an enhanced sampling technique known as the string method.

The underlying origins of this instability have not been identified despite extensive efforts, in part because identifying the essential interactions missing from the simulation requires answering *a priori* the primary question the simulations hope to address : which interactions drive pore opening and closing. Simulations of gating in neurotransmitter-gated pLGICs are further hampered by low orthosteric ligand binding affinity due to a loss of cation-π interactions in non-polarizable forcefields.

Here we circumvent both these obstacles by exploiting the allosteric properties of pLGICs. In a classic Monod-Wyman-Changeux(**??**) model of allostery, unliganded receptors still fluctuate between active and resting conformations, with the probability of the active conformation usually expected to increase with small temperature increases. We observe conformational shifts consistent with the events at the domain interface reported by Lev et al(**?**), but are able to further identify the sequence of events preceeding the spontaneous pore opening, as well as the collective electrostatic interactions that drive them.

Each pLGIC subunit consists of an extracellular agonist-binding domain (ECD) and a transmembrane domain (TMD) containing a four helix bundle with helices labeled (M1-M4). The M2 helices line the pore, and the M2-M3 loop connecting the M2 and M3 helices interacts directly with both the TMD and the ECD.

The loop has long been hypothesized to transmit agonist binding to the transmembrane domain,(**??????**) with several mutation studies indicating the importance for agonist sensitivity of attractive electrostatic interactions among contact residues, such as salt-bridges, between the M2-M3 loop and the ECD. (**????**) The mechanism through which a change in these salt bridges (either forming or breaking) opens the pore is still unclear.

Our results suggest a non-specific mechanism for the final steps of gating that relies on multibody interactions within two sets of homologous charged residues: 1) a group of three residues containing both positive and negative charges, facing into the pore and forming a rapidly oscillating charge-dipole arrangement, which we term the pore oscillator, and 2) an interfacial band of five like charge residues at the interface of the ECD and TMD which, upon an energetically unfavorable conformational change, selects for an open conformation of the pore oscillator(Figure **??**).

We show using simple electrostatic expressions that repeated cross-pore repulsions in the interfacial band introduce a significant energetic penalty for shrinking the interfacial band, and that the symmetry inherent in the interfacial band amplifies the interactions between distant residues. Molecular dynamics simulations indicate this repulsion among interfacial band residues can be propagated along M2 helices to open the hydrophobic gate.

In $\mathrm{GABA_A R}$ receptors, the interfacial band is formed by a basic residue in the M2-M3 loop conserved across $\mathrm{GABA_A R}$ subunits as $\alpha K279, \beta K274$, or $\gamma K289$ (Figure **??**), and notated as M2 $24'$ in the prime numbering scheme suggested in (**?**). Sequence conservation of these charges across $\mathrm{GABA_A R}$ subspecies is shown in Figure S3. M2 $24'$ has been previously shown to be critical for conferring sensitivity to agonist; Harrison and colleagues(**?**) demonstrated via shift in EC50 that charge-reversal of $\alpha 279$ reduced sensitivity, which was restorable via additional charge-reversal of αD57 or αD149, both within the ECD and in the vicinity of

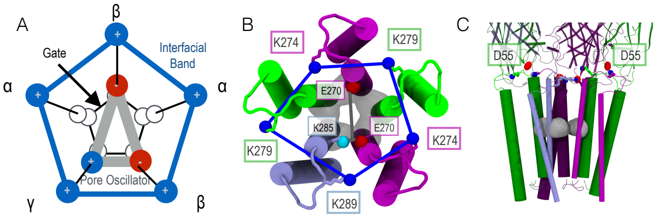

Figure 2.1: (A)Schematic of the $\mathrm{GABA_A}$R pore with relevant multibody interactions. A conserved basic residue at $24'$in the M2-M3 loop forms a pentamer of positive charges, interfacial band, drawn here in blue. The γ K289M mutation neutralizes one of the charges. One turn closer to the intracellular domain, one basic residue and two acidic residues constitute a charge-dipole arrangement, pore oscillator, is shown in gray. The tightest constriction is at the hydrophobic gate at $9'$, lined by five leucines (white). (B) View of the TMD from ECD, colored by subunit; γ - iceblue; β - purple; α - green. Charged ends of the residues forming the interfacial band and pore oscillator are represented by spheres connected (for visualization only) by gray and blue bonds respectively. Space-filling representation in gray depicts the hydrophobic gate at $9'$. (C) Side view of ECD and TMD showing the residues in (B), as well as the position of α D55 in the ECD.

the M2-M3 loop. Similar behavior was observed in the nicotinic acetylcholine receptor (nAChR), upon charge-reversal of α R209 in M1 and α E45 in the ECD.(**?**)

The basic residue at M2 24′ is also conserved in GLIC, ELIC, and GlyR, and was further implicated in interdomain communication in simulations of GLIC by Lev et al(**?**), who also found that salt bridging of M2 24′ with the ECD (D32) is correlated on a "high-probability communication pathway" with shrinking distances between M2 helices and pore closure. A causative and predictive physical mechanism, however, was not established.

Negative effects of a natural but uncommonly occurring missense single nucleotide polymorphism (SNP) at M2 24′ in the γ_2 subunit supports a role for collective charge interactions in stabilizing the open state. The γ_2:K289M mutation has been reported in families with generalized epilepsy and febrile seizures plus(GEFS+)(**???**), a generalized phenotype that often includes only febrile (fever-caused) seizures until about age 11, but can also include less severe myoclonic, atonic, or absence seizures at normal body temperature. In $\alpha_1\beta_2\gamma_2$ K289M receptors, GABA-evoked current amplitude was dramatically reduced relative to the WT (**??**), while in $\alpha_1\beta_3\gamma_2$K289M receptors the mutation did not affect current amplitudes but did increase the deactivation rate(**?**). In the latter receptors, currents had reduced mean open times, in part due to flickering(**???**). In hippocampal neurons containing GABA$_\mathrm{A}$R with γ_2:K289M subunits, accelerated desensitization of inhibitory post synaptic currents was also observed(**?**). Although a mechanism involving reduced trafficking has been proposed,(**?**) this would not explain the flickering observed in single-channel recordings.(**?**)

We have run unbiased MD simulations and adaptive biasing force (ABF) calculations of the $\gamma K289M$ mutant at multiple temperatures, and detect occluded channels at higher temperatures consistent with the known behavior of the K289M mutants, with differential dynamics of the interfacial band consistent with expectations based on the multibody expression. We propose a mechanism underlying the mutation's effects, involving destabilization of the open state due to the reduced cost to shrink a interfacial band with significant shape fluctuations .

2.3 Material and Methods

2.3.1 Simulations

This manuscript considers data from four systems: two replicas of the wildtype $\alpha 1\beta 1\gamma 2$ receptor (termed K1, K2) and 2 replicas of the K289M mutant (M1, M2). Each system was run for 500 ns at both 300K and 315K, for a total of 4 μs of unbiased MD simulation. Additional free energy calculations involved the K1 and M1 systems.The model used in this paper corresponds to Model 1 - CHOL from Reference(**?**), and was built with GluCl (PDB code : 3RHW) as a template as well as the alignments published in Ref(**?**). Further justification and details on this model can be found in Reference(**?**). The systems were prepared as in Ref(**?**), by embedding the protein in a homogenous lipid bilayer composed of phosphatidylcholine (POPC) built using CHARMM Membrane builder, with the final system containing 266 POPC molecules. All simulations used the CHARM22-CMAP(**?**) force field with torsional corrections for proteins. The CHARMM36 model(**??**) was used for phospholipids, ions, water and cholesterol molecules. Energy minimization and MD simulations were conducted using the NAMD2.9 package(**?**). A cutoff of 1.2 nm was used for non-bonded potentials, with a switching function starting at 1.0 nm; all simulations employed periodic boundary conditions, and long-ranged electrostatics were handled with smooth Particle Mesh Ewald method with a grid spacing of approximately 1Å. All simulations were run in the NPT ensemble with weak coupling to Langevin thermostat at temperature 300 or 315K, and a Langevin barostat at 1 atm. High temperature (315K) simulations were run for 500 ns following 200 ns of simulation at the lower temperature (300K). Full details are provided in SI.

2.3.2 Analytical Prediction of Multibody Interactions

Our simulation analysis is motivated by the multibody interactions within two arrangements of charges found around the GABA(A)r pore, representing the interfacial band and the pore oscillator. Each arrangement includes residues on opposite sides of the pore, and the plane containing the residues is normal to the pore axis, so attractive and repulsive interactions within the arrangement will contribute directly to pore-closing and pore-opening, respectively.

Charged pentamer

As shown in SI Theory, the total Coulomb energy for a charged pentagon with average side length $\bar{r}$ and average diagonal length $\bar{s}$ is

$$U_{+5}(\bar{r}, \delta_\phi) = \frac{5k_e e^2 \phi}{\bar{r}} \left(1 + \frac{\delta_\phi}{\phi}\right) + O(\bar{\delta r}^2) + O(\bar{\delta s}^2) \tag{2.1}$$

where e is the electron charge, $k_e = 332\text{Å}/\text{kcal/mol}/e^2$ is the Coulomb constant, and $\bar{\delta r}^2$ and $\bar{\delta s}^2$ are the variance in r and s across the five sides of the pentamer. For a regular pentamer $\bar{s} = \phi\bar{r}$ where $\phi \equiv \left(1 + \sqrt{5}\right)/2 \sim 1.62$ is a geometric constant often called the "golden ratio", with the convenient property $1/\phi = \phi - 1 = 0.62$. δ_ϕ is the deviation of $\frac{\bar{r}}{\bar{s}}$ from the value for a regular pentamer : $\delta_\phi \equiv \frac{\bar{r}}{\bar{s}} - (\phi - 1)$.

The linear term in δ_ϕ reflects the effects of shape fluctuations on the relative contributions of diagonal and adjacent pairs. Second-order terms given by $\bar{\delta r}^2$ and $\bar{\delta s}^2$ reflect variance in the adjacent and diagonal distances respectively. According to Eq. **??**, positive values of δ_ϕ (in which diagonal distances are shorter

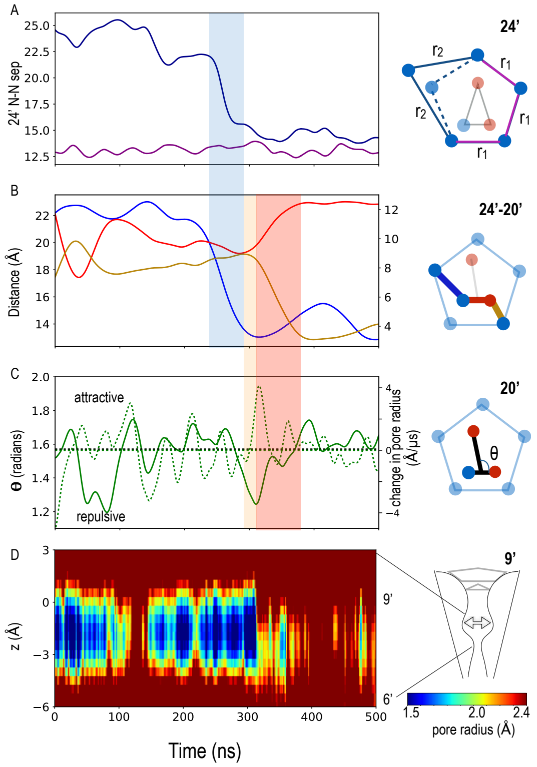

Figure 2.2: **Evolution of the interfacial band and pore oscillator in one replica of the WT system at 315K.** (A) Flip of one residue (α-K279) so the interfacial band switches from elongated to regular pentamer, occurs at ∼250 ns, followed by a series of events leading to the pore opening between ∼250 ns - 350ns, as marked by the shaded regions. (B) The distances between residues $\alpha K279 - \gamma K285$, plotted on y-axis and $\gamma K285 - \beta$-K270, β-K270 − β-K274, plotted on alternate y-axis, are shown in blue, red and gold respectively. (C) The solid green curve depicts the angle between the charge-dipole arrangement representing the pore oscillator ; The Dotted green line represents the pore-opening event as measured by calculating the first derivative of the minimum pore radius. (D) Pore radius as a function of distance along the pore axis and time. All curves are smoothed as described in SI Methods. Transition windows are shaded blue (early), orange (mid), and red (late).

than expected in a regular pentamer) will increase the overall energy of the interfacial band, provided the average distance between adjacent residues ($\bar{r}$) is kept constant. This asymmetry-induced increase in energy can be offset by an overall increase in the size of the interfacial band : δ_ϕ ¿0 will stabilize a larger $\bar{r}$. Similarly, negative δ_ϕ will decrease the overall energy of the interfacial band and allow it to close with reduced penalty.

Neutralizing any of the charges removes two diagonal and two adjacent interactions, so the Coulomb energy for 4 like-charges arranged on a pentagonal lattice is

$$\begin{aligned} U_{+4}(\bar{r}, \delta_\phi) &= \frac{3k_e e^2 \phi}{\bar{r}} \left(1 + \frac{\delta_\phi}{\phi}\right) + O(\bar{\delta r}^2) + O(\bar{\delta s}^2) && (2.2) \\ &= \frac{3}{5} U_{+5}(\bar{r}, \delta_\phi) && (2.3) \end{aligned}$$

where averages only consider distances involving charged residues, and therefore $\bar{r}$ and δ_ϕ incorporate only three adjacent distances and three diagonal distances. The factor of 3/5 will generally stabilize a smaller value of $\bar{r}$ at any temperature, but $\delta_\phi, \bar{\delta r}^2, \bar{\delta s}^2$ will also be directly dependent on temperature. The simple Coulomb calculation represented in Eq. **??** indicates a large energetic cost of shrinking the interfacial bandover typical distances (Fig S1B). Considering typical distances between homologous residues in pLGICs, the strength of the interaction among homologous residues may be unintuitive. Reducing the distance between two like charges from $r_1 = 15\mathring{A}$ to $r_1 = 12\mathring{A}$ raises the electrostatic energy by only 5.5 kcal/mol, but shrinking the regular pentagon (including diagonal interactions) from $r_1 = 15\mathring{A}$ to $r_1 = 12\mathring{A}$ increases the energy of the arrangement by 49 kcal/mol! Diagonal, cross-pore interactions contribute almost 20 kcal/mol, nearly doubling the total.

Charge-dipole

Farther away from the interface with the ECD, facing the pore, is another charged ring of three residues, at M2 20′ (βE270 and γK285), that we term the "pore oscillator " because it exhibits rapid shape fluctuations that are propagated to the hydrophobic gate. The Coulomb energy reflects two diagonal interactions, and one adjacent interaction, and is effectively a charge-dipole interaction:

$$U_{c-dp} = -\frac{k_e e^2}{r}\left(\frac{r}{d} + \frac{1}{z^+} - \frac{1}{z^-}\right) \tag{2.4}$$

$$z^{\pm} \equiv \sqrt{1 + \left(\frac{d}{2r}\right)^2 \pm \frac{d\cos\theta}{r}} \tag{2.5}$$

where U_{c-dp} is the Coulomb energy of the charge-dipole, d is the distance between the two charges forming the dipole, r is the separation between the charge and dipole midpoint, $z^{\pm}$ are the distances between the charge and the close and far ends of the dipole, respectively, and θ is the angle between the dipole and dipole midpoint-charge separation vector (see diagrams in Fig. **??**C and S1B).

It is common in undergraduate-level treatment of charge-dipole interactions to assume $r/d >> 1$ in Eq. **??**, but for a charge-dipole arranged on a regular pentagonal lattice, $r/d \equiv \phi \sim 1.6$. One central result from the usual treatment is that at $\theta = \pi/2$, the interaction switches from being attractive to repulsive, with a discontinuity at the boundary; this result still holds in the full expression (Fig S1B), as expected.

2.4 Results and Dicussion

2.4.1 Spontaneous opening event at 315 K

A spontaneous opening event was observed in one WT replica at the higher temperature. In this replica, the pore was closed for over 500 ns at 300K (Figure S6), but after raising the temperature to 315K and about 200 ns of simulation, a spontaneous set of events induced a stable open pore for the remainder of the simulation. (Figure **??**, and SI Movie S1). The event itself took about 100-150 ns, and involved the following stages, shaded by the specified colors in Figure **??**.

1. **Early (blue): Symmetrization of interfacial band.** The interfacial band begins in an elongated conformation, because the side-chain of one charged residue (α_γ-K279) faces away from the pore axis, while all other side-chains face toward it. Between 200 and 260 ns, this side-chain flips, causing the interfacial band to switch from an elongated to a regular conformation (Figure **??** A). This flip may be dependent upon flexibility introduced by the adjacent proline (αP278); the conservation(**?**) and significance of this proline for function(**?**) are well-established, although its fundamental role in gating has been unclear.

2. **Mid (orange): Response to symmetrization; partial opening and deformation.**

    (a) t = 260-300 ns: The previous symmetrization step is electrostatically unfavorable for the other residues of the interfacial band and for the basic residue of the pore oscillator; in response, the M2 helices of the flipped α subunit and the γ and β subunit on either side separate from the other two subunits. This initiates widening of the pore, as shown by the sharp transition in Figure **??** D. Simultaneously, the positively-charged end of the pore oscillator dipole (γ-K285) is deflected toward the intracellular domain and away from the ECD (Figure **??**). This destabilizes its salt-bridge with the negatively charged residue comprising the other end of the "dipole", β_γ-E270.

    (b) t=300-330 ns: Upon weakening of favorable electrostatic interactions with positively charged residues in the pore oscillator and interfacial band, the two negative sidechains of the pore oscillator pivot around

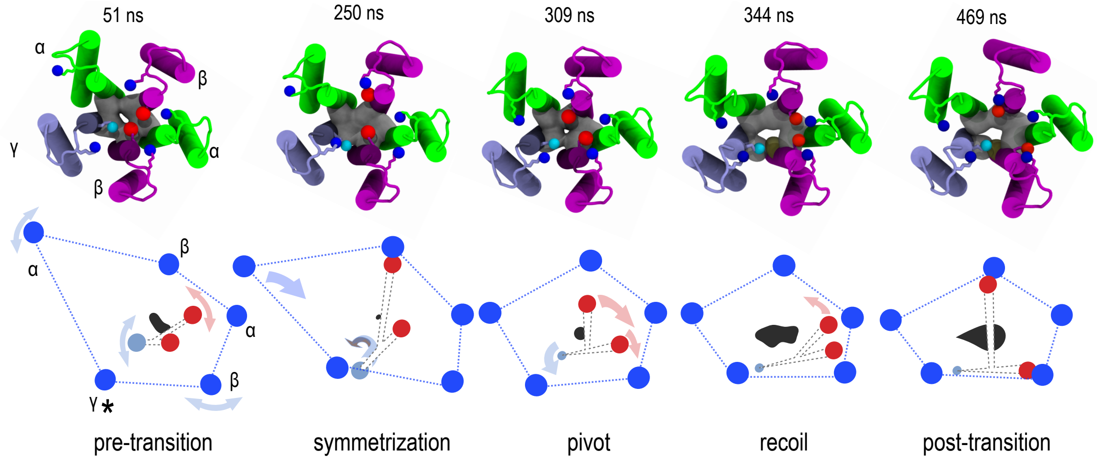

Figure 2.3: **Evolution of pore oscillator and interfacial band during spontaneous opening event.** Top: Representative frames are shown from the WT trajectory at 315K, with coloring as in Figure 1B/C. Bottom: Cartoon of transition highlighting movement of the charged groups forming interfacial band(blue) and pore oscillator (γK280-cyan, βE270-red). Dashed lines connecting the points of the pore oscillator and interfacial band are for visualization purposes only and do not represent physical bonds. The filled gray shape indicates the unoccluded area of the hydrophobic gate. After α K279 flips during the symmetrization step, M2 helices separate along the axis connecting the flipped and current positions (frame at 344 ns), while after the acidic residues pivot, M2 helices separate along the axis connecting the two acidic residues (post-transition panel). Salt-bridges are represented by contacting red and blue spheres. The asterisk marks the charge that is neutralized with the K289M mutation.

their C_α atom to face away from the γ subunit. This switches the pore oscillator charge-dipole interaction from attractive to repulsive, as tracked by θ in Figure **??** C and according to Eq. **??**; for small values of θ, the distance between the two negatively charged residues becomes particularly small (Figure **??**).

3. **Late (red): Recoil and Stabilization.**

The pore-oscillator is now in a highly unfavorable configuration due to proximity of the two negative charges corresponding to low values of θ. The resulting repulsion causes a rapid separation of the charges. This is further propagated to increase the distance between their respective M2 helices, as indicated by an additional increase in pore radius, not just at the pore oscillator but also at the minimum constriction 16-17 Angstroms away (Figure **??** D). The trajectories of θ and the time derivative of the minimum pore constriction are shown plotted on the same axis in Figure **??** C; the two most rapid increases in the pore radius each occur directly after the two θ compression events (at t = 100 ns and t = 325 ns). This association was also qualitatively observed in the other replica trajectories (Figures S5-S11), although in some cases it was a less acute value of θ, held over a longer time period, that preceded opening.

Upon recoil, each of these two acidic residues formed an intrasubunit salt-bridge with a basic residue of the interfacial band (Figure **??** B). Since the charged interfacial band is resistant to shrinking, these salt-bridges can only form if the acidic residues in the pore oscillator are also separated. The timing of events is consistent with pore oscillator recoil simultaneously allowing salt-bridging with the interfacial band and causing an overall separation of M2 helices. Due to the stochastic nature of the trajectory, determining the typical order of these two events would require many more replicas.

The pore oscillator samples small values of θ regardless of the configuration of the interfacial band, due to high frequency oscillations consistent with the discontinuity in the interaction, including twice in this particular trajectory (once at $t = 100$ ns and once at $t = 350$ ns). Such events were observed in all simulated systems and were usually followed by brief opening of the pore. A stable opening event, however, was only observed when salt-bridging of each of the pairs of β-E270 and β-K274 residues was also stable, which depended upon the symmetrization step. The significance of the symmetric interfacial band is verified through the next set of simulations involving a mutant of an interfacial band residue.

γ K289M increases energetic sensitivity to shape fluctuations of the interfacial band

The multibody mechanism proposed in the previous section suggests an important role for each basic residue in the interfacial band for conferring stability of the open state, beyond communication with the agonist-binding domain. γ subunits are not required for functional GABA(A) receptors, and do not participate in the interfaces forming the orthosteric binding sites. Yet neutralizing the γ-contributed charge to the interfacial band causes flickering in single-channel recordings (**?**) and is associated with fever-induced seizures.

Simulations of the two K289M replicas at both 300K and 315K, as for the WT receptors, indicated a reverse temperature dependence for the distribution of minimum pore radii (Figure **??**). As shown in Figure **??** A, we observe no effect of the mutation on the overall distribution of pore radii at 300K. At 315K, the WT distribution broadens, as expected (Figure **??** B). The K289M distribution broadens even more at the higher temperature, but is also shifted toward smaller radii, so that at 315K both WT replicas have larger pore radii than both K289M replicas for most frames.

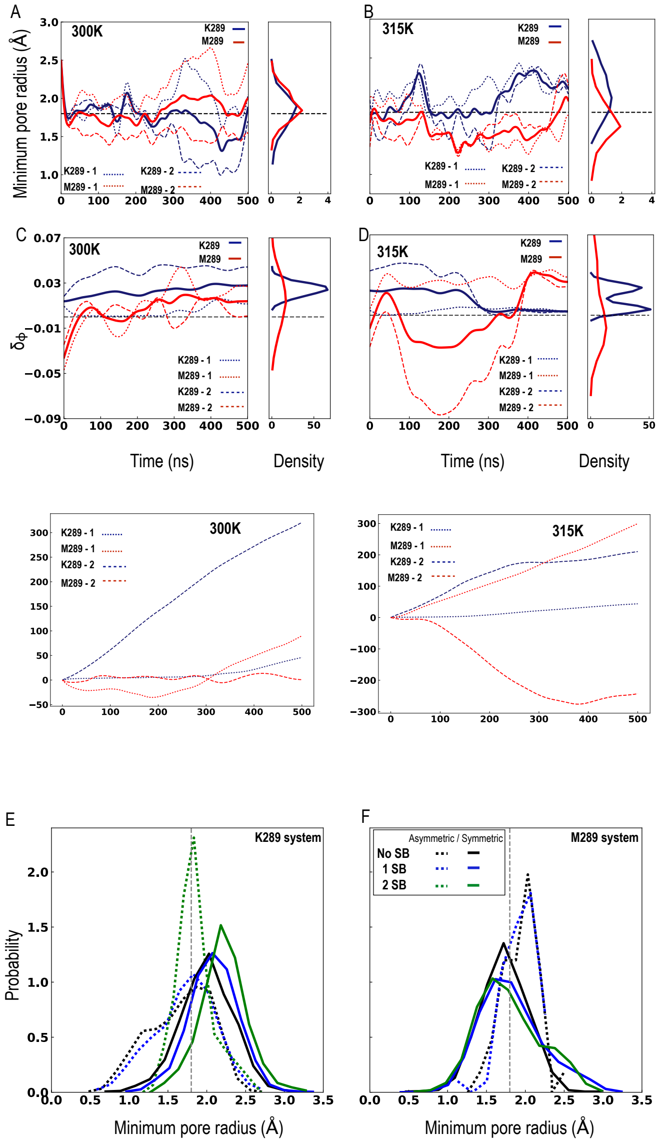

Figure 2.4: **Correlations between shape of interfacial band, pore radius, and salt-bridging between interfacial band and pore oscillator for multiple replicas and temperatures.** (A/B) Smoothed time evolution of the pore minimum constriction, averaged (solid lines) over two replicas (shown separately as dotted lines) each, at 300 K and 315 K. The radius of a chloride ion is represented by the dashed horizontal line at 1.8Å. (C/D) Smoothed time evolution and distribution of δ_ϕ for both WT and K289M systems at 300 and 315K. Distribution trends are similar to those generated numerically, discussed in SI Theory. (E/F) Distribution of minimum constriction radius for conformations clustered by total number of β K274-E270 salt-bridges and symmetrization of the interfacial band.

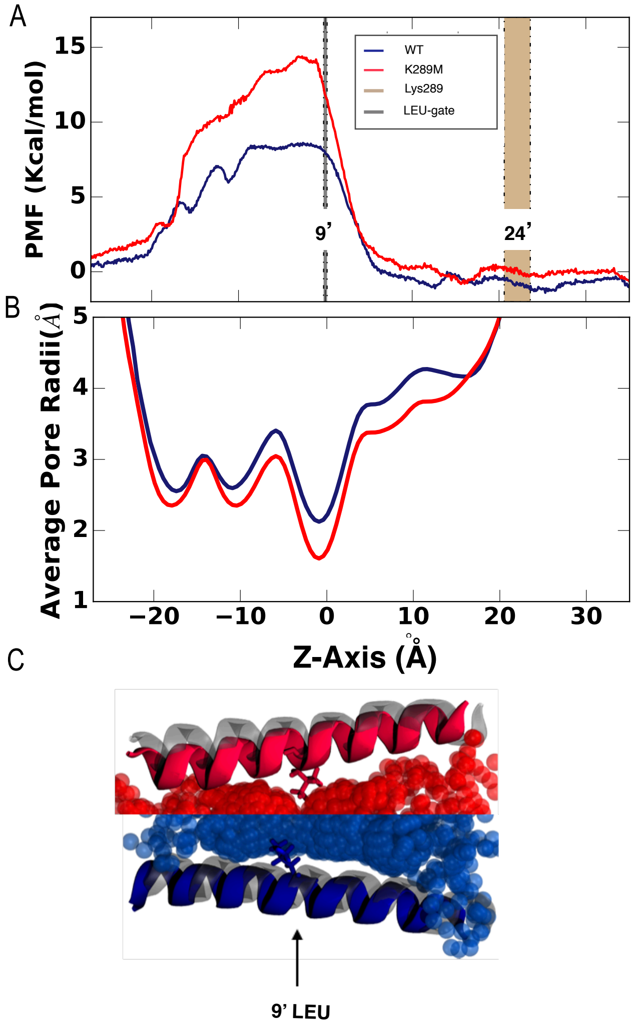

Figure 2.5: **Potential of mean force** (A) Potential of mean force profile of a chloride ion crossing the ion channel, calculated at 315K for a receptor that remained primarily in the elongated conformation for the WT and had a flexible interfacial band for the K289M. The full PMF including the rest of the simulation box is in Fig S14. (B) Average pore radius profile for the conformations in (C).

Eq. **??** indicates three possible contributions to a reduced cost for shrinking the K289M interfacial band compared to that of the WT interfacial band:

1. The reduced charge of the K289M interfacial band results in a factor of 3/5 for the overall energetic cost to shrink the K289M interfacial band, assuming the same value of $\bar{r}$ and δ_ϕ. This contribution is not temperature dependent, and the 40% loss is large enough that it is perhaps most surprising that an K289M receptor is functional at any temperature. This may be explained by the observation that in the K289M systems, $\gamma M220'$ (M2 K285) of the pore oscillator assumes a position much closer to the original position of K289.

2. Any reduction in δ_ϕ will destabilize the open state by reducing the energetic cost to shrink the interfacial band(Eq. **??**). Both increased temperature and the loss of charge symmetry would be expected to increase the root-mean-square-displacement (RMSD) of each remaining side-chain. We ran simple numerical calculations to determine how increased RMSD in individual charges affects the distribution of δ_ϕ, shown in Figure S2. The distribution of δ_ϕ is not particularly sensitive to RMSD if all five charges of a closed pentagon are used, due to geometric constraints and the non-cohesive nature of the noise. The distribution is expected to widen with increased RMSD, but mainly in the positive direction (Figure S2A).

3. Even if each individual (conserved) charge has the same RMSD in the K289M and WT receptors, the distribution of δ_ϕ will be broadened in the K289M receptor because only three of the five adjacent and diagonal distances are used to calculate the average adjacent and diagonal distances, and they are not constrained by the requirement of forming a closed pentagon (Figure S2). Furthermore, the broadening is symmetric, with significant

> probability of $\delta_\phi < 0$. This is consistent with what we observe in the molecular systems, as shown by deviations of the ratio of diagonal to adjacent distances from $1/\phi$ (Figure **??** C,D) over each trajectory.

Comparison between Figure **??**A,B and C,D, reveals similar trends for distributions of minimum pore radius and δ_ϕ, upon introducing the mutation, raising the temperature, or both.

The pore oscillator-interfacial band salt-bridge formation becomes uncorrelated from the pore radius in the K289M systems, as shown in Figure **??** F.

2.4.2 γ K289M increases barriers to conduction via channel conformation rather than direct interactions with ions

Determining whether a single ion channel conformation corresponds to an "open" or "closed" state is frequently not possible in unbiased MD simulations, except for conformations at an extremum. A Cl- atom has a radius of approximately 1.8Å, the hydrophobic residues lining the minimum pore radius but makes it unlikely a Cl- atom will pass through a constriction of exactly 1.8Å ; when both salt bridges between the interfacial band and pore oscillator are formed, the WT receptor has a minimum pore radius of at least 2.5Å.

The effects of the mutation on purely electrostatic barriers for chloride ion translocation was quantified via the Poisson-Boltzmann equation as described in SI Methods. The mutation from a positively charged to neutral residue led to insignificant changes in the electrostatic potential along the most favorable path given identical starting conformations (as shown in Supplementary Figure S12), suggesting that the mutation alone could not affect conductance without inducing conformational shift. Although the electrostatic potential is weakened near the mutation, the ion can adjust its pathway through the channel to fall closer to the other four residues in the interfacial band. Calculation of the electrostatic potential using the equilibrated structures of WT and K289M receptors showed a 5-10 kcal/mol (Figure S12C) higher electrostatic barrier in K289M, predominantly occurring in the transmembrane domain enclosing the residues containing the minimum pore constriction region.

The PMF for chloride ion translocation at 315K, measured using ABF, is shown in Figure **??**. The largest barrier for the WT of 8 kcal/mol is proximal to the leucine residues at M2 $9'$, forming the tightest constriction; this barrier is increased by 5 kcal/mol for the mutant receptors. The difference in PMF near residue $\gamma_2$289 is much less than 1 kcal/mol. While mutation of a positively charged to neutral residue does have a small effect on affinity of the chloride ion for the region of the receptor near the mutation, the dominant effect of the mutation on conduction is via conformational instability of the open state.

2.5 Conclusion

The primary new insights of this work are:

1. Repulsive cross-pore electrostatic interactions at the TMD-ECD interface (the "interfacial band") stabilize the open state of the GABA(A) receptor; the interfacial band becomes more resistant to shrinking as the average separation between adjacent charges decreases or as the relative strength of diagonal interactions is reduced.

2. In $\mathrm{GABA_A}$R receptors with 2 α subunits, 2 β subunits, and 1 γ subunit, a three-body charge-dipole arrangement (the "pore oscillator") among three M2 helices (two adjacent and one diagonal) drives fluctuations in minimum pore radius, by alternating between a repulsive and an attractive configuration. All three charges are conserved within α, β and γ species of the GABA(A) receptor (although γ_3 has an arginine instead of a lysine, Figure

S3).

3. Switching from an asymmetric to symmetric configuration of the interfacial residues in (1) can lock the charge-dipole interaction in (2) in a repulsive configuration, via a pair of salt-bridges between the pore oscillator and interfacial band.

4. Neutralizing one of the residues from (1), as in the epilepsy-associated γ_2K289M mutations, makes the cost to shrink the interfacial band more sensitive to dispersion of the remaining charges; at higher temperatures this results in a significant population of closed states. This is consistent with the flickering observed in receptors with this mutation in *vitro*, as well as the critical role of fever in inducing seizures for this phenotype.

The debate over the mechanism through which binding of a ligand at one site regulates the effects of binding of a ligand at another site ("allostery") is over fifty years old,(**??**) and much of that debate was focused on placing mechanisms within two extreme cases : "conformational selection" (functional conformations are visited in the absence of ligand but stabilized by ligand, the Monod-Wyman-Changeux or MWC model) or "induced fit" (functional conformations require all ligands to be bound, also known as the Koshland-Nemethy-Filmer model).

The mechanism for pore opening observed here fits most consistently with an MWC model, but the presence of both the interfacial band (1) and the pore oscillator (2) suggests a sequence of conformational events, with each event in the sequence falling at a different location along the continuum between pure conformational selection and pure induced fit. Although effects of the substitutions of interfacial band residues have been studied numerous times, we are unaware of mutagenesis studies involving either of the residues of the pore oscillator ($\gamma K/R285$ and $\beta E270$). The present simulation results suggest a role for these residues in determining receptor kinetics, including desensitization.

Our results indicate that a topological view of pLGICs may be counterproductive for conceptualizing gating mechanisms, because interactions entirely within a helix/subunit (or between two adjacent helices/subunits) are only indirectly related to conformation of the pore. While we present these results in heteropentamers, and the presence of the pore oscillator requires multiple subunit species, the role of symmetry in stabilizing conformations with open or occluded pores has been demonstrated previously in both heteropentamers such as nAChR(**?**) and homopentamers such as GLIC. (**?**) Our results indicate a critical role for diagonal interactions in determining the effects of asymmetry; asymmetry that decreases or increases diagonal distances opens or closes the pore respectively.

More generally, the Coulomb interaction between two charges placed on the diagonal of a regular pentagon will only be moderately reduced from the interaction they would have as adjacent charges. Diagonal interactions will always contribute 38% of the overall interaction energy. A role for long range interactions within the nAChR TMD-ECD interface has been recently demonstrated by Auerbach and colleagues(**?**). The residues forming an interfacial band need not be located in the M2-M3 loop; they could also be in the M1 linker as in nAChR, or even in the M4 C-terminus. The concept of an interfacial band that we propose here is topologically abstract, but depends on pentameric symmetry and a regular charge density at the interface between the two domains; it may therefore be generalizable to many or even all pLGICs.

2.6 Supporting Methods

The systems were solvated using the SOLVATE plugin in VMD(**?**) and neutralizing ions were added to bring the system to a 0.15M salt concentration using the AUTOIONIZE plugin. The final system contained about 160,000 atoms. MUTATE plugin was used to introduce the K289M mutation in the γ subunit of

$GABA_A$R receptor.

All bonds to the hydrogen atoms were constrained using the SHAKE/RATTLE algorithm. A multiple time-step rRESPA method was used, and controlled with a high frequency time-step of 2fs and low frequency time-step of 4fs. All the systems were energy minimized for 10000 steps, then simulated for 5 ns with restraints of 1 kcal/mol/Å applied to the C_α atoms of the protein. Restraints were then removed and 495 ns of nearly unrestrained simulation was carried out in all four systems at low temperature. During this period of the simulation, only harmonic restraints (force constant 0.4 kcal/mol/Å) between the intracellular ends of the M3 and M4 helices were used, to mimic the effects of the intracellular domain and prevent separation of the M4 helix from the rest of the bundle.

2.6.1 Long-range electrostatics

The simulations here used the prescribed cutoff value of 12 $\mathring{A}$ for the CHARMM forcefield, with a switching function past 10$\mathring{A}$, combined with PME and a grid size of about 1Å. The distances between charged residues in the interfacial band are similar to this cutoff distance, and it is not uncommon to use cutoffs less than 10Å(as in (**?**)). This may cause a significant accumulated error in simulations of any proteins with repeated interactions near the cutoff/switching distance, not just pLGICs. In pLGICs, it can reduce the energetic cost of shrinking the interfacial band, leading to an increased likelihood of closed states even in WT systems. By recalculating energies using direct Coulomb electrostatics just for interfacial band and pore oscillator residues, from a trajectory generated using PME, we found PME reduced the energetic difference between elongated and regular conformations by about 5 kcal/mol.

2.6.2 SMD Simulations

Steered Molecular Dynamics (SMD) simulations (**??**) were used to obtain favorable positions of the ion at different positions along the channel, for later use in Adaptive Biasing Force (ABF) calculations. The chloride ion was pulled along the pore of the channel at a constant velocity of 10Å/ns. The force required to pull at constant velocity is also calculated, and can, in principle, be used to calculate a potential of mean force (PMF) using Jarzynski's equation (**??**), but in practice it is challenging to achieve a sufficiently slow pulling speed.

2.6.3 ABF Simulations

Adaptive biasing force calculations (ABF)(**????**) were used to measure the potential of mean force (PMF) of a chloride ion translocating the GABA$_A$R ion channel at 315K, for both the WT and K289M channels. ABF was performed using the Collective Variables module(**?**) of NAMD2.9. The pore axis was divided into 23 bins of each 5Å length.

Initial coordinates for the ion were obtained from SMD simulations (as described in SI). One thousand samples were collected in each bin prior to the application of ABF to avoid undesired non-equilibrium effects on the dynamics. Fifteen ns of trajectory were generated in most bins, while bins near the primary barrier in the pore contained 25 ns.

2.6.4 Pore Analysis

Measurement and analysis of the pore radii has been carried out using the HOLE software (**?**) and TCL scripting through VMD(**?**). Python scripts have been used to analyze and visualize the hydration of the pore throughout the simulation.

2.6.5 Poisson-Boltzmann Calculations

The Poisson-Boltzmann (PB) profile for conduction of both a Na+ and Cl- through the ion channel was calculated using APBSmem(**?**). The pre-generated PQR format of the proteins using PDB2PQR(**?**) tool was used as the input for the electrostatic potential calculations.

These calculations were performed for initial non-equilibrated structures of the protein, as well as for conformations extracted from the last 50 ns of both the 300K and 315K MD simulations (for Cl-).

2.6.6 Graphs and images

All plots were calculated and drawn using Python and Tcl scripts.In Figure 2 and the similar supplementary figures S5-S11, the series of curves depicting the pore-opening events were further smoothened using a digital filter(Butterworth) with a order of the filter value, 2, and a critical frequency value, 0.02, as implemented in the SciPy python module. The time derivative of the minimum pore radius was calculated using the gradient function implemented in the numpy python module. VMD(**?**) was used for visualization and for creating molecular images and movies.

2.7 Supporting Theory

We consider an irregular pentagon with five side lengths r_i and five diagonal lengths s_i (Figure S1A). The total Coulomb energy for the charged ring is given by

$$U_{+5} = k_e e^2 \sum_i^5 \frac{1}{r_i} + \sum_i^5 \frac{1}{s_i} \tag{2.6}$$

where e is the electron charge, $k_e = 332\text{Å/kcal/mol}/e^2$ is the Coulomb constant. Writing each distance as a perturbation from the average : $r_i = \bar{r}(1 + \delta r_i)$ and

$s_i = \bar{s}(1 + \delta s_i)$, where the average adjacent length $\bar{r} = \sum_i^5 r_i/5$ and the average diagonal length $\bar{s} = \sum_i^5 s_i/5$. Expanding in powers of δs_i and δr_i,

$$\sum_j^5 \frac{1}{r_j} = \sum_j^5 \frac{1}{\bar{r}(1+\delta r_i)} = \frac{1}{\bar{r}} \sum_j^5 (1 - \delta r_i + O(\delta r_j^2)) \tag{2.7}$$

$$= \frac{5}{\bar{r}} \left(1 + O(\bar{\delta r}^2)\right) \tag{2.8}$$

and similarly,

$$\sum_j^5 \frac{1}{s_j} = \frac{5}{\bar{s}} \left(1 + O(\bar{\delta s}^2)\right), \tag{2.9}$$

where we have used $\sum_j^5 \delta s_j = \sum_j^5 \delta r_j = 0$, and $\bar{\delta r}^2$ and $\bar{\delta s}^2$ are the variance in r and s across the five sides of the pentagon respectively. Therefore,

$$U_{+5} = k_e e^2 \left(\sum_i^5 \frac{1}{r_i}\right) \left(1 + \frac{\sum_j^5 \frac{1}{s_j}}{\sum_j^5 \frac{1}{r_j}}\right) \tag{2.10}$$

$$= k_e e^2 \left(\frac{5}{\bar{r}} \left(1 + O(\bar{\delta r}^2)\right)\right) \left(1 + \frac{\frac{5}{\bar{s}}(1 + O(\bar{\delta s}^2))}{\frac{5}{\bar{r}}(1 + O(\bar{\delta r}^2))}\right) \tag{2.11}$$

$$= \frac{5 k_e e^2}{\bar{r}} \left(1 + \frac{\bar{r}}{\bar{s}}\right) + O(\bar{\delta r}^2) + O(\bar{\delta s}^2) \tag{2.12}$$

For a symmetric pentagon $\bar{s} = \phi \bar{r}$ where $\phi \equiv \left(1 + \sqrt{5}\right)/2 \sim 1.62$ is a geometric constant usually called the "golden ratio", representing the ratio between the lengths of a pentagon diagonal and side, and with the convenient property $1/\phi = \phi - 1 = 0.62$. We define δ_ϕ as the deviation of $\frac{\bar{r}}{\bar{s}}$ from $1/\phi = \phi - 1 = 0.62$, so $\delta_\phi \equiv \frac{\bar{r}}{\bar{s}} - (\phi - 1)$, and

$$U_{+5} = \frac{5 k_e e^2 \phi}{\bar{r}} \left(1 + \frac{\delta_\phi}{\phi}\right) + O(\bar{\delta r}^2) + O(\bar{\delta s}^2) \tag{2.13}$$

The linear term in δ_ϕ reflects the effects of asymmetry on the relative contributions of diagonal and adjacent distances. Second-order terms given by $\bar{\delta r}^2$ and $\bar{\delta s}^2$ reflect variance in the adjacent and diagonal distances respectively. According to Eq. **??**, positive values of δ_ϕ (in which diagonal distances are shorter than expected in a regular pentagon) will increase the overall energy of the interfacial band, provided the average distance between adjacent residues ($\bar{r}$) is kept constant. This asymmetry-induced increase in energy can be offset by an overall increase in the size of the interfacial band : δ_ϕ ¿0 will stabilize a larger $\bar{r}$. Similarly, negative δ_ϕ will decrease the overall energy of the interfacial band and allow it to decrease the average separation $\bar{r}$ with reduced penalty.

Any reduction in δ_ϕ will thus destabilize the open state. We ran simple numerical calculations to determine how increased random noise would affect the distribution of δ_ϕ. Five points were generated with random polar angles corresponding to $\{0 + \zeta_1, 2\pi/5 + \zeta_2, 4\pi/5 + \zeta_3, 6\pi/5 + \zeta_4, 8\pi/5 + \zeta_5\}$ where ζ_i was a random value taken from a flat distribution in the range $\pm 3\pi/40$ (low variation) or in the range $\pm 5\pi/40$ (high variation), and the radial values were $\{1.5 + \rho_1, 1.5 + \rho_2, 1.5 + \rho_3, 1.5 + \rho_4, 1.5 + \rho_5\}$ where ρ_i was a random value from a flat distribution in the range ± 0.375 (low variation) or ± 0.625 (high variation). Although these are the specific values used in Figure **??** and are given for completeness, the overall trends were not particularly sensitive to the precise values chosen.

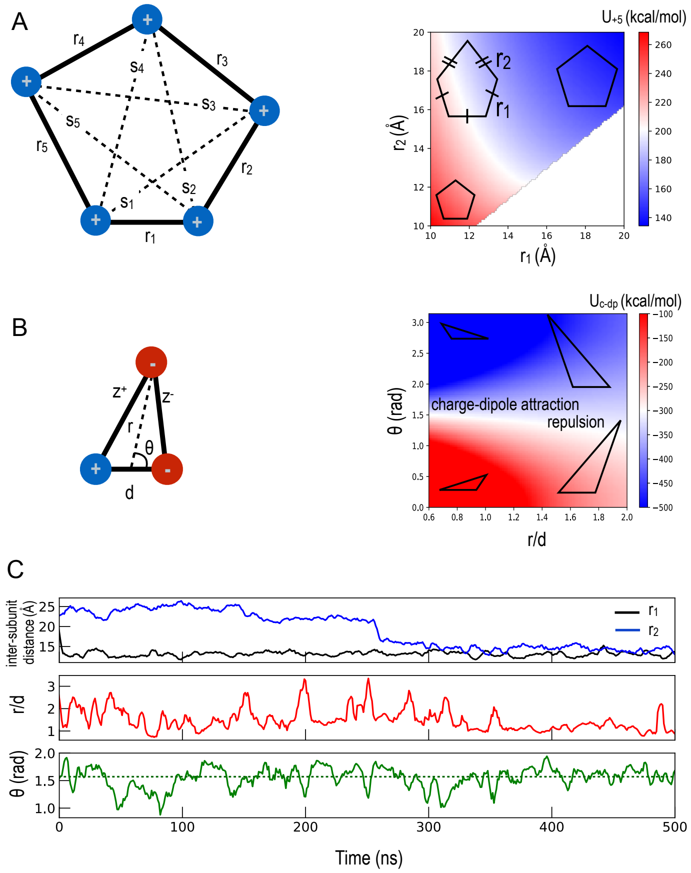

Figure 2.6: **Theory variables** (A) Adjacent and diagonal distances for the pentagonal Interfacial Band used to calculate averages for Eq. **??**, and the associated electrostatic energy for the special case of a pentagon in which three sides are identical and two adjacent sides are also identical, but may differ from the other three. This special case is similar to that observed for the symmetrization step in Figure 2. (B) Definition of terms for the charge-dipole interaction that is formed by three residues in the pore oscillator , as well as associated energy. At around $\theta = \pi/2$, the potential energy shifts from decreasing with increasing distance (repulsive) to increasing with increasing distance (attractive). C) Trajectory for defined angles and distances for the K315 replica explored in Figure 2; curves shown here are smoothed much less than in Figure 2 and retain significantly more high frequency noise.

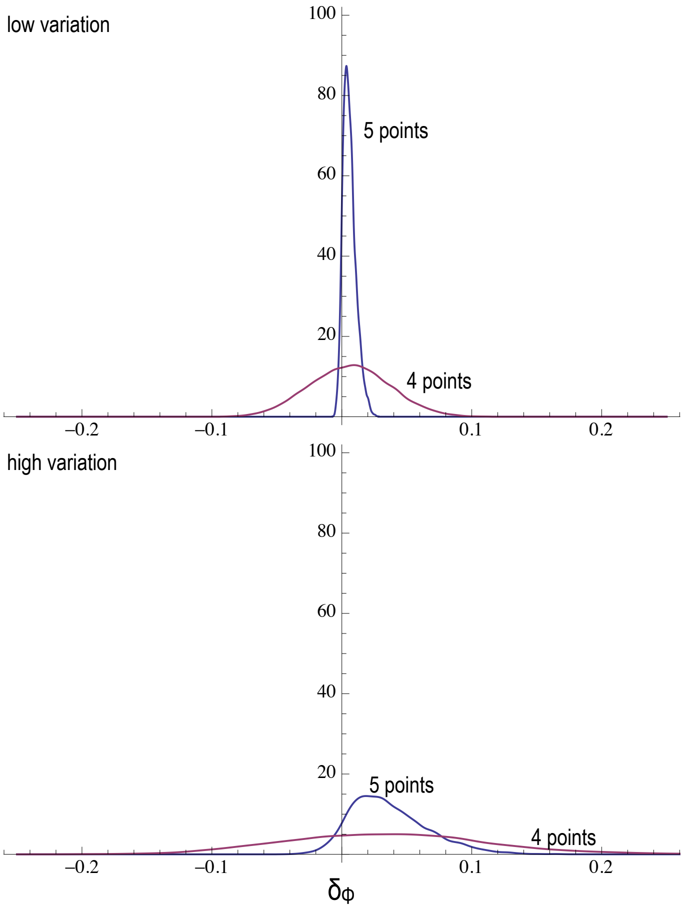

Figure 2.7: **Distribution of δ_ϕ** Distribution of $\delta_\phi \equiv \bar{r}/\bar{s} - 1/\phi$ for 10,000 trials of five randomly distributed points, with a low or high deviation from a regular pentagonal lattice, as described in Supporting Theory. For the same set of randomly distributed points, δ_ϕ was calculated incorporating all five adjacent and diagonal distances into the averages $\bar{r}$ and $\bar{s}$ (blue line) or only distances involving a 4 point subset (purple line). High deviation is similar to a "high temperature" scenario, and the 4 point subset is analogous to the K289M mutant. The energy required to shrink the average side length $\bar{r}$ will decrease for conformations with low δ_ϕ, according to Eq. **??**.

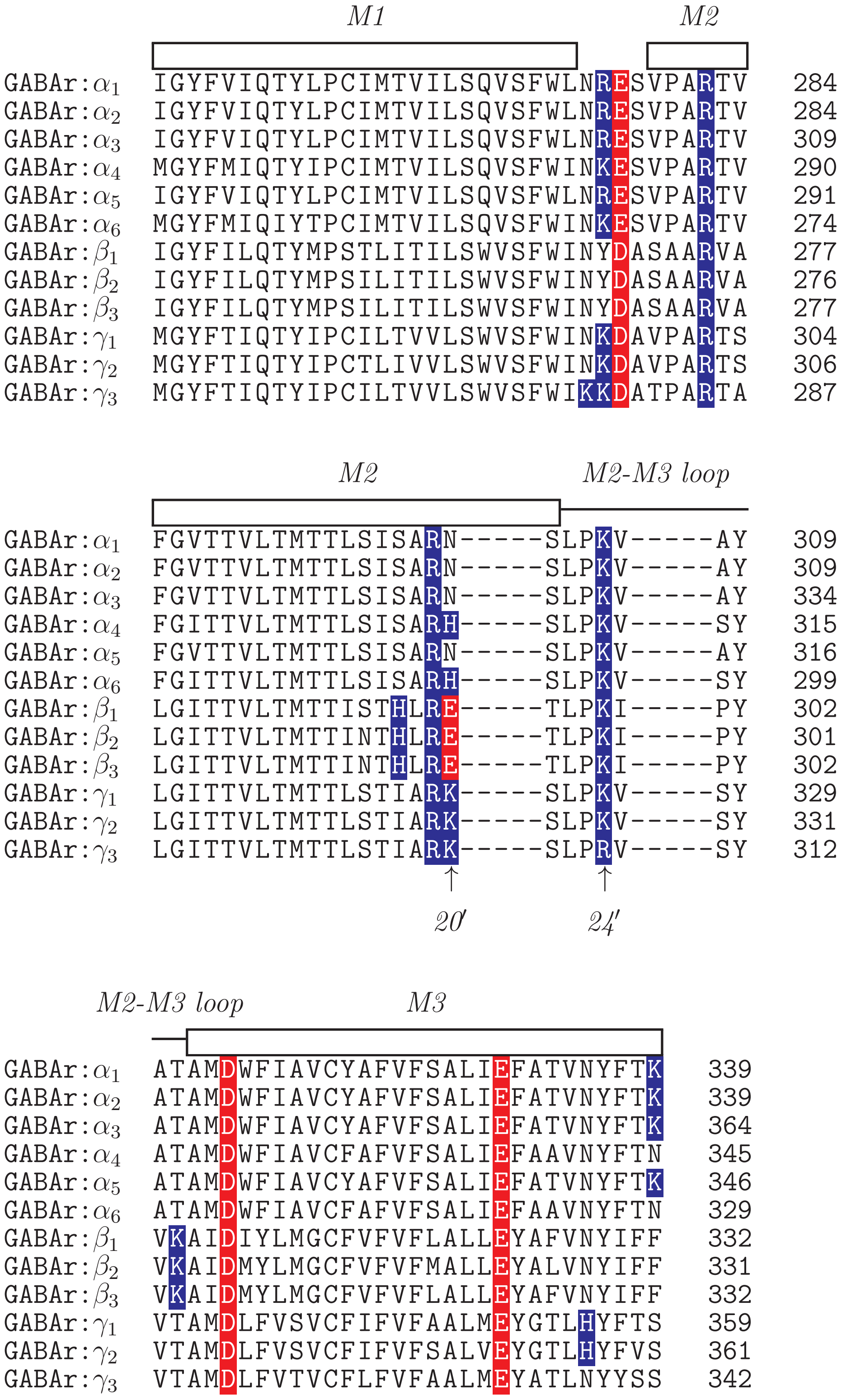

```
GABAr:α1  IGYFVIQTYLPCIMTVILSQVSFWLNRESVPARTV   284
GABAr:α2  IGYFVIQTYLPCIMTVILSQVSFWLNRESVPARTV   284
GABAr:α3  IGYFVIQTYLPCIMTVILSQVSFWLNRESVPARTV   309
GABAr:α4  MGYFMIQTYIPCIMTVILSQVSFWINKESVPARTV   290
GABAr:α5  IGYFVIQTYLPCIMTVILSQVSFWLNRESVPARTV   291
GABAr:α6  MGYFMIQIYTPCIMTVILSQVSFWINKESVPARTV   274
GABAr:β1  IGYFILQTYMPSTLITILSWVSFWINYDASAARVA   277
GABAr:β2  IGYFILQTYMPSILITILSWVSFWINYDASAARVA   276
GABAr:β3  IGYFILQTYMPSILITILSWVSFWINYDASAARVA   277
GABAr:γ1  MGYFTIQTYIPCILTVVLSWVSFWINKDAVPARTS   304
GABAr:γ2  MGYFTIQTYIPCTLIVVLSWVSFWINKDAVPARTS   306
GABAr:γ3  MGYFTIQTYIPCILTVVLSWVSFWIKKDATPARTA   287

GABAr:α1  FGVTTVLTMTTLSISARN-----SLPKV-----AY   309
GABAr:α2  FGVTTVLTMTTLSISARN-----SLPKV-----AY   309
GABAr:α3  FGVTTVLTMTTLSISARN-----SLPKV-----AY   334
GABAr:α4  FGITTVLTMTTLSISARH-----SLPKV-----SY   315
GABAr:α5  FGVTTVLTMTTLSISARN-----SLPKV-----AY   316
GABAr:α6  FGITTVLTMTTLSISARH-----SLPKV-----SY   299
GABAr:β1  LGITTVLTMTTISTHLRE-----TLPKI-----PY   302
GABAr:β2  LGITTVLTMTTINTHLRE-----TLPKI-----PY   301
GABAr:β3  LGITTVLTMTTINTHLRE-----TLPKI-----PY   302
GABAr:γ1  LGITTVLTMTTLSTIARK-----SLPKV-----SY   329
GABAr:γ2  LGITTVLTMTTLSTIARK-----SLPKV-----SY   331
GABAr:γ3  LGITTVLTMTTLSTIARK-----SLPRV-----SY   312

GABAr:α1  ATAMDWFIAVCYAFVFSALIEFATVNYFTK   339
GABAr:α2  ATAMDWFIAVCYAFVFSALIEFATVNYFTK   339
GABAr:α3  ATAMDWFIAVCYAFVFSALIEFATVNYFTK   364
GABAr:α4  ATAMDWFIAVCFAFVFSALIEFAAVNYFTN   345
GABAr:α5  ATAMDWFIAVCYAFVFSALIEFATVNYFTK   346
GABAr:α6  ATAMDWFIAVCFAFVFSALIEFAAVNYFTN   329
GABAr:β1  VKAIDIYLMGCFVFVFLALLEYAFVNYIFF   332
GABAr:β2  VKAIDMYLMGCFVFVFMALLEYALVNYIFF   331
GABAr:β3  VKAIDMYLMGCFVFVFLALLEYAFVNYIFF   332
GABAr:γ1  VTAMDLFVSVCFIFVFAALMEYGTLHYFTS   359
GABAr:γ2  VTAMDLFVSVCFIFVFSALVEYGTLHYFVS   361
GABAr:γ3  VTAMDLFVTVCFLFVFAALMEYATLNYYSS   342
```

Figure 2.8: **Conserved residues within GABA$_A$R subunits.** Alignment of M1, M2, M3 transmembrane helices and M2-M3 loop of α, β and γ subunits of human GABA$_A$R receptors. Residues are colored by charge at pH 7: negatively charged (red) and positively charged (blue). The 24' residue in the M2-M3 loop

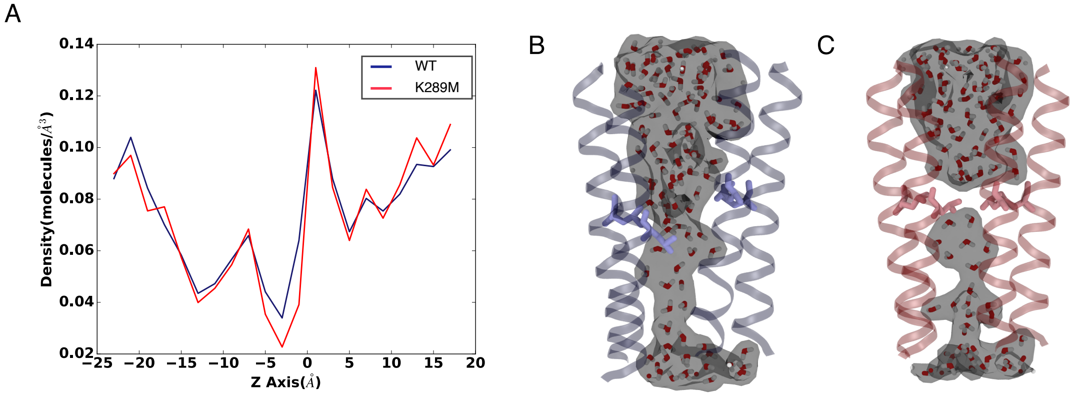

Figure 2.9: **Water density along the pore.** (A)Number of water molecules along the Z-axis averaged over the frames and replicas. Presence of water in the constriction region of the WT - M2 helices (B) as compared to the temporary dryness due to reduction in pore radii in the K289M - M2 helices(C), at higher temperature.

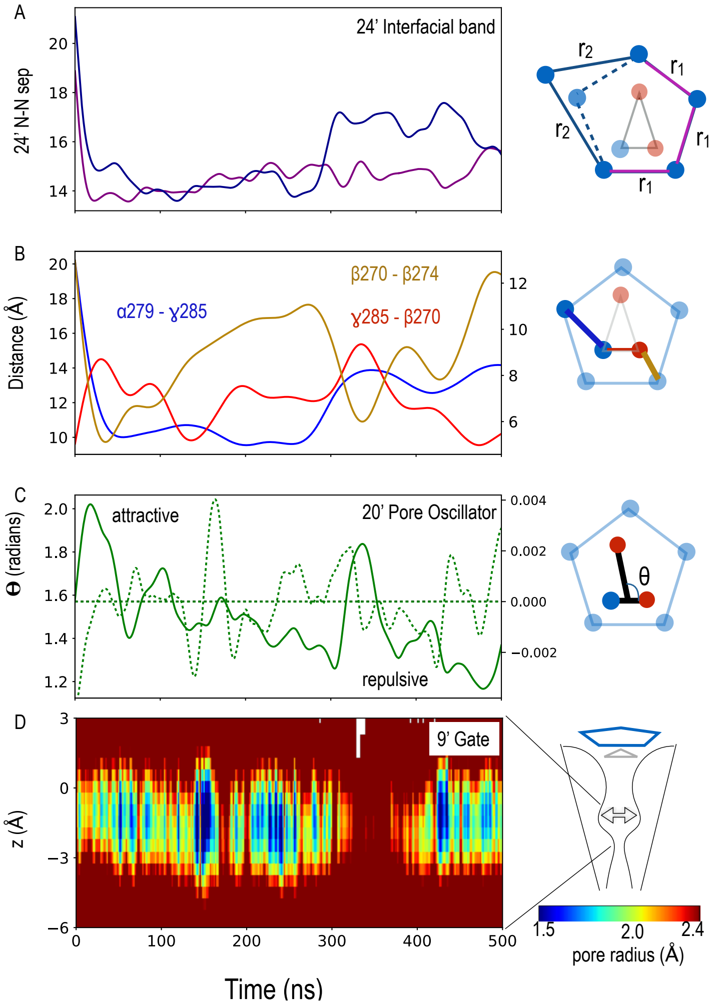

Figure 2.10: **Evolution of the interfacial band and pore oscillator in one replica of the WT system at 300K.** (A) Flip of one residue (α-K279) so the interfacial band switches from elongated to regular pentamer, occurs at $\sim$25 ns. (B) The distances between residues αK279 – γK285, plotted on y-axis and γK285 – β-K270, β-K270 – β-K274, plotted on alternate y-axis, are shown in blue, red and gold respectively. (C) The solid green curve depicts the angle between the charge-dipole arrangement representing the pore oscillator ; The Dotted green line represents the pore-opening event as measured by calculating the first derivative of the minimum pore radii. (D) Pore radius as a function of distance along the pore axis and time. All curves are smoothed as described in SI Methods.

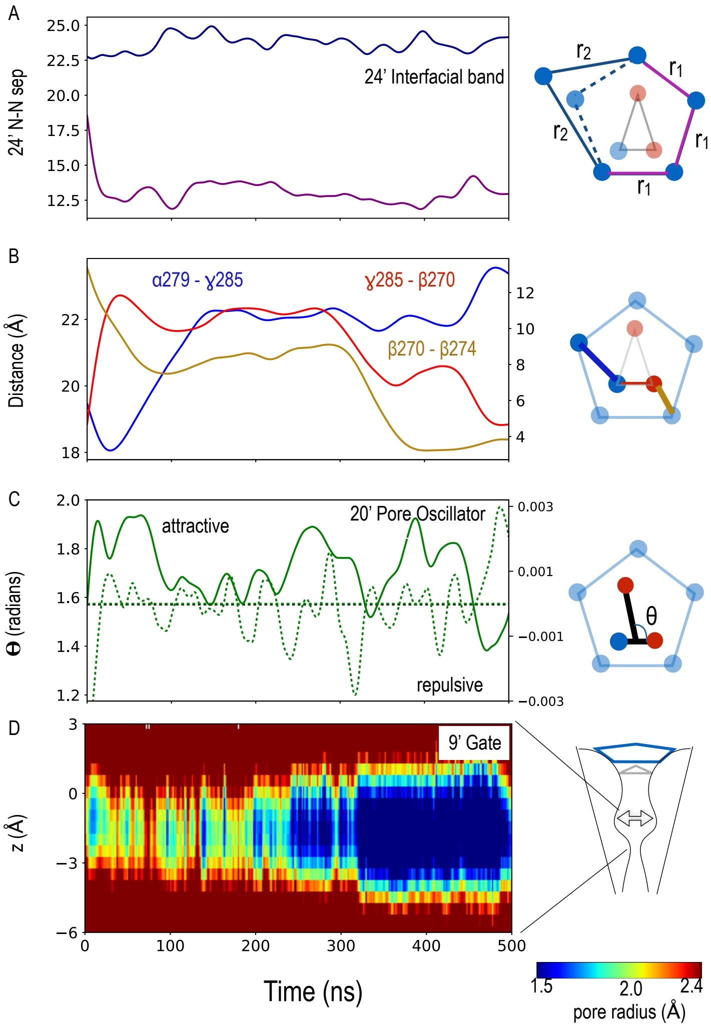

Figure 2.11: **Evolution of the interfacial band and pore oscillator in second replica of the WT system at 300K.** (A) Flip of one residue (α-K279) does not occur and the interfacial band remains in elongated pentamer form. (B) The distances between residues αK279 – γK285, plotted on y-axis and γK285 – β-K270, β-K270 – β-K274, plotted on alternate y-axis, are shown in blue, red and gold respectively. (C) The solid green curve depicts the angle between the charge-dipole arrangement representing the pore oscillator ; The Dotted green line represents the pore-opening event as measured by calculating the first derivative of the minimum pore radii. (D) Pore radius as a function of distance along the pore axis and time. All curves are smoothed as described in SI Methods.

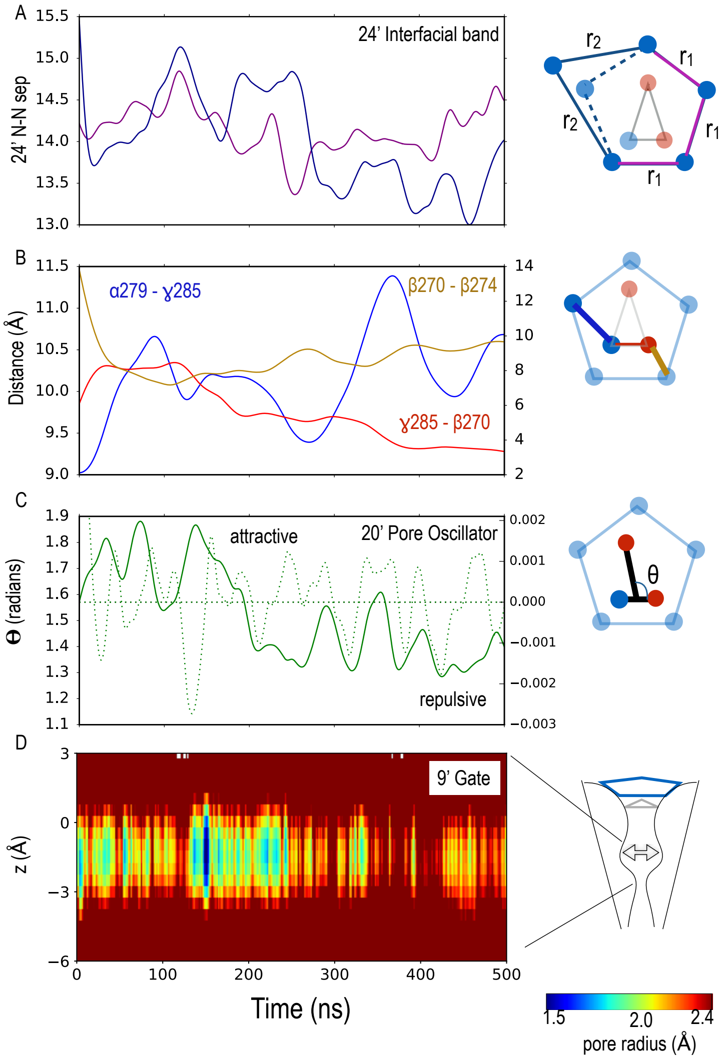

Figure 2.12: **Evolution of the interfacial band and pore oscillator in one replica of the WT system at 315K.** (A) Residue (α-K279) remains flipped from 300K simulations so the interfacial band remains in a regular pentamer form. (B) The distances between residues αK279 – γK285, plotted on y-axis and γK285 – β-K270, β-K270 – β-K274, plotted on alternate y-axis, are shown in blue, red and gold respectively. (C) The solid green curve depicts the angle between the charge-dipole arrangement representing the pore oscillator ; The Dotted green line represents the pore-opening event as measured by calculating the first derivative of the minimum pore radii. (D) Pore radius as a function of distance along the pore axis and time. All curves are smoothed as described in SI Methods.

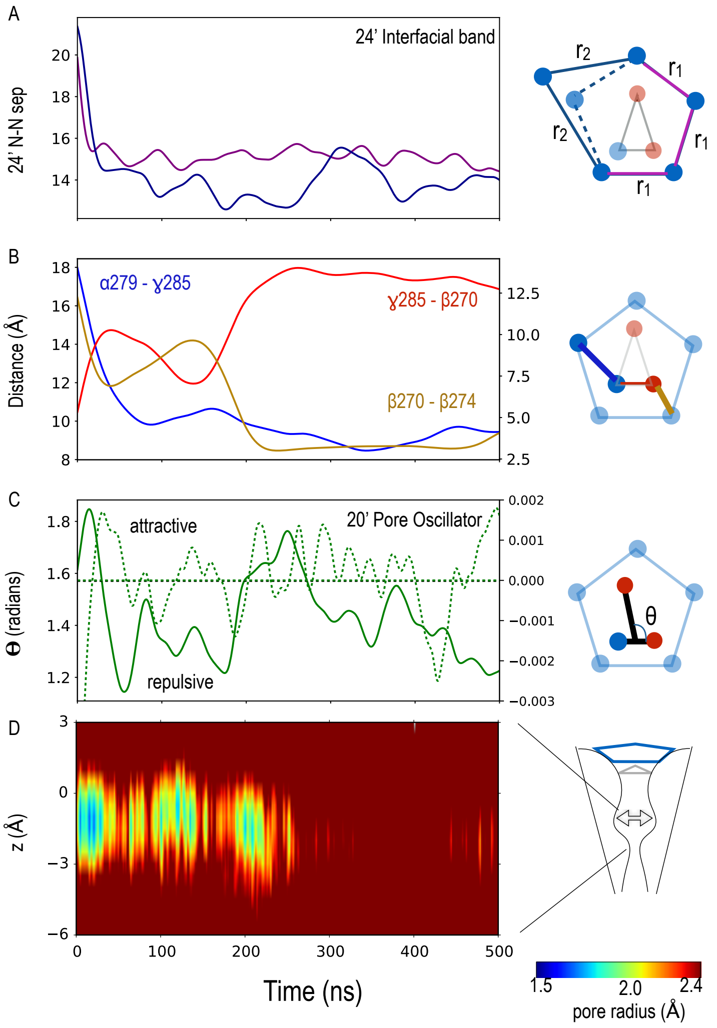

Figure 2.13: **Evolution of the interfacial band and pore oscillator in one replica of the K289M system at 300K.** (A) Flip of one residue (α-K279) so the interfacial band switches from elongated to regular pentamer, occurs at ~25 ns. (B) The distances between residues αK279 – γK285, plotted on y-axis and γK285 – β-K270, β-K270 – β-K274, plotted on alternate y-axis, are shown in blue, red and gold respectively. (C) The solid green curve depicts the angle between the charge-dipole arrangement representing the pore oscillator ; The Dotted green line represents the pore-opening event as measured by calculating the first derivative of the minimum pore radii. (D) Pore radius as a function of distance along the pore axis and time. All curves are smoothed as described in SI Methods.

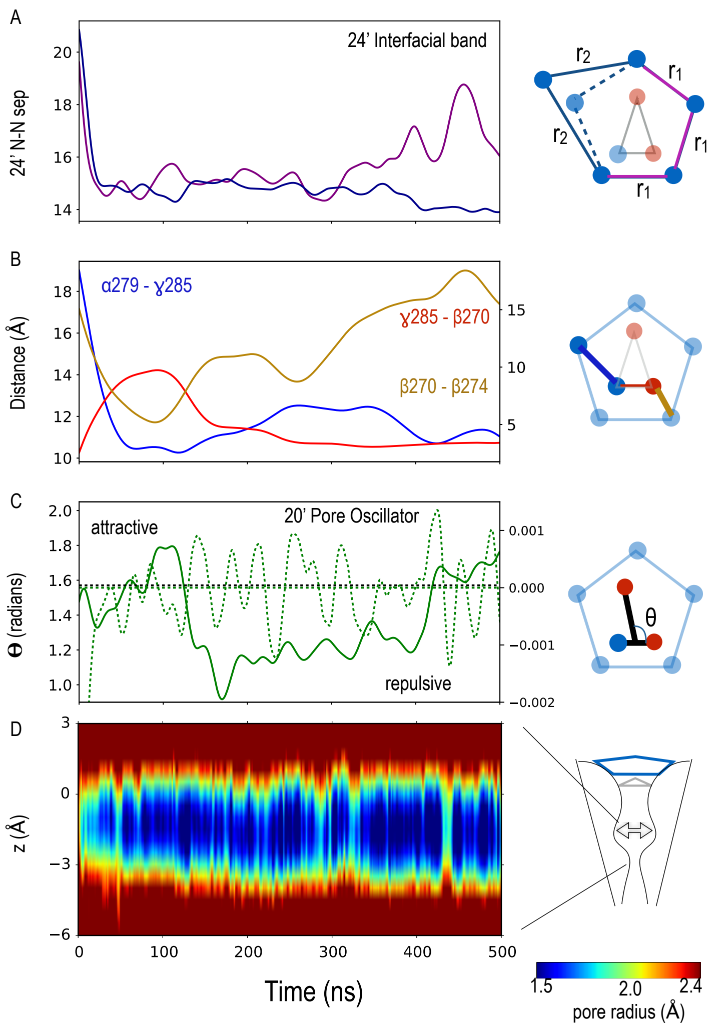

Figure 2.14: **Evolution of the interfacial band and pore oscillator in second replica of the K289M system at 300K.** (A) Flip of one residue (α-K279) so the interfacial band switches from elongated to regular pentamer, occurs at ∼25 ns. (B) The distances between residues αK279 – γK285, plotted on y-axis and γK285 – β-K270, β-K270 – β-K274, plotted on alternate y-axis, are shown in blue, red and gold respectively. (C) The solid green curve depicts the angle between the charge-dipole arrangement representing the pore oscillator ; The Dotted green line represents the pore-opening event as measured by calculating the first derivative of the minimum pore radii. (D) Pore radius as a function of distance along the pore axis and time. All curves are smoothed as described in SI Methods.

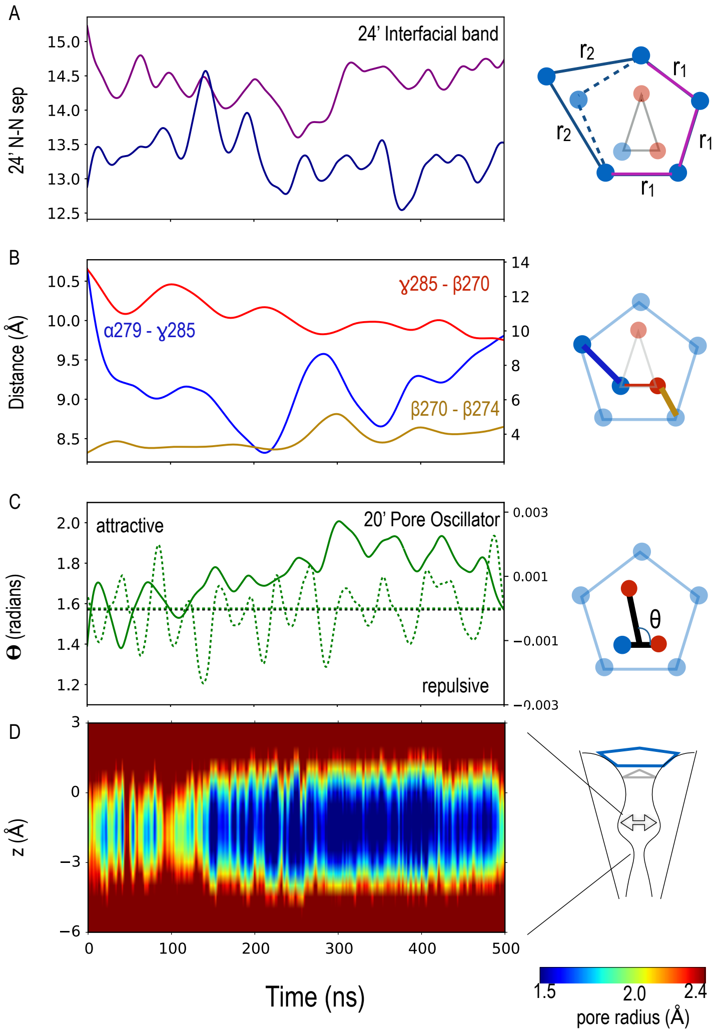

Figure 2.15: **Evolution of the interfacial band and pore oscillator in one replica of the K289M system at 315K.** (A) Residue (α-K279) remains flipped from 300K simulations so the interfacial band remains in a regular pentamer form. (B) The distances between residues αK279 – γK285, plotted on y-axis and γK285 – β-K270, β-K270 – β-K274, plotted on alternate y-axis, are shown in blue, red and gold respectively. (C) The solid green curve depicts the angle between the charge-dipole arrangement representing the pore oscillator ; The Dotted green line represents the pore-opening event as measured by calculating the first derivative of the minimum pore radii. (D) Pore radius as a function of distance along the pore axis and time. All curves are smoothed as described in SI Methods.

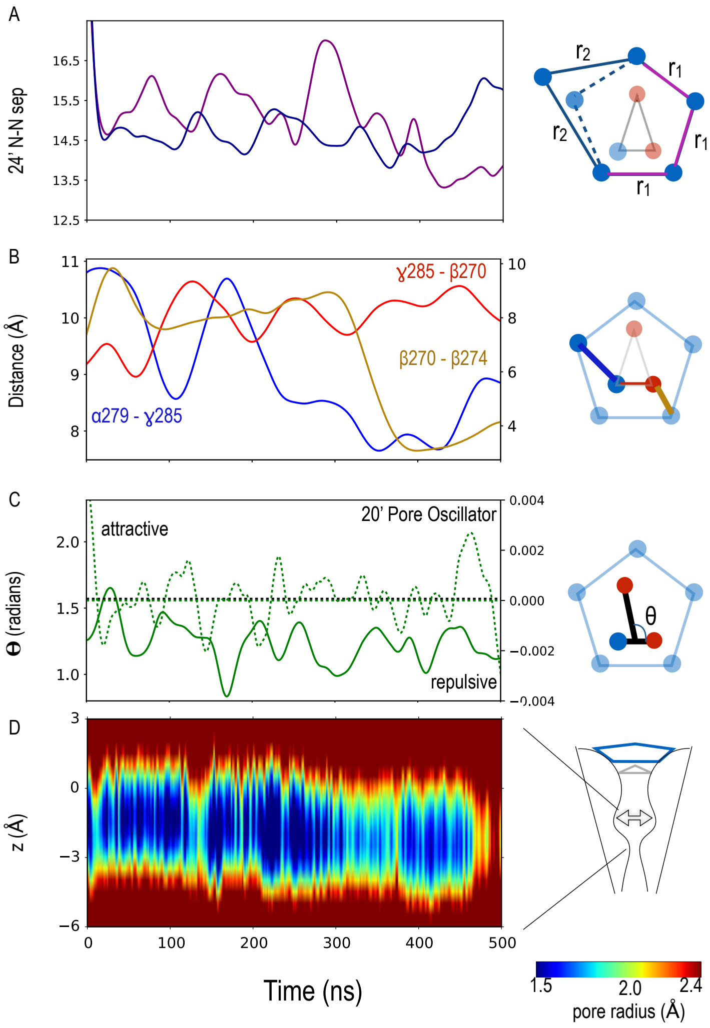

Figure 2.16: **Evolution of the interfacial band and pore oscillator in second replica of the K289M system at 315K.** (A) Residue (α-K279) remains flipped from 300K simulations so the interfacial band remains in a regular pentamer form. (B) The distances between residues αK279 – γK285, plotted on y-axis and γK285 – β-K270, β-K270 – β-K274, plotted on alternate y-axis, are shown in blue, red and gold respectively. (C) The solid green curve depicts the angle between the charge-dipole arrangement representing the pore oscillator ; The Dotted green line represents the pore-opening event as measured by calculating the first derivative of the minimum pore radii. (D) Pore radius as a function of distance along the pore axis and time. All curves are smoothed as described in SI Methods.

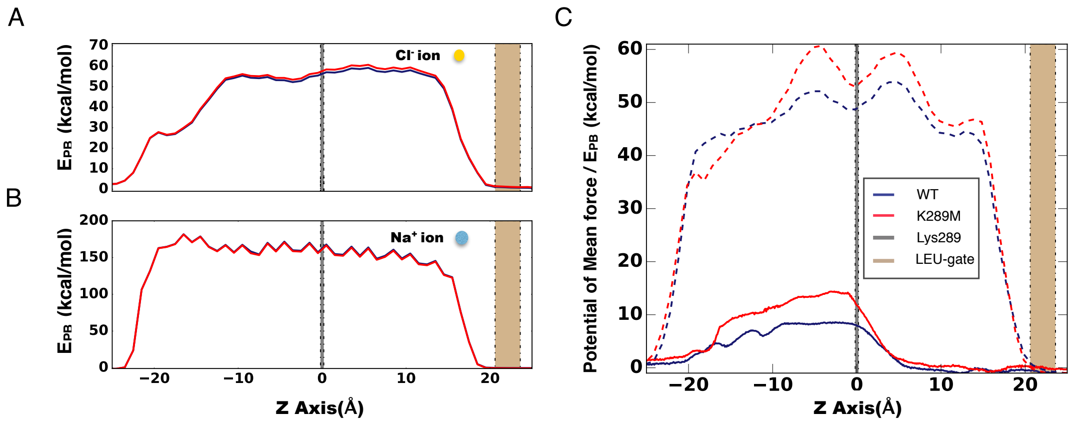

Figure 2.17: **Poisson-Boltzmann profile.** (A),(B)Electrostatic environment in the initial configuration of the channel as experienced by a chloride(A) and sodium(B) ion, obtained by performing a Poisson Boltzmann calculation along the TMD. (B)Average of the electrostatic barriers(dotted lines) for the translocation of Chloride ion, between WT and K289M replicas calculated over the final 50ns of the simulation at 315K, in comparison with the PMF (solid line) calculated using ABF simulations.

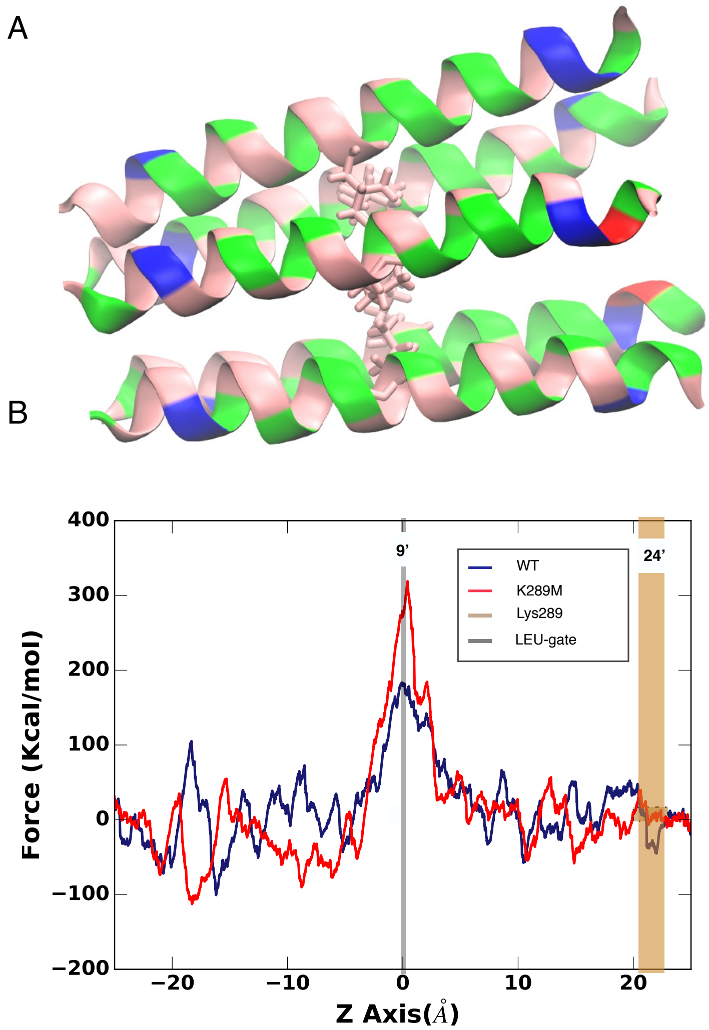

Figure 2.18: **Steered Molecular Dynamics.** (A) Snap-shot depicting the M2-helices (laid horizontally) showing the minimum constriction region flanked by LEU residues.(B) The force experienced by the ion as a function of position in the channel along the Z axis(TM domain), caluclated by performing SMD on a Chloride passing along the pore of the channel.

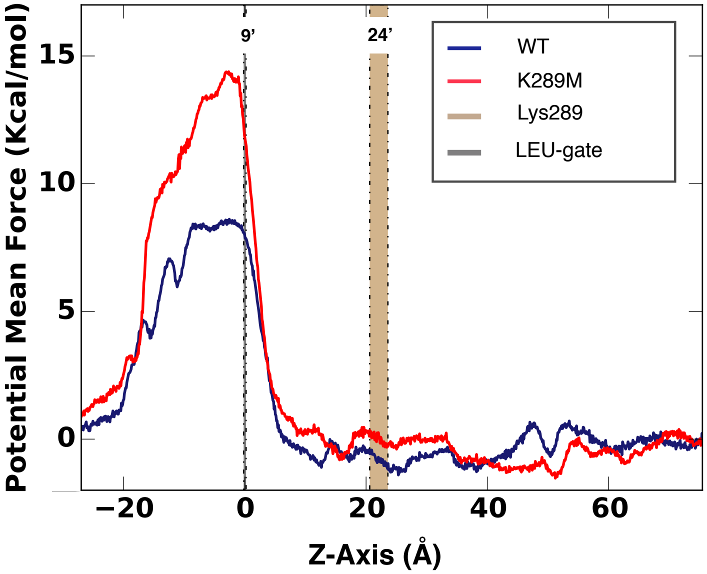

Figure 2.19: **Potential of Mean force.** (A) Potential of mean force profile of a chloride ion crossing the ion channel, calculated at 315K.

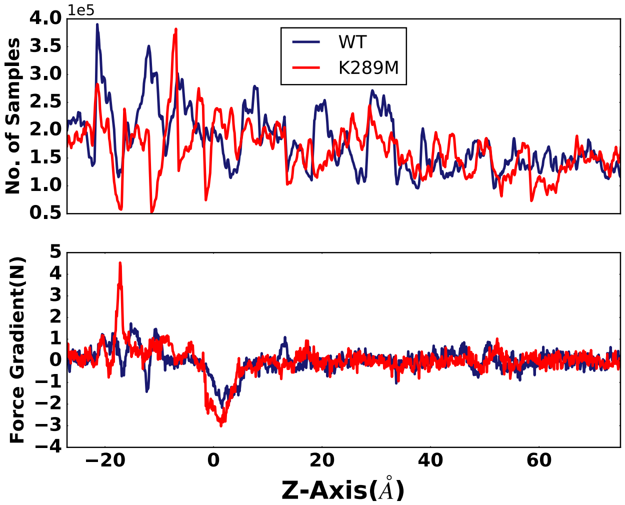

Figure 2.20: **ABF sample and gradient plots.** (A) Number of samples generated in each window of the ABF run. (B) Gradient of the force experienced by the ion in each window of the ABF run.

Chapter 3

Physical Accuracy Leads to Biological Relevance: Best Practices For Simulating Ligand-Gated Ion Channels Interacting With General Anesthetics.

3.1 Abstract

Efforts to detect binding modes of general anesthetics (GAs) for pentameric ligand-gated ion channels (pLGICs) are often complicated by a large number of indicated sites, as well as the challenges of ranking sites by affinity and determining which sites are occupied at clinical concentrations. Physics-based computational methods offer a powerful route for determining affinities of ligands to isolated binding sites, but preserving accuracy is essential. This chapter describes a step-by-step approach to multiple methods for identifying candidate sites and quantifying binding affinities, and also discusses limitations and common pitfalls.

3.2 Introduction

Pentameric ligand-gated ion channels (pLGICs) are widely-studied anesthetic targets, but present numerous challenges for structural characterization even in the apo state. EC_{50} of general anesthetics such as sevoflurane and propofol for pLGICs such as the GABA(A) receptor fall in the 100 mM to 1 μM range, and these low to moderate affinities introduce a high rate of false positives into most approaches. The ability to isolate binding sites offers an advantage to computational approaches, but one of the most common computational approaches, automated docking, is particularly unreliable on its own for interactions of GAs with pLGICs.

We have developed and refined a robust computational approach for identifying candidate binding sites, determining which binding sites are occupied at clinical concentrations, ranking them according to affinity, and determining the microscopic origins of differences in affinities. This approach considers all atoms of the system explicitly (GA, salt, lipids, water, and protein) and relies on the rigorous physics-based methods of Molecular Dynamics Simulation and Alchemical Free Energy Perturbation.

Our general process essentially involves two components : a screening or discovery phase to identify possible binding modes that might be occupied at clinical concentrations, and a quantification phase in which binding affinities are actually measured. This manuscript describes the steps to set up the necessary calculations and provides examples of the possible pitfalls in this process. This article is written with the CHARMM all-atom force field (**?**) and the NAMD molecular dynamics software (**?**)in mind, but the general approach is not forcefield or software specific. In this chapter we focus on a model of an $\alpha_1\beta_3\gamma_2$ GABA(A) receptor in a phosphatidylcholine (POPC) bilayer, interacting with the general anesthetics sevoflurane and propofol. The chapter assumes a general familiarity with the structure of pLGICs as well as the principles underlying classical molecular dynamics simulation.

3.3 MD simulation involving pLGICs

Setting up MD simulations follows a series of steps that are common for any pentameric channel with/without ligand. The CHARMM-GUI membrane builder website(**?**), a simulation input generator, accepts a protein structure file as input to embed the protein in a well-packed lipid bilayer with water molecules and neutralizing counter-ions on either side. For a system involving a pLGIC like the GABA(A) receptor, some of the important steps include:

- Choosing membrane builder from the input options.
- Setting up chain names (for non-protein molecules, like the anesthetic, the chain names should match the name mentioned in the topology files)
- Adding terminal patch groups to the protein N-terminus and C-terminus
- Preserving Hydrogen Coordinates
- Adding disulfide bonds.
- Specifying/Preserving protonation states, based on the desired pH of simulation.
- Choosing the right alignment of protein in the membrane. For a pentameric channel, choosing the option to align the 'first principle axis along Z ' would align the channel along Z axis, with the lipid in X-Y plane. Further, aligning the TMD region of protein with lipid involves translocating the protein until the pore center is at the box origin. It is advisable to check the orientation of the channel after this step, by clicking on the 'view structure ' option.
- Choosing the type of lipids for the bilayer and setting water thickness. We typically use the homogenous composition of POPC lipids and choose the default option of 1.5 layers in CHARMM-membrane builder for choosing the size the lipid membrane. There are ≈ 250 lipid molecules in GABA(A) receptor system and a water thickness of $20\mathring{A}$ is maintained at the top and bottom of the protein.
- Adding salt; we typically use 150mM of neutralizing NaCl.

The total number of atoms is typically between 140,000-200,000.

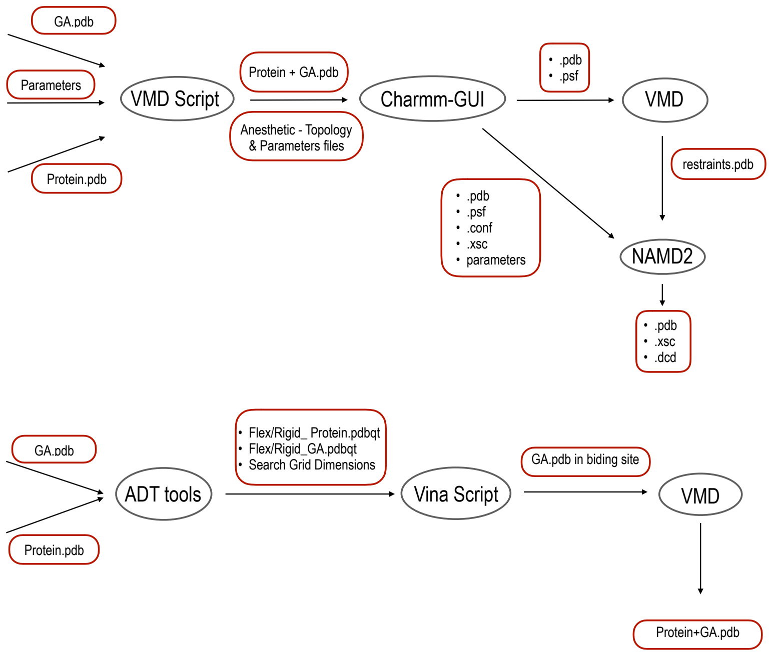
GA.pdb
Parameters
Protein.pdb
VMD Script
Protein + GA.pdb
Anesthetic - Topology & Parameters files
Charmm-GUI
• .pdb
• .psf
VMD
restraints.pdb
• .pdb
• .psf
• .conf
• .xsc
• parameters
NAMD2
• .pdb
• .xsc
• .dcd
GA.pdb
Protein.pdb
ADT tools
• Flex/Rigid_ Protein.pdbqt
• Flex/Rigid_GA.pdbqt
• Search Grid Dimensions
Vina Script
GA.pdb in biding site
VMD
Protein+GA.pdb

Figure 3.1: **Flowchart describing the sequential steps involved in performing.** (left) Flooding simulation and (right) Docking using Autodock and MD simulation

3.4 Discovery of Candidate Sites

We use two main approaches for identifying candidate binding modes: 1) Spontaneous Binding of GAs during equilibrium MD, also known as 'flooding' and 2) Docking followed by refinement using equilibrium MD. The former allows a blind, unbiased search for spontaneously occupied binding modes without targeting any particular region of the receptor, but is computationally very expensive, while the latter is primarily suitable when a specific region of the receptor is of interest. We consider each in turn:

3.4.1 Flooding Simulation

Flooding involves placing a high concentration of GA in the water surrounding the pLGIC (or, in some cases, the membrane) and allowing the GA to spontaneously partition into the membrane and protein binding sites over a simulation time that usually lasts 400 ns - 2μ s. It is most effective for small, relatively soluble ligands, and we have used this approach with isoflurane and nicotinic acetylcholine receptors and the prokaryotic homolog, GLIC(**?**) as well as sevoflurane interacting with GABA(A) receptors(**?**). It has also been used with ethanol interacting with glycine receptors(**?**) and interactions of GAs with voltage-gated channels(**?**).

Pre-requisites:

- Protein system in a water-box and lipid membrane (Procedure for this is elaborated under the previous section).
- Ligand in PDB format
- Parameters for ligand that are compatible with the forcefield used for water, protein, and lipids (see the chapter by Joseph and Henin in this volume).

Simulation setup :

- Initial Coordinates: Simulation should begin with a receptor embedded in a hydrated lipid bilayer with counter-ions and the GA molecules randomly distributed in the water. GA molecules can be randomly distributed around the receptor in the desired region of the simulation box using automated tcl scripts and VMD, and then the .pdb file containing both GAs and the receptor can be used as an input into the CHARMM-GUI membrane builder and system can be built as described in section **??**.

For a typical simulation box, a single GA molecule in aqueous phase corresponds to a concentration greater than 1 mM. To obtain a range of candidate sites over a reasonable simulation time, at least 20-100 GAs must be present in the simulation. Over the course of a flooding simulation, therefore, the concentration of GA in the aqueous phase may drop from 100mM down to 0-1mM, as GA molecules partition into the lipid phase. The poor correspondence between concentration in the simulation and *in vitro* or *in vivo* systems mandates the use of more sophisticated methods to predict likelihood of occupancy at clinical concentrations, as described subsequently; for a discovery stage, a higher than usual concentration is actually advantageous.

An example of sevoflurane being used to flood the GABA(A) receptor is shown in Figure **??**, with a sevoflurane-to-lipid ratio of about 1:3, and a sevoflurane-to-water molecule ratio of about 1:430.

- Non-default NAMD parameters:
    - minimize: This parameter denotes the number of timesteps to minimize the system. Since this simulation involves flooding the system with multiple anesthetic molecules, it is recommended to run longer minimization runs of 50,000 to 100,000 timesteps.
    - constraints: To avoid major changes to the backbone of the protein, this parameter can be set to “on” and a pdb file flagging the backbone atoms to be constrained under the parameters ‘conskfile’ and ‘consref.’ Typically the constraints are on the order of 5 kcal/mol/$\AA$ on the C_α atoms of the protein.

Analysis: Analyzing the trajectory of a flooding simulation using VMD, one could:

- Identify microscopic interactions between protein and anesthetic, including hydrogen bonds.
- Visualize the path of entry of ligand into the binding site.
- Estimate a residence time for a site in which the ligand binds and unbinds several times over the course of the simulation.
- Use VMD plug-in,'VOLMAP tool' to create images showing the average density of the ligand in multiple binding sites (Figure **??** B)
- Visualize the competitive binding between lipid and anesthetic as shown in Figure **??** (A).
- Identify sites likely to have multiple occupancy.
- Identify other binding sites not recognized by docking software. For instance, intra-subunit sites and multiple occupancy of specific sites were identified in flooding simulations with Sevoflurane as shown in Figure **??** (A).

Pitfalls: Some of the possible errors while setting up and running simulation involve:

- Incomplete PSF files being generated after GA is added to the protein, with overlapping the water molecules.
- Insufficient minimization or equilibration. Simulations must be run sufficiently long for GA molecules to partition into the lipid and access binding sites in the protein that may be deep.

Limitations: The high concentrations required can cause aggregation in GAs with poor solubility (such as propofol). It is also usually not practical to calculate concentration dependent occupancies because of the high concentrations required; AFEP methods described subsequently are essential for estimating features of dose-response.

3.4.2 Docking

Our approach usually limits use of automated docking to the generation of reasonably favorable binding modes in a particular region of a protein, as initial configurations for significant refinement via MD simulation. Scoring functions from automated docking are rarely meaningful as absolute values, but relative scores may be appropriate for suggesting the most favorable binding mode to use as an initial configuration. Although docking scores are often presented as binding affinities in units of kcal/mol, the method of assigning these units rarely involves an explicit calculation of interaction differences between bound and apo states. Docking scores *cannot* meaningfully be used to calculate a K_D in its usual meaning as the ligand concentration at which half the sites are occupied.

Pre-requisites:

- Receptor model and ligand in PDB format
- Particular region of the receptor of interest, such as the pore, a given subunit interface in the TMD, or the center of a given subunit.

Softwares used:

- Auto-dock Vina (**?**) is a docking algorithm that predicts a number of preferred orientations of ligand molecule bound to the protein and ranks them based on approximate scoring functions.

- VMD (**?**) is a software that allows us to visualize and analyze the protein-anesthetic complex following docking.

Docking setup:

- Initial Coordinates: Starting configurations for docking is a PDB structure of the protein and the ligand to be docked with, in the PDB format. In the Figure **??** we have docked sevoflurane and propofol to GABA(A) receptor system.
- Non-default Parameters: Docking can be performed from command-line prompt with a configuration file containing the following commands:
  - flex: Some side-chains of the channel can be made flexible and this part of the protein can be saved as a separate '.pdbqt' file, while the rigid part of the protein would be the argument for the previous command. Use of this command is to facilitate and focus docking in proximity to these 'flex' residues. The software further rotates these 'flex' residues to predict more number of orientations of the ligand at the docked site. This parameter is useful when there is prior knowledge regarding the location of possible binding sites, or specific residues present in the binding site. To select flexible residues, one can name the chain and the residue number into the dialogue box from the toolbar as show in Figure **??**B.
  - ligand : Input ligand in '.pdbqt' format. Similar to the receptor, the ligand can be loaded into Autodock tool, in '.pdb' format. Rotatable bonds/torsions must be set for the ligand molecule using the options from toolbar. This specifies the flexibility of the molecule; for propofol all bonds should be left as rigid.
  - center and size : Docking is most suitable when a particular region of the protein has been identified via other means, and this parameter

  can be used to limit the search space. For instance, the site of interest might be the intersubunit cavity around $\beta N265$, a residue which has been implicated numerous times for propofol ((**????**). (Figure **??**). Autodock-tools is useful for visualizing the search space over layed with the protein.

  - exhaustiveness: Docking consists of multiple individual runs starting from random conformations of the protein-ligand complex. The number of these runs depends on the flexibility of the ligand and the protein side-chains and can be controlled by this parameter. We use a value of 15 for this parameter, but also run multiple docking runs with the same parameters for a specific system.
  - nummodes: This parameter specifies the maximum number of binding poses to be generated. We use a value of 20 with multiple individual runs.

Pitfalls: Even with the precautions listed above, the ligand may be inherently unstable in the binding mode for a number of reasons. The two most common are:

- A ligand binding to an unoccupied binding site displaces solvent, and the overall stability depends not just on how the ligand interacts with the protein residues, but how solvent interacts with the protein, and how the ligand interacts with solvent. Automated docking algorithms do not take into account the latter in a rigorous way even for aqueous solvent. The situation is even worse when the site fills with lipid acyl chains in the absence of ligand, as GA sites on pLGICs often do; in many cases a GA can compete much more favorably with water than with an acyl chain, and docking programs will overestimate the favorability of such a binding mode.

  As a result, it is not uncommon for GAs to migrate far enough from a docked location even in shorter ($\sim$ 100 ns long) MD simulations that contact residues are entirely different between the initial and final frame. For example, AutoDock typically returns a binding mode for sevoflurane that is particularly far from the extracellular domain (Figure **??**), but in MD simulation, sevoflurane reliably migrates to a site much more similar to that for propofol. Rigorous calculation of affinities using AFEP identifies the latter binding mode as much more favorable than the initial docked conformation.

- The docking algorithm usually uses flexible ligands, with an energy associated with rotation around bonds. Configurations for Propofol in which the hydroxyl clashes with the isopropyl group do not actually have unfavorable dihedral angles and many docking programs will not identify this clash as unfavorable, returning a propofol conformation in which the hydroxyl is overlapping the isopropyl (Figure **??**). This can introduce an instability or rapid unbinding in the MD simulation (Figure **??** (A,B)), depending on how equilibration is carried out. For this reason, we strongly recommend removing ligand flexibility when docking with propofol.

3.4.3 Running Molecular Dynamics Simulation

Several of the limitations of automated docking can be overcome by refinement with unbiased MD simulation, and if possible, it is almost always advisable to do so before drawing conclusions about microscopic interactions or calculating binding affinity.

Pre-requisites:

- Docked protein-anesthetic complex

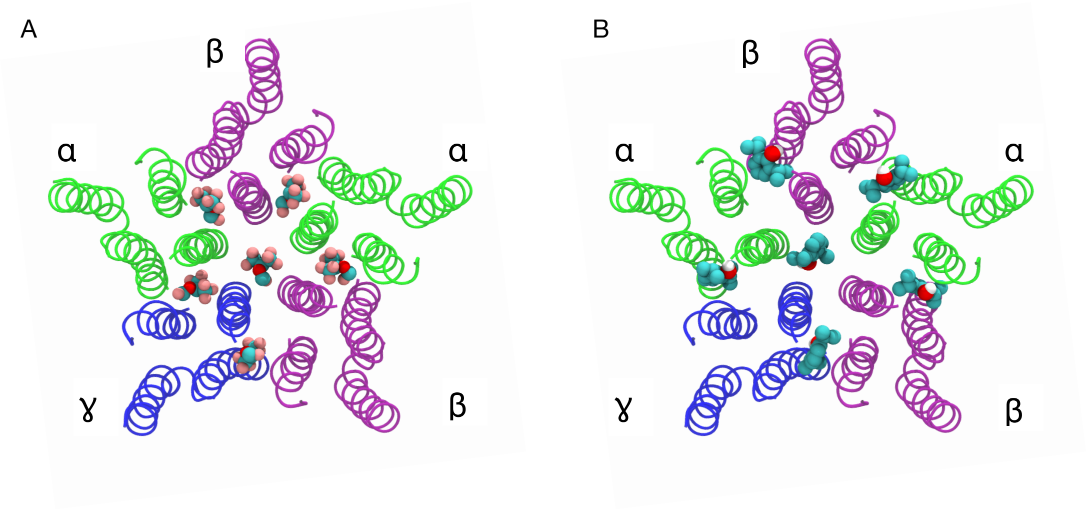

Figure 3.2: **View of the TM domain, looking down on the membrane from the extracellular region.** Sevoflurane(A) and Propofol(B) docked to the TMD of GABA(A) receptor. Docking was individually performed at all the inter-subunit sites and the pore by making few of the protein residues, flexible. For instance, at the α-β site, βMET289 residue side-chain was made flexible while docking to this interface.

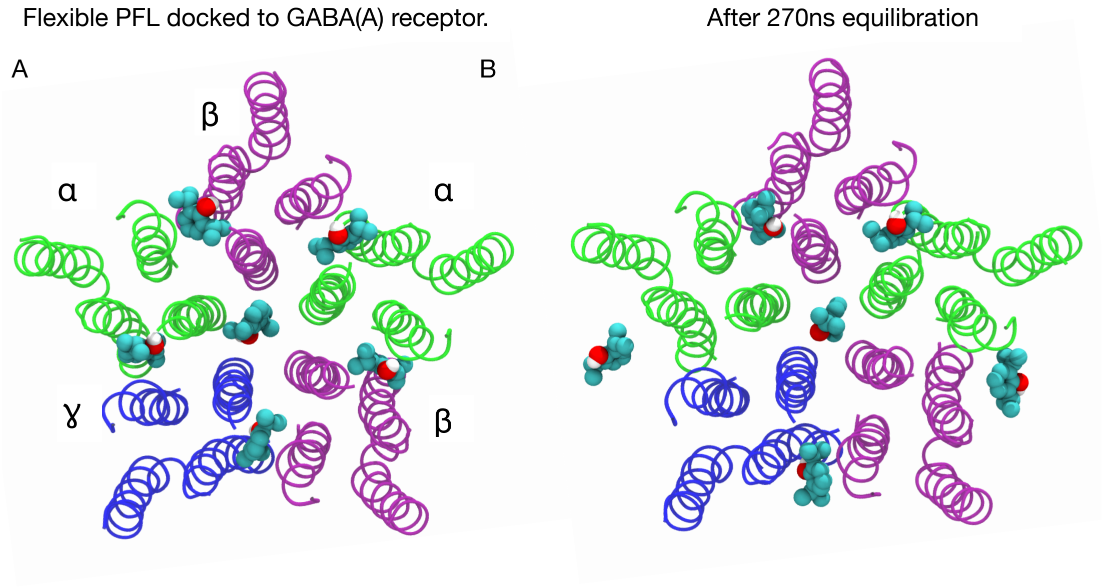
Flexible PFL docked to GABA(A) receptor.
After 270ns equilibration
A
B
β
α
α
γ
β

Figure 3.3: **View of the TM domain, looking down on the membrane from the extracellular region.** MD of PFL-GABA(A) receptor system, images depict the position of Propofol at initial and final frames of the trajectory. Unfavorable conformation of Propofol led to expulsion of the ligand in the course of the simulation.

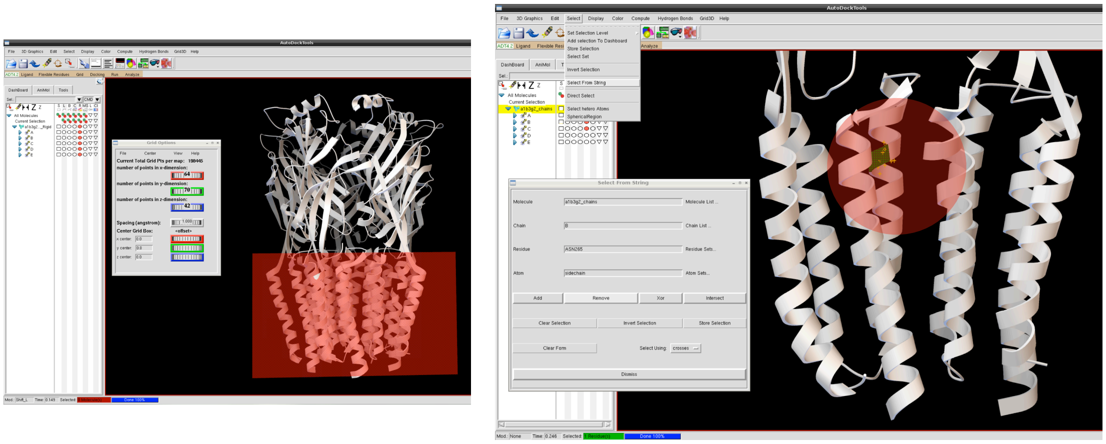
AutoDockTools
Grid Options
File
Center
View
Help
Select From String
Molecule List ...
Chain List ...
Residue Sets...
Atom Sets...
Add
Remove
Xor
Intersect
Clear Selection
Invert Selection
Store Selection
Clear Form
Dismiss

Current Total Grid Pts per map: 198445
number of points in x-dimension: 64
number of points in y-dimension: 70
number of points in z-dimension: 42
Spacing (angstrom): 1.000
Center Grid Box: <offset>
x center: 0.0
y center: 0.0
z center: 0.0

Molecule: a1b3g2_chains
Chain: B
Residue: ASN265
Atom: sidechain
Select Using: crosses

Mod.: None Time: 0.246 Selected: 1 Residue(s) Done 100%

Figure 3.4: **Screenshot of Autodock tools screen depicting a dialogue box describing.** (A) the measurements of the grid box over the TMD of the protein and (B) the process of selecting the flexible residues in the protein.

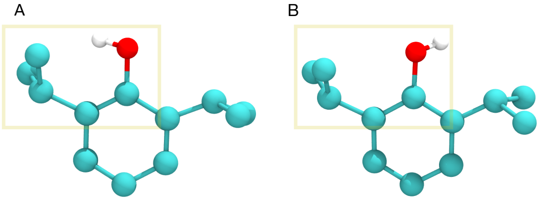

Figure 3.5: **Low and high energy conformation of Propofol.** Comparison between an unfavorable (A) and favorable low energy (B) conformation of Propofol.

- Parameters for the anesthetic.

Simulation Setup:

- Initial Coordinates: Starting configurations for the simulation would be anesthetics docked to binding sites in the protein, generated using docking software.The protein-anesthetic complex can be used as an input to the CHARMM-GUI membrane builder website(**?**) to build the system.
- Non-default Parameters: restartfreq, dcdfreq, xstFreq, outputEnergies and outputTiming: These parameters denote the number of timesteps between which each output is generated. By default, the configuration files generated by CHARMM membrane builder has these parameters set to 125 or 500 timesteps. A frequency of 5000 timesteps is ideal for further analysis unless a much lower frequency is required.

Analysis: Running the simulation for a considerable about of time (≈ 200-500ns) , one has to analyze the dynamics before setting up FEP simulations. Initial analysis include:

- Checking the stability/mobility of the ligand in the binding site. This can be done by tracking the location of the center of mass (COM) of the ligand in the site throughout the trajectory, using tcl scripts in VMD. Dispersion in the COM is essential to estimate prior to constructing spherical restraints for the ligand while setting up FEP calculations.
- Visualizing microscopic interaction between ligand and its environment. For example, on loading the trajectory into VMD, one can make following selections for a ligand with resname PFL:
    - "(protein and within 3 of (resname SEV)) or (resname PFL)". Making the representation as H-Bonds would allow us to view the hydrogen bonds formed between protein and the ligand (Figure **??**).

  - “(protein or lipid or water) and same residue as within 4 of (resname PFL)”. This selection would let us see the interactions among the protein residues, water, lipids and the anesthetic, in the binding site. Analyzing these interactions may provide insight into the affinity (obtained through AFEP) of the anesthetic to a specific site, as in (**?**).

- Identifying higher affinity sites, compared to the sites identified through docking. In the case of sevoflurane docked to a GABA(A) receptor, the low specificity and smaller size of the anesthetic results in greater mobility in the binding site, thus allowing it to explore/move to higher affinity sites as shown in Figure **??**.

- Ensure the bound anesthetic is in its favorable/low-energy conformation. In case of docked to GABA(A) system, docking with an unfavorable conformation of propofol (Figure **??**) led to immediate expulsion of the molecule as the simulation began. This is described by depicting few snap-shots from the simulation in Figure **??**, and this issue can be overcome by removing propofol flexibility during the docking process.

Pitfalls: Some of the common pitfalls encountered during setting up a simulation are:

- Not adding necessary disulphide bonds while setting up the system in CHARMM-GUI.

- Inaccurate protonation states of amino acids at pH 7.

- Not confirming the proper alignment of the protein in the lipid membrane.

- Mismatch in names of the GA atoms in the pdb file and topology file.

- Ligand should have a separate chain name different from the rest of the protein, to be recognized as HETATM by CHARMM-GUI.

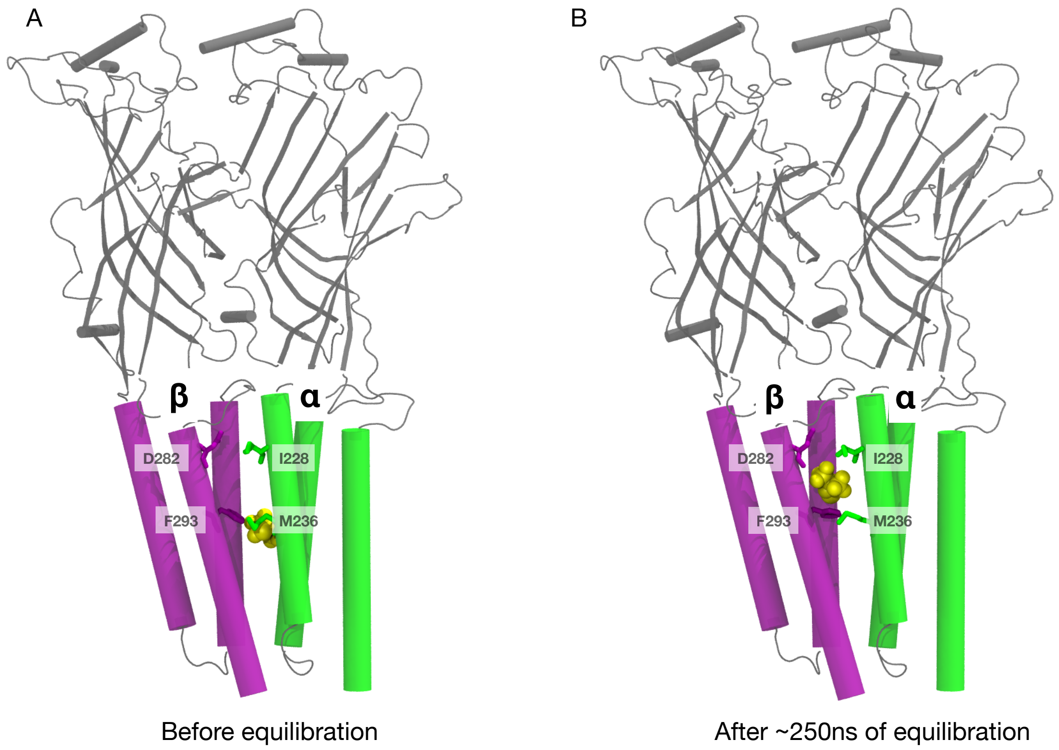
A
β
α
D282
I228
F293
M236
Before equilibration
B
β
α
D282
I228
F293
M236
After ~250ns of equilibration

Figure 3.6: **Side view of the sevoflurane in the β-α interface of the GABA(A) receptor system.** Two images depicting the docked (A) and equilibrated conformation (B) of the system. Equilibration of the docked conformation allows Sevoflurane to re-orient itself at a higher affinity site.

Limitations: Inability to witness lipid mixing or domain formation around the receptor in a mixed membrane. This would require extensively long simulations or can be achieved thorough coarse-graining simulations.

3.5 Calculation of Binding Affinities

Following the identification of a stable binding mode for the anesthetic, the binding affinity can be rigorously calculated using a theoretically exact simulation technique called Alchemical Free Energy Perturbation (AFEP) that relies on the

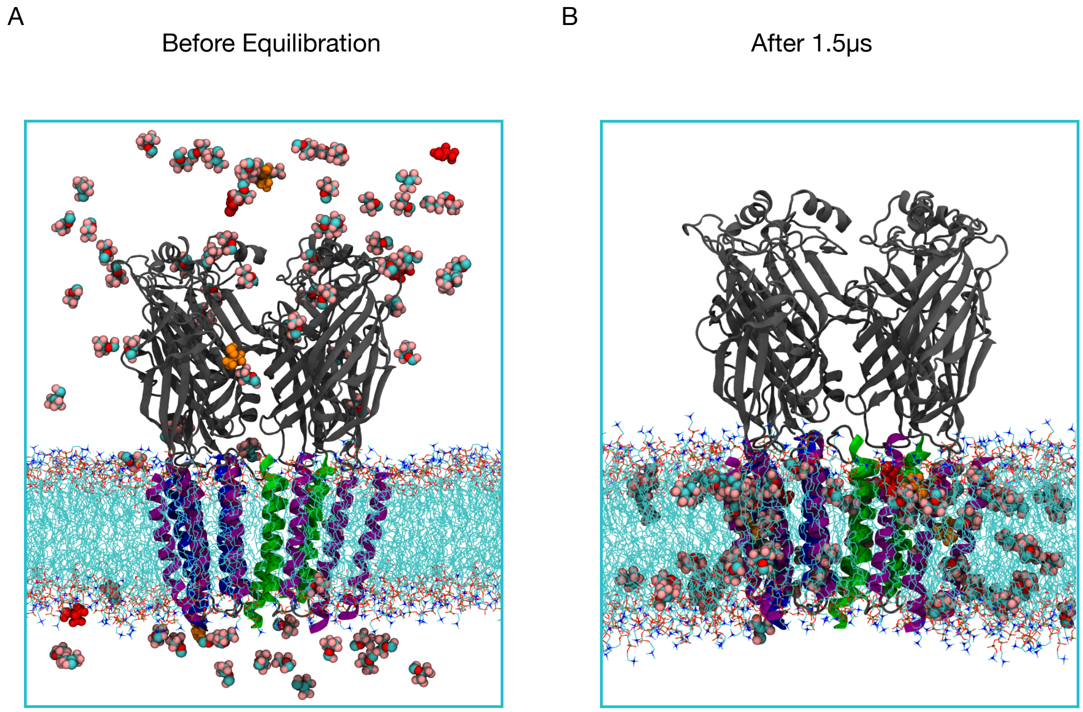

Figure 3.7: **Cross-sectional view of the Sevoflurane flooded GABA(A) receptor system with the TMD aligned along POPC lipid membrane(colored by name) and placed in a box of explicit water (molecules not shown, represented as a blue box).** (A) Initial frame with Sevoflurane(colored by name) flooded in the water; After 1.5μs Sevoflurane completely localizes in the lipid membrane with some binding the inter and intra-subunit sites(red and orange) in the TMD.

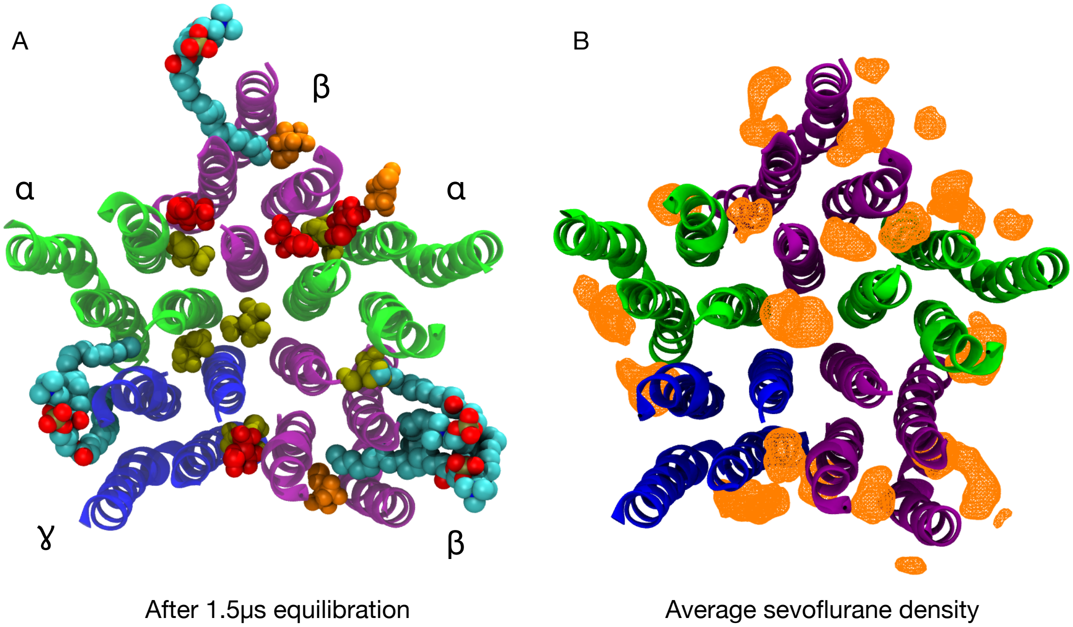

Figure 3.8: **View from the extracellular domain, of a Sevoflurane flooded GABA(A) receptor system.** (A) Final frame from the flooding simulation showing sevoflurane occupying the inter, intra and pore sites(Red, orange) overlaid with sevoflurane(yellow) docked using Auto-dock; Flooding simulation also identified lipid (colored by name) interference in β intra-subunit site and and α-γ, α-β intersubunit sites. (B) Image created using VMD plugin, VOL-MAP tool, to depict the density isosurface (orange) averaged over the last 700 ns of the simulation; large mesh represent occupation over majority of the trajecotory, whereas a few smaller mesh represents occupation for lesser time.

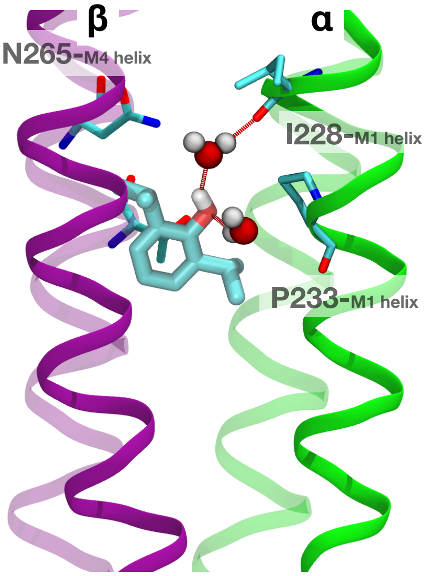
β
α
N265-M4 helix
I228-M1 helix
P233-M1 helix

Figure 3.9: **Propofol bound to an intersubunit site.** Depiction of Propofol interacting with water and protein side-chains at the $\beta-$-$\alpha+$ intersubunit site, in a snapshot from a MD simulation.

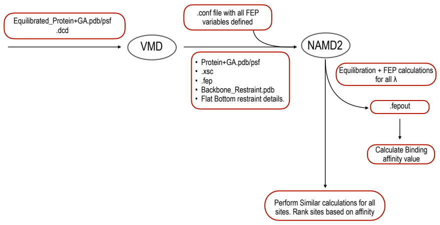
Equilibrated_Protein+GA.pdb/psf
.dcd
VMD
.conf file with all FEP variables defined
NAMD2
• Protein+GA.pdb/psf
• .xsc
• .fep
• Backbone_Restraint.pdb
• Flat Bottom restraint details.
Equilibration + FEP calculations for all λ
.fepout
Calculate Binding affinity value
Perform Similar calculations for all sites. Rank sites based on affinity

Figure 3.10: **Flowchart for FEP.** Flowchart describing the sequential steps involved in calculating binding affinity of anesthetics

equation introduced by Zwanzig(**?**) for calculating the difference in Helmholtz free energy between two states, X and Y:

$$\Delta A_{X\rightarrow\ Y} = -RT \ln \left\langle e^{-(H_Y(\mathbf{r})-H_X(\mathbf{r}))/RT} \right\rangle_X \tag{3.1}$$

where R is the gas constant, T is temperature, $H(\mathbf{r})$ is the Hamiltonian for state X or state Y. In a binding free energy application, X would represent the bound state, Y would represent the apo state, and $\Delta A_{X\rightarrow\ Y} \sim \Delta G_{X\rightarrow\ Y}$ because ligand binding will not significantly change the system volume. In practice (**??**) for convergence purposes this is carried out by summing over a series of windows in which the interaction between the ligand and all other atoms of its environment are gradually decreased to zero:

$$H_{\lambda_i} = H_{\text{env}} + H_{\text{lig}} + (1-\lambda_i)H_{\text{env}-\text{lig}}, \tag{3.2}$$

where $\lambda = 0$ is equivalent to the bound state X, $\lambda = 1$ is the unbound state Y, $0 <= \lambda_i < 1$ for all i and $\lambda_i < \lambda_{i+1}$. The free energy change for "decoupling" the ligand from its environment is

$$\Delta G_{\text{env}} = -RT \sum_i \ln \left\langle e^{-(H_{\lambda_{i+1}}(\mathbf{r})-H_{\lambda_i}(\mathbf{r}))/RT} \right\rangle_{\lambda_i} = -RT \sum_i \ln \left\langle e^{-(\lambda_i-\lambda_{i+1})H_{\text{env}-\text{lig}}/RT} \right\rangle_{\lambda_i}. \tag{3.3}$$

Treating the coupled ligand as the bound state requires that the fully coupled ensemble (at $\lambda = 0$) includes no states with ligand outside the binding site. This assumption can breakdown for moderate affinity ligands like GAs, but can be resolved by making the requirement of localization to the binding site explicit, via a restraint potential on the ligand center of mass.

A flat-well potential that vanishes within the binding site but is very high outside the binding site accomplishes this with minimal need for correction, and also alleviates convergence problems for windows close to $\lambda = 1$ (fully decoupled). The standard binding affinity is

$$\Delta G^0 = \Delta G_{\text{site}} - \Delta G_{\text{solv}} - k_BT \ln(V_{site}/V^0) \tag{3.4}$$

where ΔG_{site} is free energy of decoupling from environment of the protein binding site, ΔG_{bulk} is the free energy of decoupling ligand from bulk solvent(solvation free energy), V_{site} is the volume accessible to the center of mass of the bound ligand (as specified by Eq. **??**), and $V^0 = 1661\text{Å}^3$ is the accessible volume per molecule in a 1M solution. Although this method is theoretically exact and all degrees of freedom are considered automatically by the method, the success and inherent challenge of the technique relies on obtaining reasonable convergence of each average in Equation **??**.

Pre-requisites:

- Starting configuration from MD simulation.
- PDB files indicating the atoms/ligands to be unbound/decoupled.
- Restraint files indicating the type of restraints to be applied to the movement of the ligand during the simulation.
- Solvation free energy of the anesthetic. This involves, decoupling the ligand from bulk solvent in the absence of protein. This is required to calculate the free energy cost of moving the ligand from bulk solvent to a binding site in the protein.

Simulation Setup :

- Initial coordinates: Starting coordinates should be taken from the output of a fully interacting equilibrium MD simulation, as described in the previous section.
- Non-default parameters:

- alchEquilSteps : the number of steps at the beginning of each alchemical window that is excluded in the cumulative average used to calculate $\Delta\Delta G_i \equiv -RT \ln \left\langle e^{-(\lambda_i - \lambda_{i+1}) H_{\text{env}-\text{lig}}/RT} \right\rangle_{\lambda_i}$ for window i, to allow the system to adjust to the new value of λ. We typically use values of 25000 to 50000 steps to balance the need for equilibration time with need for actual samples. It affects on-the-fly analysis but not the actual trajectory, and different values can be used in post-processing.
- alchElecLambdaStart : the value of λ for which the electrostatics should be entirely switched off, through the soft-core potential necessary for FEP calculations. We use the value of 0.5 recommended by the NAMD User‘s guide (**?**).
- alchVdwLambdaEnd : the value of λ for which the Van der Waals interaction should be entirely switched off, through the soft-core potential necessary for FEP calculations. We use the value of 1.0 recommended by the NAMD User‘s guide (**?**).
- alchDecouple : This parameter specifies whether either intermolecular interactions of the anesthetic are turned ‘off’ (decoupling) or both inter and intra-molecular interactions are turned ‘off’ (annihilation). By default this parameter is set to ‘off’ which chooses the annihilation option. We use the decoupling method, i.e, set the parameter ‘on’ as the intramolecular annihilation free energies simply get canceled when the solvation free energy is subtracted.
- alchLambda/alchLambda2 : Every configuration file would have different values for λ, denoting the progress of the perturbation. We typically use windows with $\lambda_{i+1} - \lambda_i = 0.05$ for λ between 0 and 0.8 and $\lambda_{i+1} - \lambda_i = 0.025$ for λ between 0.8 and 1.0. These values can be modified during re-runs to improve sampling.

- Additional files:
  - Restraint file: We use flat-bottom spherical restraints for the inter and intrasubunit sites with the following potential:

$$U_{rest}(\vec{r}_{COM}) = \begin{cases} \frac{k(\vec{r}_{COM}-R)^2}{2}, & |\vec{r_0} - r_{COM}| > R \\ 0, & |\vec{r_0} - r_{COM}| <= R \end{cases} \tag{3.5}$$

    where $\vec{r}_{COM}$ is the ligand center of mass, $\vec{r_0} = \langle \vec{r}_{COM} \rangle$ in the fully coupled and bound state, and $R = \max(|\vec{r_0} - r_{COM}|)$ in the fully coupled and bound state. Both $\vec{r_0}$ and R can be determined from Equilibrium MD simulations, and determine the value $V_{site} = 4/3\pi R^3$.

    Typical values of k are 5 kcal/mol/Å. For pore sites we adjust Equation **??** to represent a cylindrical site by applying separate potentials on the vertical and radial coordinates. In NAMD, these restraints can be implemented using tclForces or the collective variables module, both of which require an additional file. For simple geometries, using tclForces tends to be computationally faster and is implemented using the parameter 'tclForces' in the configuration file.
  - FEP file : PDB file used to denote the atoms that are to be decoupled. Can be generated using VMD, where the 'beta' column in the PDB file can be flagged with number '-1.00' for outgoing atoms and '1.00' for incoming atoms.

Analysis:

- Multiple FEP runs with same or different starting configurations can be performed to check the consistency of the results.
- Performing a recoupling run(ligand-unbound state to bound state) followed by decoupling and combining the results using BAR or SOS estimator to obtain more accurate binding energy value.

- Understanding the affinity values obtained. The standard free energy of binding is related to the dissociation constant K_D via,

  $$\Delta G^0 = RT \ln K_D \tag{3.6}$$

  Any K_D value that is smaller (stronger) than the EC_{50} of a GA indicates the site may be essential to action of the GA. Previously we used measured K_D for isoflurane in the GLIC pore to argue that inhibition by isoflurane likely occurred via pore block rather than an allosteric mechanism;(**?**) although there is still no available crystal structure for isoflurane bound to GLIC, crystal structures released several years later confirmed pore block as the dominant mechanism for a homologous prokaryotic channel, ELIC(**?**). Similarly, we were able to rank K_D for propofol interacting with GABA$_A$r subunit interfaces, with sites containing α and β subunits having K_D <EC$_{50}$ but sites with γ subunits having $K_D > EC_{50}$, consistent with results using photolabeling with azipropofol and a click agent in neurons. Correlating these results with observations of interactions from Equilibrium MD explained the surprising result that propofol had a particularly low affinity for the site with the most polar residues, due to competition with water.(**?**)

Pitfalls:

- Insufficient sampling to properly calculate the necessary averages is a primary pitfall (**?**); it can be assessed by examining $\Delta\Delta G$ per window by plotting the last column of the '.fepout' output file from the FEP simulation (Figure **??**). Converged windows will flatten out by the end of the window, while abrupt changes indicate a need for:
  - Extending the calculation for that window.
  - Further dividing $\delta\lambda$ into multiple separate windows.

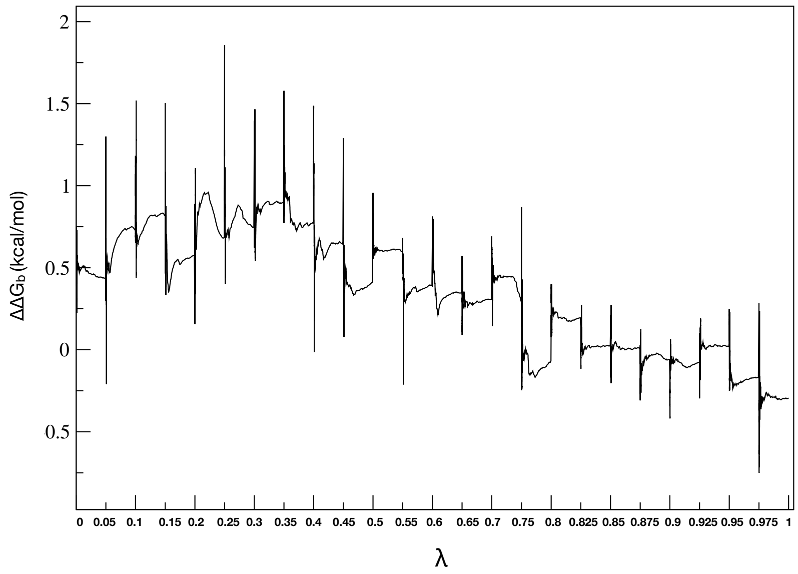

Figure 3.11: $\Delta\Delta G_i$ **variations.** Sample data set for $\Delta\Delta G_i$ variations per window.Curves that plateau (as at $\lambda = 0.825$ to 0.85) indicate convergence, while curves that still change rapidly by the end of the window (as at $\lambda = 0.20$ to 0.25) indicate a need for extending the calculation for that window or dividing the window into two.

  - Removing some of the early values from the average (equivalent to increasing alchEquilSteps)

- Insufficient total simulation time to sufficiently equilibrate decoupled states. One way to assess this is tracking the rehydration of the binding site following the decoupling of the ligand, by comparing the number of solvent molecules with a hydrated site in an apo simulation. Increasing the overall simulation time is necessary if the site does not become fully solvated, and usually adding this time to later, mostly decoupled windows works best.

- Neglecting the analytical correction for the standard state in Equation **??**.

- Applying restraints with inaccurate values for R or $\vec{r}_0$. Analyzing unbiased MD simulations of the protein-ligand complex for each potential site is critical for doing this properly.

- Beginning AFEP using a configuration generated by docking without performing sufficient equilibration. In the case of Sevoflurane docked to a lower site in the TMD (Figure **??** A), FEP run resulted in an affinity in the 0.1 M range, while AFEP runs with well equilibrated conformations (Figure **??** B) yielded affinities in the 20-200mM range, on the order of EC_{50}.

3.6 Summary

We have presented a step-by-step approach to identifying candidate binding sites and quantifying and ranking affinities of volatile and injected general anesthetics with pentameric ligand-gated ion channels. While automated docking calculations do have limited usefulness, the realistic parameterization and explicit water and lipids used in Molecular Dynamics simulation is particularly important for characterizing interactions of GAs with binding sites in pLGICs. For identifying multiple candidate sites, flooding simulations provide a useful balance between classical simulation that is straightforward to interpret and conceptualize in analogy with experiments, while still maintaining a realistic environment and set of interactions. Alchemical free energy perturbation calculations can provide high accuracy estimates for affinities if carried out carefully, but require skill and careful attention to convergence.

Chapter 4

Relative affinities of general anesthetics for pseudo-symmetric intersubunit binding sites of heteromeric GABA(A) receptors

4.1 Abstract

GABA(A), a pentameric ligand gated ion channel is critical for regulating neuronal excitability. These inhibitory receptors, gated by γ-amino butyric acid (GABA), can be potentiated and also directly activated by intravenous and inhalational anesthetics. Although this receptor is a widely-studied target for general anesthetics, the mechanism of receptor modulation remains unclear. These receptors are predominantly found in 2α: 2β:1γ stoichiometry, with four unique inter-subunit interfaces. Here we use thermodynamically rigorous free energy perturbation (AFEP) techniques and Molecular Dynamics simulations to rank the different intersubunit sites by affinity. AFEP calculations predicted selective propofol binding to interfacial sites, with higher affinities for α_β - β_α and β_γ - α_β, γ - β_γ, and is equivalent to propofol EC50. Propofol is predicted to have 10-fold lower affinity at the other identical site, β_α - α_γ.The simulations revealed the key interactions leading to propofol selective binding within GABAA receptor subunit interfaces, with stable hydrogen bonds observed between propofol and β subunit at α_β - β_α and γ - β_γ sites. Varying number of water molecules flooding the site along with multiple hydrogen bonding partners, causes some differences in affinities among the two identical sites, β_α - α_γ and , β_γ - α_β. Propofol competed with water and lipid molecules for hydrogen bonding in the more amphiphilic and

less tight binding site, α_β- γ due to the lack of bulky residues at 15'M3-α and 15'M1-γ thus resulting in a lower affinity.

Weaker affinities were measured for sevoflurane, consistent with its greater EC50. 'Flooding' molecular dynamics simulations identified stable binding modes in the accessible γ - β_γ, α_β - β_α and β_α - $\alpha_\gamma$sites. Consistent with recent photo-labelling studies, simulations reveal that sevoflurane is highly mobile in the site, interacting with multiple hydrogen bonding partners, and the flooding simulation also reveals a site with multiple occupancy.

4.2 Introduction

General Anesthetics are small molecules that induce immobilization, unconsciousness and amnesia by depressing neuronal signaling (**?**). During general anesthesia, myriad of events alter cognition , sensation and causes unconsciousness. This complicated process has made it difficult to reach consensus on defining what an anesthetized state is. Anesthetics, initially thought to bind only to the lipid membrane (Meyer 1899, Overton 1901), later, based on x-ray and neutron diffraction studies, were also found to bind to proteins (**?**). Multiple studies have shown that anesthetics have multiple sites of action in the ion channel and its mechanism depends on the cell type of the target and the concentration applied to the target (**???**). Following this , experimental approaches were used to identify molecular targets for anesthetics at ligand-gated ion channels, especially, GABA$_\mathrm{A}$R, major inhibitory anion channel, was considered as one of the important targets (**??**).

The γ-amino butyric acid type A (GABA$_\mathrm{A}$R) receptor is an ionotropic receptor critical for inhibitory signaling in the central nervous system. GABA$_\mathrm{A}$Rs exists as heteropentamers, predominantly in the 2α:2β:1γ stoichiometry (**???**). Each subunit consists of 4 helices (M1-M4) in the transmembrane domain, with M2 lining the pore and M4 facing the lipid membrane. Numerous molecules with sedative, anxiolytic, and anesthetic properties are positive modulators or agonists of the GABAA receptor, including neurosteroids (**?**), benzodiazepines (**??**) and inhalational anesthetics such as sevoflurane (**???**) and intravenous general anesthetics (**??**)like propofol (**?**).

Propofol has been a predominantly used general anesthetic since its discovery in 1980. Propofol has been shown to potentiate GABA$_A$R (**?**) and even directly activate the channel at higher concentrations (**??**). With the lack of anesthetic bound crystal structure of GABA$_A$R, identifying binding sites has been mainly through indirect means of mutagenesis and photolabelling. While certain studies have suggested sites involving α or γ subunit, extensive site-directed mutagenesis and photo-labelling indicates a compulsory presence of β subunits in the binding sites (**??????**). With the surge of efficient photo-analogs developed in the recent times for multiple anesthetics that target GABA$_A$R, studies have been able to find relative affinities for specific binding sites (**?**). This study further indicates the presence of atleast 4 distinct binding sites (β_+ -α_-; α_+/γ_+ - β_-) for propofol with varying affinities.

Among the inhaled anesthetics, isoflurane was the first anesthetic shown to enhance GABA induced currents(**?**), following which most volatile anesthetics have been shown to positively modulate GABA$_A$R at a concentration($\approx 300\mu$M) much lower than that of intravenous anesthetics(**?**). Mutagenesis and electrophysiology studies have identified α subunit to be more significant for potentiation by sevoflurane than β subunit(**?**). Mutagenesis studies usually suffers the disadvantage of misinterpreting the results from allosteric conformational change and developing a photoaffinity analogue closely resembling the parent compound has been very challenging. Computational approaches can complement the experimental data, and can be useful in analyzing protein-ligand interactions. Although docking has been used to approximate the location of the binding site, the docking algorithm does not account for desolvation, rotational and translational entropy of the bound

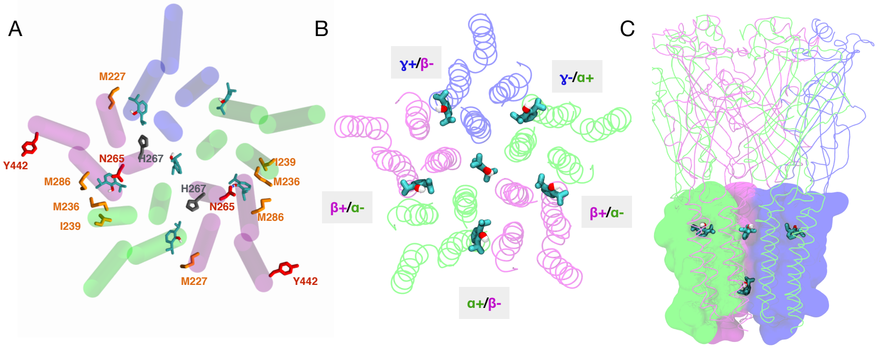

Figure 4.1: **View of the TMD of GABA$_A$R from the ECD** GABA$_A$R is colored by subunit (A) Propofol binding site residues identified through photolabelling using AziPM are shown in orange; o-PD are shown in Gray and residues identified through mutagenesis are shown in red; (B) View of the TMD of GABA$_A$R from the ECD; Starting conformation of propofol in the intersubunit sites are shown in licorice form; (C) Cross-section view of the channel showing the starting conformation of PFL bound to TMD of GABA$_A$R.

ligand and the protein dynamics(**?**). In contrast, MD simulations involve simulating the anesthetic-bound receptor along with the lipid membrane and explicit water, allowing the ligand to explore the binding site. A recent study involved using a novel photoaffinity analog of Propofol, showed selectivity to sites, β_+ -α_- or α_+ - β_- and this was further substantiated using MD simulations to identify key interactions mediating the binding of the ligand and obtain KD values explaining the affinity differences between α/β sites and sites involving γ subunits.

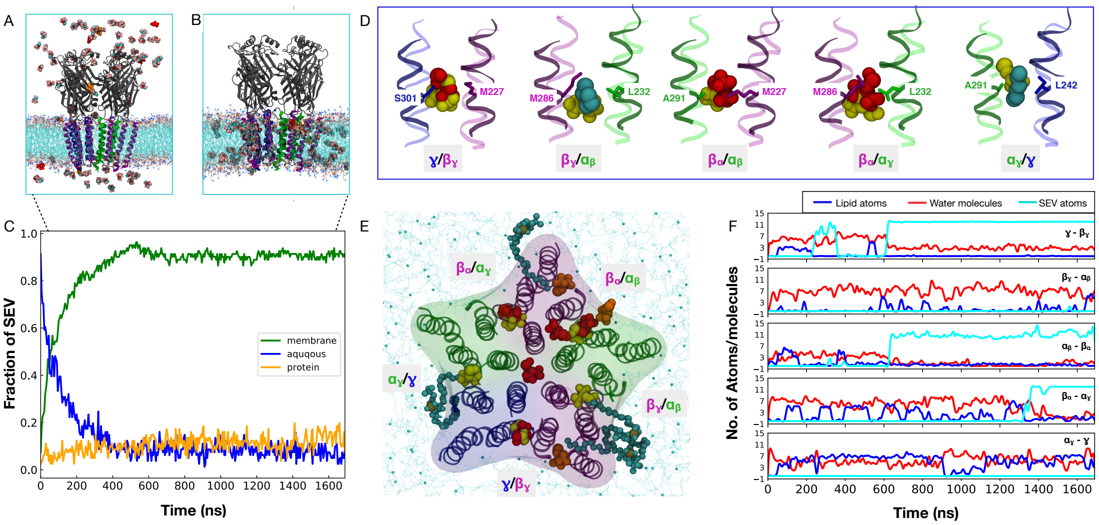

Figure 4.2: **Flooding simulation of GABA$_A$R with sevoflurane.** (A) GABA$_A$R system flooded with sevoflurane in the water box. (B) GABA$_A$R system after the sevoflurane partitions into the lipid membrane;(C) fraction of sevoflurane molecules in each phase; (D) Different intersubunit sites viewed from the TMD, depicting the binding sites and orientation of sevoflurane identified through flooding simulation(red) and standard MD simulation(yellow);(E) View of the TMD of GABA$_A$R from the ECD at the final frame of the flooding simulation, displaying the sevoflurane molecules bound to the TMD of the channel; (Red) VDW representations are Sevoflurane molecules that are bound to the inter-subunit sites; (yellow) are molecules that are bound to the β intra-subunit sites; (orange) are molecules are that are found in the periphery of the TMD and the pore; (cyan) VDW representation of lipid molecules that penetrate β intra-subunit sites and one of the inter subunit site (α_+ - β_-); (F) Number of water(red) molecules, lipid(blue) and Sevoflurane(cyan) atoms that enter intersubunit cavity in the course of the simulation.

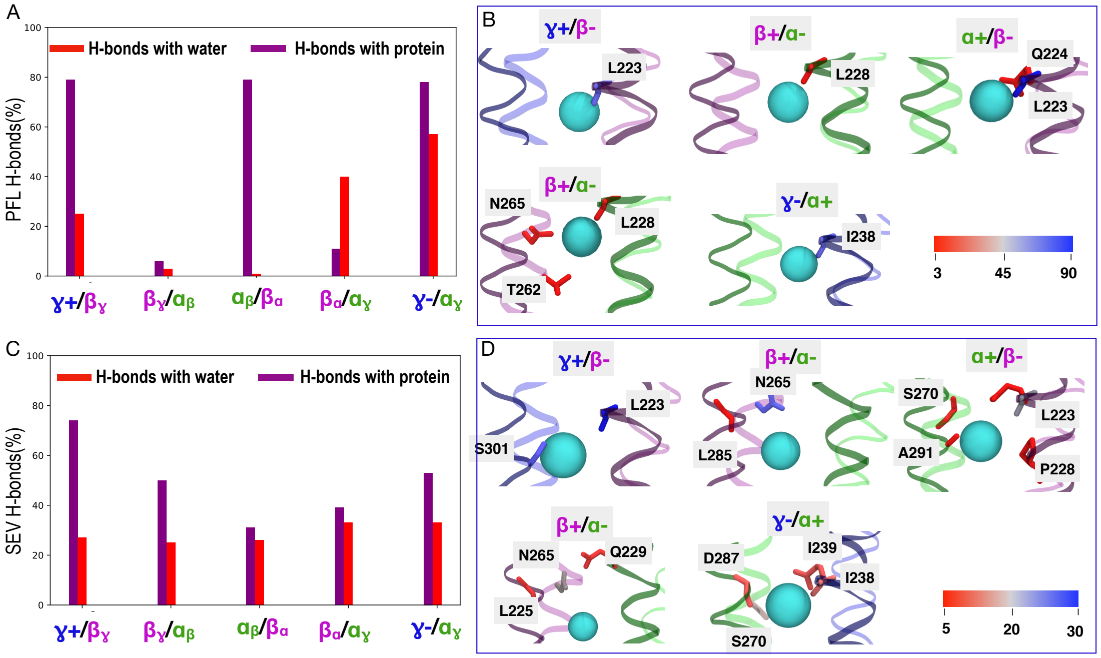

Figure 4.3: **Protein-anesthetic interactions in intersubunit sites.** (A) Percentage of H-bonds between protein or water and (A) Propofol and (C) Sevoflurane. The protein residues that H-bond with PFL(B) and SEV(D) are shown in licorice and colored by the percentage of the hydrogen bonds formed in the course of the simulations, with red denoting residues that forms least number of Hydrogen bonds with the ligand and blue denoting the residues forming the highest number of hydrogen bonds.

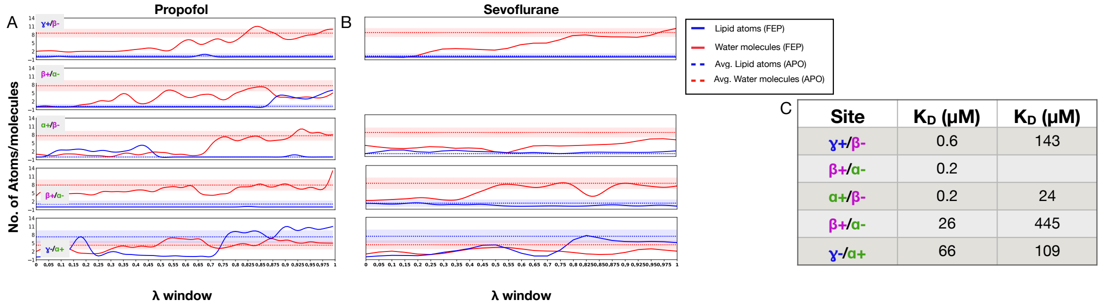

Site	K_D (μM)	K_D (μM)
γ+/β-	0.6	143
β+/α-	0.2	
α+/β-	0.2	24
β+/α-	26	445
γ-/α+	66	109

Figure 4.4: **Free energy of binding for Propofol and sevoflurane.** Free energy calculation for propofol bound to GABA$_A$R (A) Plot depicting the number of water(red) molecules and the lipid(blue) atoms that enter the binding site through the course of the FEP simulation of Propofol and (B) Sevoflurane.(C) Dissociation constant (K_D) values of Propofol and Sevoflurane at different intersubunit sites.

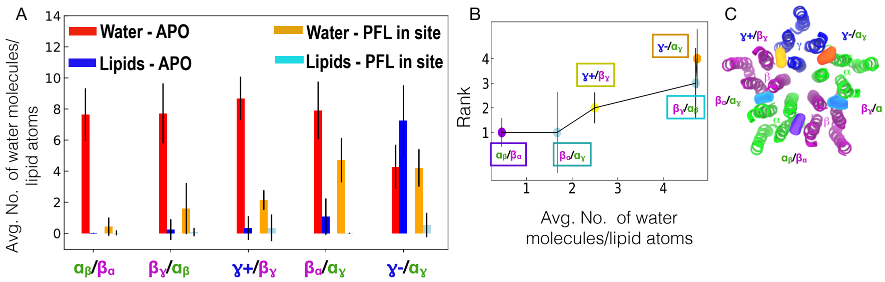

Figure 4.5: **Water, lipid interactions at intersubunit sites.** (A)Comparisons of the Number of water molecules and Lipid atoms at the different intersubunit site in Apo receptor system and propofol bound receptor system; (B) Correlation between binding site affinity and average no. of water or lipid atoms in the specific sites in propofol bound receptor system.(C) A, five propofol molecules (colored surfaces) docked in the GABA$_A$R receptor subunit interfaces (β_α - α_γ and β_γ - α_β (2 sites)) are as follows: cyan, α_β - β_α; violet, α_γ - γ; orange, γ - β_γ; yellow.

4.3 Results

Persistent interactions observed between anesthetics and residues from photolabeling

Photolabeling experiments have developed multiple photo-analogs for many general anesthetics, in particular, $\mathrm{GABA_A R}$ receptor in this study, was modelled based on the GluCl crystal structure(4RHW) with the ivermectin bound, a positive modulator to the M2-15' in the channel (**?**). This confirms the presence of 5 distinct binding clefts at inter-subunit sites in the TMD region. Furthermore, multiple residues have been photolabelled in this region with photo analogs of etomidate, barbiturate , propofol etc. The $\mathrm{GABA_A R}$ receptor homolog model is arranged clockwise with two $\alpha 1$, two $\beta 3$, and one $\gamma 2$ subunit arranged $\beta\alpha\beta\alpha\gamma$ counterclockwise. This creates 5 intersubunit sites, β_γ - α_β, α_β - β_α, β_α - α_γ, α_γ - γ, γ - β_γ (Figure **??** B). Site α_β - β_α has residues identified as being part of the binding site through various experimental techniques. One of the residues identified through experimental studies, in this site is the (15'M1)βM227. Propofol inhibitable photolabelling of the residue βM227 with AziPm was evident in $\alpha 1\beta 3$ receptors(**?**). MD simulations also revealed the residue βH267, that was photolabelled using propofol analog o-PD (**?**), occasionally facing the propofol in this site (**??** C). Sites β_γ - α_β and β_α - α_γ are two identical interfaces among the five intersubunit sites. Most of the residues identified experimentally are found in this interface. The 15'M2 βN265, a residue that has seldom been photolabelled, has been shown to weaken propofol effects, when mutated to methionine(**?**)(**?**) and is seen to form hydrogen bond with propofol during our MD run. Remaining but reduced propofol effects despite the N265M mutation, further indicates presence of other binding sites for propofoll(**?**). The residues M3 βM286 and M1αM236 identified through photolabelling(**?**), forms the lipid facing residues, while also being in close proximity to the bound Propofol in our simulations. Various mutations to the residue M286 has revealed that when mutated to β_2-M286W, this reduces the binding site volume and thus does not allow potentiation of $\mathrm{GABA_AR}$ by propofol((**?**)). Mutation and SCAMP studies further provide definite evidence of the presence of αM236 in this binding site (**?**). In accordance with these results, through the course of the MD simulations, we see that propofol slides between two regions in the site, one being near β M286-N265 region and other being near α-M236. This behavior is evident in both the β_γ - α_β , β_α - α_γ sites. Although a recent experimental study has indicated that the two identical sites differentially affect modulation by etomidate and not propofol (**?**), the affinity of propofol, calculated for the two sites, in this study, are certainly different. This behavior in addition to the difference in number of water flooding these sites could explain the dissimilarity in the behavior of propofol in this site (Figure **??** B,D).

A recent work of involving photolabelling protection experiments (ABPP) of propofol along with our simulations, revealed the high affinity sites as the ones involving α and β subunits(**?**). Despite the comparatively polar interface of γ - β_γ, this site has the same β_- side as the highest affinity site α_β - β_α, with the propofol consistently hydrogen bonding with βL223. But the weak hydrogen bonding and low affinity reported in the previous study(**?**) could stem from the fact the bound propofol in the site did not have a low energy conformation (**?**). With low energy propofol configuration, our current FEP calculation, suggests that the γ - β_γ has an affinity for propofol that is equivalent to the highest affinity site.Although no residues on γ has been reported to be present in the binding site, the residue βM227 is part of this interface as well (Figure **??** A).

α_γ - γ is the only site that does not have any propofol binding site residues identified experimentally. In accordance with this, our FEP simulations also identifies this site to have a comparatively lower affinity. MD simulations further reveal an increased amount of lipid interference as compared to other sites. Lack of a bulky Methionine residue at the 4' location, unlike the other sites, could provide more room for lipid penetration (Figure **??** E).

Flooding with sevoflurane suggests multiple occupancy for some sites, as well as exchange with lipid.

As shown in Figure **??**(E), we observe sevoflurane flooded in the system to occupy three of the five intersubunit sites, γ - β_γ, α_β - β_α, β_α - α_γ. Specifically in site, α_β - β_α, we see two sevoflurane bind the site (**??**(E)), with one of the sevoflurane molecule, entering from the pore, while the other entering from the lipid membrane. Sevoflurane being a small-molecule anesthetic, with higher solubility in water is well suited for a flooding simulation. In $\approx$ 300 ns we see that almost all of the sevoflurane molecules partition into the lipid membrane, leaving the aqueous environment as shown in Figure (**??** A,B, C) . Following this we observed sevoflurane to bind inter-, intra-subunit and pore sites (Figure **??** E). All the intersubunit sites identified were in the upper TMD , closer to ECD, similar to sites identified through standard MD simulations . The different inter-subunit sites were occupied by water , lipids or sevoflurane molecules as described in the Figure (**??** F). As evident in Figure (**??** F) , sevoflurane temporarily occupies γ - β_γ at $\approx$ 200ns , for $\approx$150ns before re-entering the site at $\approx$ 600ns. We see α_β - β_α site gets occupied at $\approx$ 600ns as well. While the γ - β_γ site appears to have about 5-8 molecules of water until occupied by sevoflurane , the α_β - β_α has only about 2-5 molecules of water indicating the more hydrophobic nature of the site. Subsequently, another sevoflurane molecule enters the α_β - β_α site at $\approx 1\mu$s thus revealing a possibility of multiple occupancy at this site. The β_α - α_γ was the last to get filled in the course of the simulation at $\approx 1.3\mu$s. Sites β_γ - α_β and α_γ - γ remained unoccupied in the course of 2μs simulation and is instead occupied by lipids and water molecules thus prohibiting sevoflurane from binding(Figure **??** E,F) . All the Sevoflurane molecules bind the inter-subunit sites by entering the lipid membrane except the site α_+ - β_- in proximity to the pore, which is bound by a sevoflurane initially present in the pore. This pathway gives us a clear indication of how a ligand entering the pore could end up occupying an inter-subunit site, instead of blocking the pore (**?**).

Spontaneous binding is observed for intrasubunit, pore, sites from flooding.

As shown in Figure (**??** E) β subunit is the only subunit that favored intra-subunit sevoflurane binding , at a height similar to that of the inter-subunit sites. While the site between the M1 and M4 helix is occupied by sevoflurane, a lipid tail is seen to penetrate the subunit between the M3 and M4 helix. This interactions occur at identical spots in both the β subunits. We see three Sevoflurane molecules enter the pore one after the other through the ECD. While two sevoflurane molecules remain very mobile within the upper-TMD of the channel, a third Sevoflurane entering the site leads to it being forced to enter a intersubunit site. In the course of the simulation, one of the sevoflurane molecule enters the inter-subunit site α_+ - β_- site from the pore thus revealing another binding site at this cavity.

Propofol but not sevoflurane persistently hydrogen-bonds with backbone.

As shown in Figure **??** (A,B) , Propofol forms Hydrogen bonds with the backbone carbonyl oxygen in each of the interface, more persistently ($\approx$80-90%) in sites with Propofol facing $\beta_-$and γ subunit than α_-. In comparison, Sevoflurane, a less potent anesthetic, forms hydrogen bonds transiently ($\approx$30%) than propofol, with having strongest interaction at γ - β_γ β_γ - α_β (Figure **??** (C,D) . Due to the presence of a conserved proline residue at the 13‘ position on all M1 transmembrane helix, a break in the helix is formed at 16‘ position, thus causing the carbonyl oxygen to be available for hydrogen-bonding with the ligand. This behavior is also observed in crystal structures of GluCL and GABA β_3 homopentamer.

As illustrated in Figure **??** (B) at the interfaces, γ - β_γ, α_β - β_α and α_γ - γ, the propofol interacts solely with the backbone carbonyl oxygen of βL223, γI238 respectively. In the two identical β_α - α_γ and β_γ - α_β sites, propofol behaves differently, with forming highly transient hydrogen bonds with αL228 in β_γ - α_β and weak hydrogen bonds with multiple residue such as ,βN265, βN262, and αL228 in β_α - α_γ.

Figure **??**(D), sevoflurane forms most consistent hydrogen bond at the γ - β_γ site, with residues βL223 and γ301.At the α_γ - γ, sevoflurane shows strong interaction with αS270 and weak interactions with the *gamma* interface, Q238, I239. In the β_γ - α_β site, sevoflurane interacts with the residue homologous to αS270, βN265, more consistently than β_α - α_γ. Sevoflurane form weakest interactions at the α_β - β_α site with the βL223. The general presence of multiple hydrogen-bonding partners makes the Sevoflurane very mobile in the site.

Propofol but not sevoflurane shows site specificity.

We identified β_+ -α_- and α_+ - β_- to have the highest affinity followed by γ_- - β_+ and α_+ - γ_- as tabulated in Figure (**??**). The number of water/lipid molecules that bind the site after the unbinding of Propofol reaching the average number of water/lipid occupying the site, indicates the convergence of the free energy calculation (Figure (**??** A, B , C)). The two identical β_+ -α_- having weak and multiple hydrogen-bonding residues , in addition to different number of water molecules could lead to propofol behaving differently in the sites.

Differences in affinities across sites for Propofol tend to reflect distinct interactions of the sites with lipid or water rather than anesthetics.

Figure **??** (A) helps us understand how these inter-subunit sites differ based on the number of water/lipid atoms occupying the sites. In the apo receptor, the

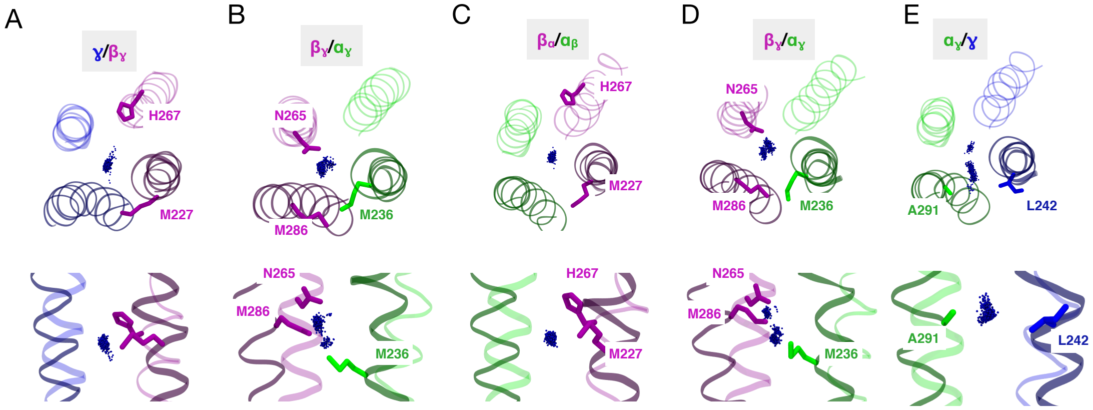

Figure 4.6: **Trajectory of propofol at subunit interface.** Individual subunit interface, with view from ECD(top) and view along TMD(below); Licorice residues colored by subunit are the residues identified through previous experimental studies; Blue dots represent the center of mass of propofol throughout the simulation(A) γ - β_γ,(B) β_γ - α_β,(C) α_β - β_α, (D) β_α - α_γ, (E) α_γ - γ; (E) No residues have been reported in this site; Residues in licorice form are residues homologous to other sites.

sites containing α and β subunits have similar number of water molecules. γ - β_γ site has slightly more number of water molecules compared to the other sites due to the additional polar residue in site as shown in our previous study (**?**). Simulations reveal some water molecules being replaced due lipid binding in site α_γ - γ. In order for an Anesthetic to bind the intersubunit sites, it would have to replace the water/lipid residues in site. Therefore the affinity of particular site would depend on the number of water/lipid residues removed or existing in that site following the binding of propofol. Figure **??** (B), shows the correlation between the affinity and the number of water/lipid atoms existing in site. We see the affinity increases with ability of propofol being able replace all the water molecules in site.

4.4 Conclusion

Propofol bound to the different intersubunit sites show persistent interactions with the backbone carbonyl oxygen on M1 helix in interface containing β_{-}or γ_{-} subunit. Despite Propofol showing very transient hydrogen bonding at the β_γ - α_β interface, this site has a higher affinity due to ability of propofol to displace water/lipid molecules originally occupying the site in Apo receptor. In a similar trend sites, Propofol shows a higher affinity for sites α_β - β_α, γ - β_γ and β_γ - α_β. With comparatively higher amount of water/lipid molecules in the presence propofol makes these sites have weaker affinity for propofol. For sevoflurane, flooding simulations reveal various inter and intra-subunit sites. Sevoflurane was observed to bind both the β intrasubunit , γ - β_γ, β_α - α_γ and α_β - β_α intersubunit sites, with multiple occupancy in α_β - β_α site. FEP simulations showed that sevoflurane showed no specificity to any particular site with affinity values for all sites below its EC_{50}

.1 Appendix A: Role of the Fourth Transmembrane a Helix in the Allosteric Modulation of Pentameric Ligand-Gated Ion Channels

This chapter involves experimental work conducted by experimentalists in University of Ottawa. The results were validated by us using computational techniques and analysis were performed using tcl and python scripts.

Article

Structure

Role of the Fourth Transmembrane α Helix in the Allosteric Modulation of Pentameric Ligand-Gated Ion Channels

Graphical Abstract

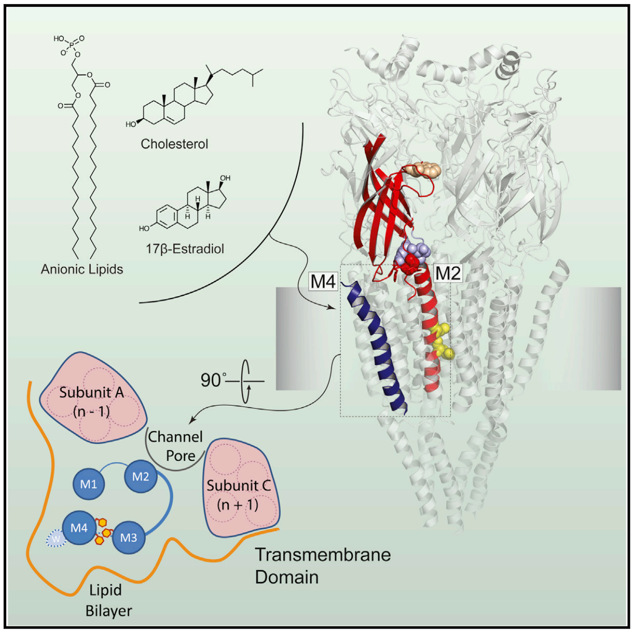
Cholesterol
17β-Estradiol
Anionic Lipids
M4
M2
90°
Subunit A
(n - 1)
Channel
Pore
Subunit C
(n + 1)
M1
M2
M4
M3
Transmembrane
Domain
Lipid
Bilayer

Highlights

- The transmembrane α helix, M4, is the site of action for lipids and neurosteroids
- Enhanced interactions between M4 and adjacent α helices potentiate channel function
- These also underlie potentiation by a lipid-facing myasthenic syndrome mutation
- M4 influences the allosteric modulation of pentameric ligand-gated ion channels

Authors

Casey L. Carswell, Camille M. Hénault, Sruthi Murlidaran, ..., Julian A. Surujballi, Grace Brannigan, John E. Baenziger

Correspondence

john.baenziger@uottawa.ca

In Brief

Numerous modulators of pentameric ligand-gated ion channels act on structures peripheral to those directly implicated in gating. Carswell et al. show how one of these structures, the transmembrane M4 α helix, plays a role in the allosteric regulation of channel function.

Carswell et al., 2015, Structure *23*, 1655–1664
September 1, 2015 ©2015 Elsevier Ltd All rights reserved
http://dx.doi.org/10.1016/j.str.2015.06.020

Structure
Article

Role of the Fourth Transmembrane α Helix in the Allosteric Modulation of Pentameric Ligand-Gated Ion Channels

Casey L. Carswell,[1,4] Camille M. Hénault,[1,4] Sruthi Murlidaran,[2] J.P. Daniel Therien,[1] Peter F. Juranka,[1] Julian A. Surujballi,[1] Grace Brannigan,[2,3] and John E. Baenziger[1,*]
[1]Department of Biochemistry, Microbiology, and Immunology, 451 Smyth Road, Ottawa, ON K1H 8M5, Canada
[2]Center for Computational and Integrative Biology, Rutgers University-Camden, Camden, NJ 08102, USA
[3]Department of Physics, Rutgers University-Camden, Camden, NJ 08103, USA
[4]Co-first author
*Correspondence: john.baenziger@uottawa.ca
http://dx.doi.org/10.1016/j.str.2015.06.020

SUMMARY

The gating of pentameric ligand-gated ion channels is sensitive to a variety of allosteric modulators that act on structures peripheral to those involved in the allosteric pathway leading from the agonist site to the channel gate. One such structure, the lipid-exposed transmembrane α helix, M4, is the target of lipids, neurosteroids, and disease-causing mutations. Here we show that M4 interactions with the adjacent transmembrane α helices, M1 and M3, modulate pLGIC function. Enhanced M4 interactions promote channel function while ineffective interactions reduce channel function. The interface chemistry governs the intrinsic strength of M4-M1/M3 inter-helical interactions, both influencing channel gating and imparting distinct susceptibilities to the potentiating effects of a lipid-facing M4 congenital myasthenic syndrome mutation. Through aromatic substitutions, functional studies, and molecular dynamics simulations, we elucidate a mechanism by which M4 modulates channel function.

INTRODUCTION

Pentameric ligand-gated ion channels (pLGICs), such as the nicotinic acetylcholine receptor (nAChR), respond to neurotransmitter binding by transiently opening either cation- or anion-selective channels across the post-synaptic membrane. The sites for agonist binding are located at the interfaces between subunits in the extracellular domain (ECD), which extends away from the membrane surface into the synaptic cleft (Figure 1) (Unwin, 2005). Agonist binding induces rigid body motions, which are translated into transient movements of the pore lining M2 α helices of the transmembrane domain (TMD) by a series of loops at the ECD/TMD interface (Althoff et al., 2014; Sauguet et al., 2014; Unwin and Fujiyoshi, 2012). Considerable attention has focused on elucidating the gating movements of these interfacial loops, which form the primary allosteric path leading from the agonist site to the channel gate (Grutter et al., 2005; Jha et al., 2007; Lee and Sine, 2005; Lummis et al., 2005). In contrast, structures not directly involved in the primary allosteric path have received less attention, even though a number of allosteric modulators influence gating via these auxiliary sites (Figure 1A).

The fourth transmembrane α helix, M4, is located on the periphery of the TMD and is the target of both lipids and neurosteroids (Baenziger et al., 2015; Barrantes, 2003, 2015; Henault et al., 2015; Hosie et al., 2006; Paradiso et al., 2001). Lipid-facing mutations in M4 of the muscle-type nAChR influence channel gating, with at least one leading to a congenital myasthenic syndrome (CMS) (Bouzat et al., 1998; Lasalde et al., 1996; Lee et al., 1994; Li et al., 1992; Shen et al., 2006; Tamamizu et al., 2000). M4 extends beyond the bilayer to interact directly with the β6-β7 loop (often referred to as the Cys-loop), a key structure at the ECD/TMD interface that participates in channel gating. One model proposes that interactions between M4 and the adjacent α helices, M1 and M3, are dynamic, in that effective M4-M1/M3 interactions lead to M4/Cys-loop contacts that promote channel function, while ineffective M4-M1/M3 interactions abolish M4/Cys-loop connections to reduce channel function (daCosta and Baenziger, 2009; daCosta et al., 2013). In this context, it is intriguing to note that of the four transmembrane α helices, M1–M4, M4 exhibits the greatest sequence variability among the various *Torpedo* and human nAChR subunits. This variability should lead to subunit-specific interactions at the interface between M4 and M1/M3, resulting in variable interaction energies. If strong M4-M1/M3 interactions promote coupling between the agonist site and channel gate, then variable M4-M1/M3 interaction energies should lead to variable coupling efficiencies. nAChR subunits with weak M4-M1/M3 interactions should also be more sensitive to allosteric modulators that act on M4.

The two structurally well-characterized prokaryotic pLGICs, GLIC and ELIC (Figure 1) (Bocquet et al., 2009; Hilf and Dutzler, 2008, 2009; Pan et al., 2012; Sauguet et al., 2013), are excellent models for probing the role of M4 in pLGIC function, as both share a similar tertiary/quaternary fold yet have distinct M4 conformations. In GLIC, M4 interacts tightly with M1/M3 along its entire length. In ELIC, the C-terminal half of M4 tilts away from M1/M3 with the final five residues unresolved in the crystal structure. Aromatic interactions are key determinants that

©2015 Elsevier Ltd All rights reserved

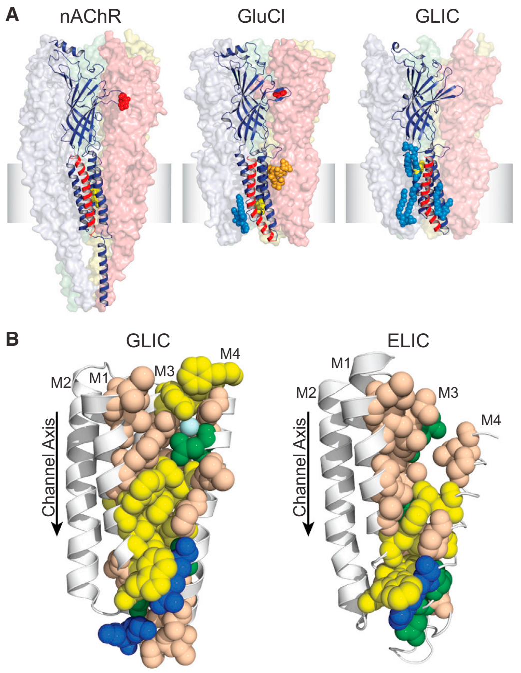

Figure 1. Structures of pLGICs with Bound Modulators

(A) Structures of the nAChR (PDB: 2BG9), GluCl (PDB: 3RIF), and GLIC (PDB: 3P50). In each case, a single subunit is shown as a dark-blue cartoon with the M4 α helix highlighted in red. In the nAChR (left), residues in the agonist site are highlighted as red spheres, while those forming the transmembrane gate are highlighted as yellow spheres. In GluCl (center), the agonist glutamine, the positive modulator ivermectin, the open channel blocker picrotoxin (aligned using 3RI5), and a bound detergent molecule are highlighted as red, orange, yellow, and marine spheres, respectively. In GLIC (right), the inhibitor propofol and bound lipids (aligned from 3EAM) are shown as yellow and marine spheres, respectively.

(B) A single TMD subunit of ELIC (left, 2VL0) and GLIC (right, PDB: 4HFI) with residues at the M4-M1/M3 interface shown as spheres. Aromatic, polar hydrogen bonding, positive, and aliphatic residues are highlighted in yellow, green, blue, and tan, respectively. The marine sphere corresponds to a water molecule.

energetically drive the binding of M4 to M1/M3 during folding of the homologous glycine receptor (Haeger et al., 2010). GLIC exhibits an extensive network of interacting aromatic residues at the M4-M1/M3 interface, including a cluster of three aromatic residues that may be essential for linking the C terminus of M4 to both M1/M3 and the β6-β7 loop (see Figures 1B and 3). Intriguingly, this C-terminal M4 aromatic cluster is absent in ELIC. Through aromatic substitutions, functional studies, and molecular dynamics simulations, we examine here the effects of aromatic residues at the M4-M1/M3 interface on the conformation of M4, and how the resulting changes in conformation influence channel function. We also examine whether TMD modulators influence pLGIC function by modulating M4-M1/M3 interactions.

RESULTS

Aromatic Residues Promote M4-M1/M3 Interactions

GLIC exhibits nine aromatic residues at the M4-M1/M3 interface (Figure 1B), labeled as aromatics (1) M4 F315, (2) M4 F314, (3) M3 Y254, (4) M4 F303, (5) M3 F265, (6) M3 Y266, (7) M1 W213, (8) M4 F299, and (9) M1 F216 (see Figure 3). Although the aromatics at positions 4, 7, 8, and 9 are conserved in ELIC, the entire M4 C-terminal aromatic cluster (aromatics 1–3) and the aromatic side chains at positions 5 and 6 on M3 are absent. We postulated that the distinct profiles of aromatic interactions at the M4-M1/M3 interface in GLIC and ELIC lead to the different conformations of M4 observed in the crystal structures. The different M4 conformations, however, could also result from differential crystal packing and/or detergent-solubilization effects prior to crystallization (daCosta and Baenziger, 2013).

To probe whether aromatic substitutions at the M4-M1/M3 interfaces influence the conformation of M4 in a folded pLGIC structure located within a membrane environment, we turned to molecular dynamics simulations. Simulations were run for both wild-type GLIC (WT-GLIC) and a mutant where the five non-conserved aromatic residues were mutated to Ala (5Ala-GLIC: aromatic-to-Ala substitutions at positions 1, 2, 3, 5, and 6). In both cases, simulations were performed using intact pentamers, as well as with a single-subunit-TMD. Both sets were run in palmitoyl-oleoyl-phosphatidylcholine (POPC) bilayers, a membrane that supports GLIC function (Labriola et al., 2013). The latter simulations revealed intriguing lipid binding poses, which are discussed below. Finally, simulations run for both wild-type ELIC and an ELIC mutant with aliphatic-to-aromatic substitutions at the same positions in the M4-M1/M3 interface were not informative because affected residues in the M4 C terminus are not defined in the ELIC crystal structure, thus precluding a defined starting conformation.

Consistent with our hypothesis, the simulations show that aromatic residues at the M4-M1/M3 interface influence the interactions of M4 with M1/M3. Specifically, the close contacts between residues along the entire length of M4 and those on M1/M3 in the GLIC crystal structure are maintained throughout the simulations with WT-GLIC. In contrast, the loss of the C-terminal aromatic cluster leads to a consistent tilting of the C-terminal half of M4 away from M1/M3, with closest C_α-C_α carbon atom contacts on M4-M1 and M4-M3 increasing by roughly 2 Å (Figures 2A and S1: the latter compares directly distances between Y/A254 on M3 and both F/A314 and F/A317 on M4). The differences in M4-M1/M3 interactions are statistically significant based on SEs calculated across the five subunits. The magnitudes of the separations are larger than typical root-mean-squared-deviations among the transmembrane C_α atoms of different pLGICs (Bocquet et al., 2009; Hibbs and Gouaux, 2011; Hilf and Dutzler, 2009; Miller and Aricescu, 2014) or between different conformations of GLIC (Sauguet et al., 2013). The C_α carbon atom separations observed in the M4 C-terminal region contrast with those observed between M4 and M1/M3 near the cytoplasmic side of the bilayer, where the C_α carbon atom separations in 5Ala-GLIC and WT-GLIC converge (C_α atoms separation differences are less than 1 Å) (Figures 2A–2C). The latter suggests that the aromatic interactions remaining

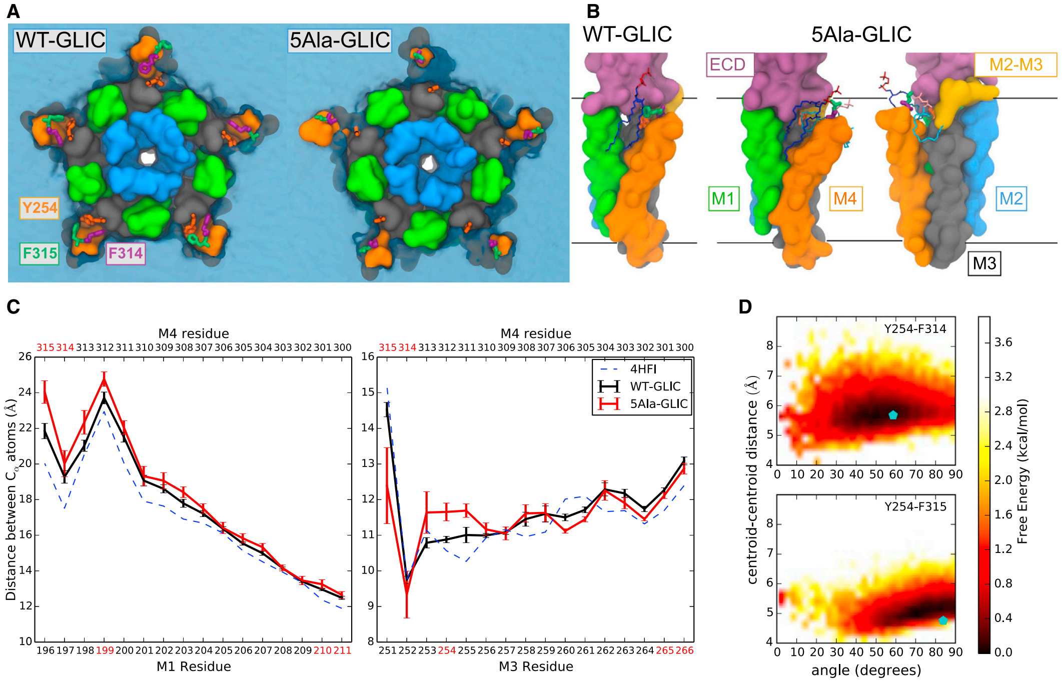

Figure 2. Aromatic Residues Promote M4-M1/M3 Interactions

(A) Transmembrane domain of WT-GLIC and 5Ala-GLIC following 300 ns of simulation. Helices are shown in surface representation (M1, green; M2, blue; M3, dark gray; M4, orange), with substituted residues shown in stick representation (Y/A254, orange; F/A314, purple; F/A315, green). The M2-M3 loop (yellow) and a portion of the ECD (purple) closest to the interface with the TMD are also shown in surface representation. POPC lipid density, averaged over the final 200 ns of the simulation, is represented by a translucent blue isosurface; the submerged appearance of the 5Ala-GLIC M4 α helices relative to those of WT-GLIC reflects significant lipid penetration of the 5Ala-GLIC subunits.

(B) Representative subunit from WT-GLIC (left) and 5Ala-GLIC (center), showing POPC lipids bound to the M1-M4 interface in stick representation with blue acyl chains and red PC headgroups. A rotated view of 5Ala-GLIC (right) shows a second POPC molecule bound to 5Ala-GLIC, with cyan acyl chains and pink PC headgroups, straddling the 5Ala-GLIC M3-M4 interface. Lines represent the membrane-water interface.

(C) Average distances between C_α atoms on residues at similar register on opposing helices. Substituted residues are highlighted in red. Error bars represent the SE across the five subunits.

(D) Free energy landscape (potential of mean force) for configurations of F314 and F315 relative to Y254 in four of five WT-GLIC subunits, as a function of angle between planar groups and centroid-centroid distance (Equations 1 and 2 in the Supplemental Information). In a fifth subunit, the aromatic cluster disassociates early in the simulation, as discussed further in Figure S2. The blue symbol in each panel indicates the value of the corresponding angle and distance determined from the crystal structure (PDB: 4HFI).

See also Table S1; Figures S1 and S2.

in the intracellular leaflet of 5Ala-GLIC are sufficient to maintain effective M4-M1/M3 interactions in this region.

The tilt of the C-terminal half of M4 observed in the simulations of the 5Ala-GLIC mutant suggests that aromatic residues are essential for promoting effective M4-M1/M3 interactions. Note that the observed tilt of M4 away from M1/M3 in the simulations of 5Ala-GLIC is similar, but of lesser magnitude than the tilt of M4 observed in the crystal structure of ELIC. In the ELIC crystal structure, the terminal five residues are unresolved, suggesting weak, if any, interaction between the M4 C terminus and M1/M3. The ELIC crystal structure supports the conclusion that aromatic residues at the M4-M1/M3 interface promote M4 interactions with M1/M3. Detergent solubilization and the removal of lipids may perturb the intrinsically weak interactions between the M4 C-terminus and M1/M3, leading to a greater disruption of M4 conformation than observed in the simulations.

The aromatic-to-Ala substitutions have a substantial effect on the energetics of M4-M1/M3 interactions. In WT-GLIC, M4 C-terminal aromatics 1, 2, and 3 are involved in pairwise interactions within the aromatic cluster, with Ala substitutions of these residues leading to energetic penalties of >1 kcal/mol (Table S1). For four of the five subunits, the two-dimensional free energy landscape (Figure 2C) calculated from the relative orientations of M3:Y254 (3) and M4:F315 (1) aromatic groups has a strong angular dependence consistent with π-π stacking interactions, with the minima near 90° indicating a T-shaped conformation similar to that found in the crystal structure. In the fifth subunit, F315 dissociates from the cluster and rotates to face the

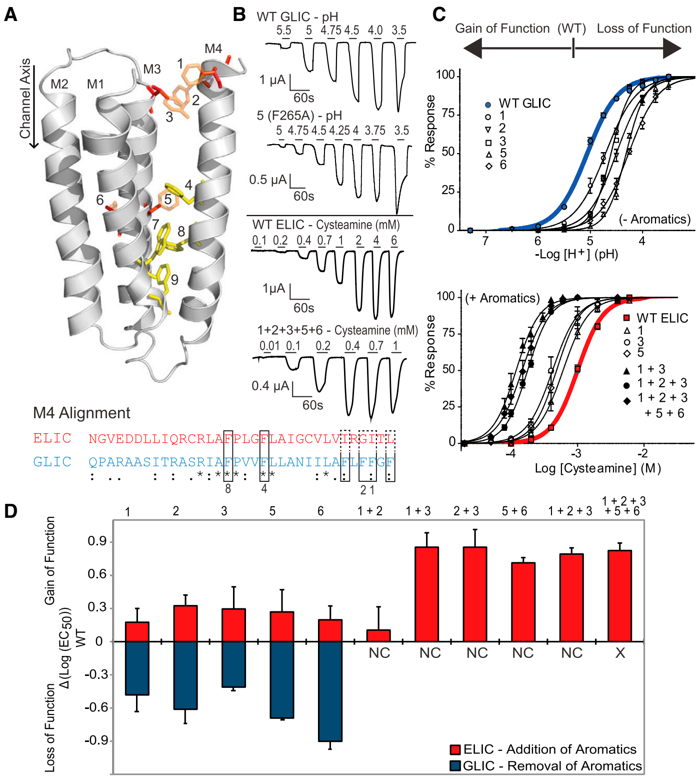

Figure 3. Enhanced M4-M1/M3 Interactions Potentiate pLGIC Function

(A) The TMD of a single subunit of an ELIC homology model (based on GLIC, PDB: 3EHZ). Aromatic residues conserved in GLIC and ELIC are shown in yellow, while aromatics removed from GLIC or inserted into ELIC are shown in orange, superimposed on wild-type (WT) ELIC residues (red). The M4 sequence alignments highlight key aromatic residues (boxed), and identical (*), conserved (:), and semi-conserved (.) residues.

(B) Two-electrode data for GLIC (upper) and ELIC (lower), with representative mutants. Ligand concentration jumps (protons or cysteamine for GLIC and ELIC, respectively) are indicated by the horizontal bar.

(C) Dose-response curves obtained for single aromatic-to-Ala substitutions in GLIC (upper) and from either single and multiple aliphatic-to-aromatic substitutions in ELIC (lower). Error bars represent SE.

(D) Changes in EC_{50} relative to the WT for GLIC (pH 5.03) and ELIC (0.92 mM cys). NC, no current. Multiple aromatic substitutions were not generated for GLIC (X). Error bars represent SD. See Table S2 for EC_{50} values.

See also Table S2 and Figure S3.

lipids, as also observed in the single-subunit-TMD simulations (Figure S1).

M4 C-terminal aromatics 1, 2, and 3 are also involved in pairwise interactions with other residues that strengthen M4-M3 interactions. An additional strong energy penalty is associated with the loss of a hydrogen bond between the tyrosine hydroxyl of M3:Y254 (aromatic 3) and the carbonyl oxygen of M4:N307. These two residues hydrogen bond via a bridging water in four out of five chains of the highest-resolution crystal structure for GLIC (Sauguet et al., 2013). In the simulations, bridging waters are observed transiently, interspersed with direct hydrogen bonding between the two residues. Also, the mutations weakened several pairwise interactions involving aromatic substituents and non-aromatic polar or hydrophobic residues (Table S1).

One intriguing finding of the simulations is that the tilt of the M4 C terminus away from M1/M3 and/or the reduced side-chain volume in 5Ala-GLIC leads to a change in lipid binding. In WT-GLIC, POPC molecules adopt poses at the edge of the M4-M1 and M4-M3 interfaces, as in the GLIC crystal structures. In 5Ala-GLIC, the POPC molecules penetrate deeper into the M1/M3/M4 α-helical bundle, with entire acyl chains becoming embedded at the M1-M4 interface (Figures 2C and 2D). A second POPC assumes a pose in a cavity formed by the C-terminal end of M4, the M2-M3 loop, and the β6-β7 loop (Figure 2D), where one acyl chain fills the increased free volume vacated by M4 F314 and F315 upon mutation of each residue to Ala, while the other acyl chain remains in contact with the bulk membrane (Figure 2D). Such interactions are seen across subunits, with one lipid at least partially buried in each of these sites. Buried lipids could potentially mediate some of the effects of the aromatic substitutions, by direct interactions with the M2-M3 and β6-β7 loop and/or indirectly by stabilizing M4 in a conformation with reduced interactions with the ECD. This possibility underscores the potential significance of even slight conformational changes in M4, particularly if they increase the free volume at the M4-M1/M3 interface above the volume required to accommodate a buried lipid. Note also that in single-subunit-TMD simulations, the absence of steric conflicts with the ECD allows even deeper penetration of the lipid. It appears that even subtle changes in conformation can dramatically alter lipid binding (Figure S3).

Weakened M4-M1/M3 Interactions Inhibit Channel Function

To test experimentally whether M4 conformation influences channel function, non-conserved aromatic residues in GLIC were individually mutated to Ala to weaken M4-M1/M3 interactions, and the effects of the individual substitutions on channel function were assessed using the two-electrode voltage-clamp apparatus. WT-GLIC gates open in response to protons, with a pH value required to elicit half-maximal channel gating of $pH_{50} = 5.03 \pm 0.08$ (n = 38). Each individual aromatic-to-Ala mutation led to a rightward shift in the dose response to protons, with the pH_{50} values decreasing by ~0.4 to ~0.9 pH units: the Y266A mutation at position 6 (Figure 3) gave rise to the largest shift down to a $pH_{50} = 4.12 \pm 0.07$ (n = 8). The shifts in pH_{50}

correspond to 2- to 8-fold increases in the concentrations of protons required for activation (Figure 3; Table S2). Simultaneous aromatic-to-Ala substitutions of interacting aromatic pairs were also generated, but none of the double mutants gave observable proton-activated currents. The absence of current could reflect impaired channel function and/or folding and then trafficking to the cell surface (Haeger et al., 2010).

Note that the pH_{50} values derived from macroscopic currents depend on both the affinity of the agonist for its binding site and the equilibrium constant governing transitions from closed to open states. In addition, desensitization kinetics can influence the measurement of pH_{50} values. Most of the mutations have little effect on the macroscopic desensitization rates (Figure S3). Given that the proton binding sites for activation are mainly distant from the TMD (Duret et al., 2011), the majority of the changes in pH_{50} likely reflect changes to the equilibrium constant governing channel gating; the decreased pH_{50} values thus likely reflect impaired coupling between agonist binding and channel gating. This interpretation, however, is not unequivocal, as a His235 located on the adjacent M2 α helix influences proton activation of GLIC (Rienzo et al., 2014; Wang et al., 2012). In particular, the Y266A could directly influence the pH_{50} for gating via this intramembrane protonation site.

Enhanced M4-M1/M3 Interactions Potentiate Channel Function

In contrast to the mutations in GLIC, individual aliphatic-to-aromatic substitutions introduced at the M4-M1/M3 interface to enhance M4-M1/M3 interactions in ELIC each shifted the dose response to cysteamine leftward, whether or not interacting aromatic partners on the adjacent transmembrane α helices were present (Figure 3; Table S2). Wild-type ELIC required a concentration of cysteamine to elicit half-maximal channel gating of EC_{50} = 0.94 ± 0.16 mM cysteamine (n = 23). Of the individual aliphatic-to-aromatic mutations, G218F (2) led to the largest reduction in EC_{50} = 0.44 ± 0.09 mM cysteamine (n = 13). The changes in EC_{50} values correspond to between 70% and 50% reductions in the concentrations of cysteamine required. Multiple aromatic additions were also introduced, and these led to even further leftward shifts in the EC_{50} values. Engineering either the entire M4 C-terminal aromatic cluster (EC_{50} = 0.18 ± 0.02 mM cysteamine [n = 9]) or the entire aromatic network of GLIC into ELIC (EC_{50} = 0.15 ± 0.04 mM cysteamine [n = 7]) shifted the EC_{50} down to a value approaching 10% of the EC_{50} value of wild-type ELIC. In fact, the largest reductions in EC_{50} were observed with just two interacting aromatic partners engineered into the M4 C-terminal region, one on M3 and the other on M4. Both the I319F/V260Y and G318F/V260Y double mutants gave EC_{50} values of 0.13 mM cysteamine.

The leftward shifts in the dose response observed with aromatic "additions" in ELIC contrast with the rightward shifts observed with aromatic "deletions" in GLIC, with leftward shifts reflecting a gain, as opposed to a loss, of channel function. In contrast to GLIC where the proton-sensitive intramembrane His235 complicates the interpretation of pH_{50} values, the agonist binding site in ELIC is greater than 30 Å distant from even the closest mutations at the M4-M1/M3 interface, suggesting that the mutations do not directly influence the chemistry of the agonist site and, thus, agonist affinity. Furthermore, mutations in M4 of the nAChR have been shown to have no effect on agonist affinity (Bouzat et al., 2000; Mitra et al., 2004; Shen et al., 2006). Although single-channel measurements are required to confirm that the changes in EC_{50} result from direct effects on channel gating, the long distance between M4 and the agonist site suggests that the changes in EC_{50} detected here reflect enhanced channel function; i.e., enhanced coupling between agonist binding and channel gating. The gain-of-function mutations show that residues along the M4-M1/M3 interface in wild-type ELIC are not optimized to promote M4-M1/M3 interactions that support channel function, and that improving the effectiveness of these interactions promotes coupling between the agonist site and channel gate.

We considered the possibility that aromatic additions to the M4-M1/M3 interface promote more effective interactions with bound lipids to enhance function. Interactions between the F315 aromatic residue in GLIC and lipids are observed in both the pentamer and single-subunit-TMD simulations. The lipid-facing F317 and F312 residues were mutated to alanine, leading to gain-of-function and loss-of-function phenotypes, respectively (F317A pH_{50} = 5.41 ± 0.05 [n = 8], F312A pH_{50} = 4.50 ± 0.01 [n = 6]). These results show that it is impossible to predict how interactions between aromatic residues and lipids will influence channel function.

Finally, an important feature of our results is the consistency of the entire dataset. Every aromatic-to-Ala substitution at the M4-M1/M3 interface in GLIC led to reduced channel function while every aliphatic-to-aromatic substitution at the same interface in ELIC led to enhanced channel function. The latter is particularly compelling, given that although optimal aromatic interactions enhance inter-α-helical interactions, the insertion of aromatic side chains at the M4-M1/M3 interface could lead to structural and/or chemical conflicts and, thus, a loss of channel function. The data highlight the ease with which effective interactions between M4 and M1/M3 in ELIC can be formed to enhance channel function. The consistency of the data suggests that the changes in function are not due to localized changes in structure, which would be expected to have random effects. The molecular dynamics simulations support the hypothesis that aromatic residues at the M4-M1/M3 interface enhance M4-M1/M3 interactions. The gains of function observed with aliphatic-to-aromatic residue substitutions in ELIC thus result, at least in part, from enhanced M4 interactions with M1/M3.

A Lipid-Facing CMS Mutation Potentiates Function by Enhancing M4-M1/M3 Interactions

If M4-M1/M3 interactions in ELIC are intrinsically weaker than in GLIC, leading to relatively poor coupling between the agonist site and channel gate, ELIC may exhibit a greater capacity for potentiation by allosteric modulators that enhance M4-M1/M3 interactions. To test this hypothesis, we focused on a CMS mutation that occurs on the lipid-facing surface of αM4 in the human muscle-type nAChR (C418W). C418W potentiates nAChR channel function roughly 25-fold (EC_{50} = 9.11 ± 1.45 μM acetylcholine [n = 31] for wild-type, EC_{50} = 0.34 ± 0.08 μM acetylcholine [n = 11] for C418W) by directly altering M4-lipid interactions, although the mutation must ultimately influence interactions between M4 and the remainder of the TMD (Figure 4; Table S3).

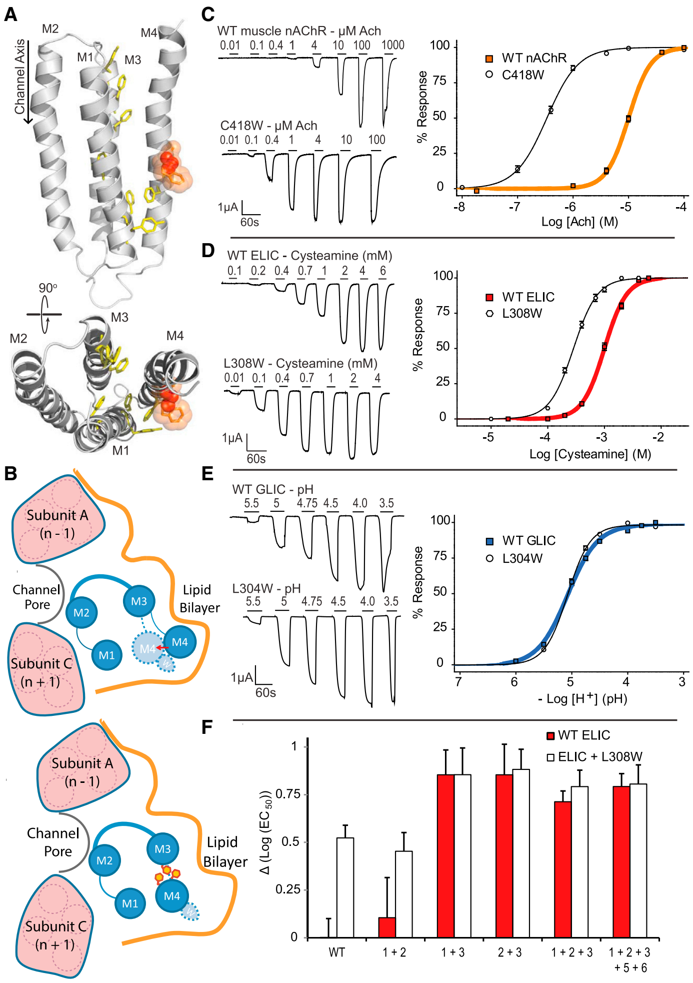

Figure 4. A CMS Trp Mutation Potentiates Channel Function by Enhancing M4-M1/M3 Interactions

(A) Side and top views of the TMD of a single subunit of human α1ChR (homology model based on PDB: 2BG9). Aromatics at the M4-M1/M3 interface are shown in yellow. The lipid-facing residue αC418 is shown as a solid orange sphere, with the potentiating αC418W mutation superimposed as an orange sphere/stick transparent combination.

(B) Proposed mechanism of function for the potentiating effect of αC418W via enhanced M4-M1/M3 interactions. In the absence of M4 C-terminal aromatic contacts, interaction of the bulky αC418W with the lipid bilayer causes M4 to interact more tightly with M1/M3 (red arrow), potentiating activity. In the presence of M4 C-terminal aromatics, M4 already interacts tightly with M1/M3, so αC418W has no effect.

(C–E) Two-electrode data (left) and dose-response curves (right) demonstrating the effect of the αC418 (or equivalent) mutation on (C) human muscle-type nAChR, (D) ELIC (L308W), and (E) GLIC (L304W). Error is represented as SE.

(F) Effect of the L308W mutation on aromatic-substituted ELIC mutants, shown as change in EC_{50} relative to WT ELIC. Error is represented as SD, and mutant numbers correspond to those in Figure 2A. See Table S3 for complete EC_{50} values.

See also Figure S4.

A leucine residue is found in both GLIC and ELIC at the equivalent position. This Leu residue (L304) residue in GLIC was changed to both Cys and Trp, but neither substitution had any effect on channel function (pH_{50} = 5.03 ± 0.02 [n = 6] and pH_{50} = 5.06 ± 0.03 [n = 6]), respectively, possibly because the extensive aromatic network at the M4-M1/M3 interface already promotes effective M4-M1/M3 interactions (Figure 4). In contrast, the same L308C and L308W mutations in ELIC both led to gain-of-function phenotypes, with the magnitude of the L308W gain of function (EC_{50} = 0.29 ± 0.05 mM cysteamine [n = 10]) approaching 5-fold relative to the wild-type ELIC. Significantly, the introduction of interacting aromatic residues to enhance intrinsic M4-M1/M3 interactions reduced the potentiating effects of this CMS mutation in ELIC. In fact, L308W had no further effect on the gating of ELIC mutants containing either the three M4 C-terminal cluster aromatics or all five aromatic substitutions. L308W thus potentiates ELIC function in a manner similar to that observed with the introduction of aromatic residues at the M4-M1/M3 interface. These results show that (1) altered lipid-protein interactions promote channel function by enhancing M4-M1/M3 interactions, and (2) the intrinsic strength of M4-M1/M3 interactions influences the functional sensitivity of a pLGIC to altered protein-lipid interactions, including mutations at the lipid-protein interface. The CMS mutation was also superimposed onto various aromatic-to-Ala substituted GLIC mutants, but none of these gave proton-activated currents (data not shown).

Propofol Inhibits Channel Function via an M4-Independent Mechanism

M4-M1/M3 interactions might play a role in the allosteric effects of other TMD modulators, such as the inhibitory drug propofol. Propofol binds to GLIC near the extracellular surface of the TMD in a cavity delineated by the four transmembrane α helices and capped by the β6-β7 loop, with the most extensive interactions occurring between M1 and M3 (Nury et al., 2011). We tested the possibility that propofol inhibits effective M4-M1/M3 interactions by investigating the effects of propofol on several of the aromatic-substituted mutants of both GLIC and ELIC. None of the aromatic-to-Ala substitutions at the M4-M1/M3 interface of GLIC or the aliphatic-to-aromatic substitutions at the same interface in ELIC, however, had a major effect on propofol inhibition (Figure S4). In contrast to our hypothesis, propofol does not inhibit gating by modulating M4-M1/M3 interactions, consistent with both mutational and simulation studies, which suggest that propofol inhibition results from binding closer to the M2 pore lining the α helix (Nury et al., 2011), or even from within the channel pore (LeBard et al., 2012).

DISCUSSION

Although there are likely other sites of action (Althoff et al., 2014; Brannigan et al., 2008; Jones and McNamee, 1988), a role for M4 in lipid sensing is highlighted by the identification of M4-bound lipids in the crystal structure of GLIC (Bocquet et al., 2009), as well as by mutagenesis data showing that changes in nAChR M4-lipid interactions influence channel function (Bouzat et al., 1998; Lasalde et al., 1996; Lee et al., 1994; Li et al., 1992; Shen et al., 2006; Tamamizu et al., 2000). M4 is also the site of action for neurosteroids (Hosie et al., 2006; Paradiso et al., 2001). In addition, a lipid-facing mutation on M4 in the muscle-type nAChR potentiates channel activity, leading to a CMS (Shen et al., 2006). M4, however, is distant from the channel-lining M2 α helix, as well as key structures that form the primary allosteric path between the agonist site and the channel gate (i.e., the β1-β2 and β6-β7 loops, the M2-M3 linker), thus raising the question of how changes in M4 structure alter channel function.

Our data show that enhanced M4-M1/M3 interactions potentiate pLGIC function while reduced interactions inhibit pLGIC function. This conclusion is based on four observations. First, molecular dynamics simulations show that aromatic residues at the M4-M1/M3 interface promote strong M4-M1/M3 interactions, with the elimination these aromatic residues leading to increased C_α-C_α carbon atom separations between M4 and M1/M3. Second, aromatic substitutions that promote M4-M1/M3 interactions enhance channel function while aromatic substitutions that weaken M4-M1/M3 interactions reduce channel function. Third, aromatic substitutions that modulate M4-M1/M3 interactions influence the potentiating effects of a lipid-facing M4 CMS mutation. No potentiation was observed when the CMS mutation was introduced into GLIC, which exhibits intrinsically effective M4-M1/M3 interactions, while strong potentiation was observed with ELIC, which lacks M4-M1/M3 stabilizing aromatic interactions. Significantly, engineering aromatic interactions into the M4-M1/M3 interface in ELIC abrogates the potentiating response. Finally, the strength of M4-M1/M3 interactions has no effect on the inhibitory effects of the drug propofol, which acts at a TMD site that does not directly involve M4 (LeBard et al., 2012; Nury et al., 2011).

Our proposed model of M4 action is supported by biophysical studies, which have shown that the orientation of nAChR M4, and thus presumably the interactions between M4 and M1/M3, is sensitive to its surrounding lipid environment (Antollini et al., 2005; Xu et al., 2005). The nAChR M4 moves halfway along the reaction coordinate between agonist binding and the open state (Mitra et al., 2004). Motion of M4 has also been detected during desensitization of GLIC (Velisetty et al., 2014), consistent with the desensitization effects observed here with some of the M4-M1/M3 interface aromatic residue substitutions (Figure S3).

There appears to be a particularly important role for the M4 C terminus in pLGIC function, in agreement with the proposed role of the M4 C terminus in lipid sensing by the muscle-type nAChR from *Torpedo*. Increasing levels of cholesterol and anionic lipids stabilize increasing proportions of agonist-responsive nAChRs (Baenziger et al., 2000; daCosta et al., 2002, 2009; Hamouda et al., 2006). In the absence of these activating lipids, the nAChR adopts an uncoupled conformation that exhibits resting-state-like agonist binding, but does not usually undergo agonist-induced conformational transitions (Baenziger et al., 2008; daCosta and Baenziger, 2009; daCosta et al., 2013). The M4 C terminus in both the nAChR and GLIC interacts directly with the β6-β7 loop, an important link between the agonist site and the transmembrane gate (Jha et al., 2007; Lee et al., 2009). The M4 C terminus also interacts with M3 adjacent to the M2-M3 linker, a structure that controls the orientation of the M2 gating α helix. Tighter M4 interactions with M1/M3 may facilitate interactions between the M4 C terminus and the β6-β7-loop, to form a β6-β7-loop conformation that participates optimally in channel gating (daCosta and Baenziger, 2009). Interestingly, the M4 C terminus does not interact directly with the β6-β7 loop in the ELIC crystal structure, which is significant because crystallized ELIC does not undergo channel gating (Gonzalez-Gutierrez et al., 2012). Weak M4 C-terminal interactions with M1/M3, as a consequence of detergent solubilization, may lead ELIC to adopt an uncoupled conformation (daCosta and Baenziger, 2013).

Finally, a key finding of our study is the demonstration that variable chemistry at the interface between M4 and M1/M3 in different pLGICs leads to variable M4-M1/M3 interactions, different ‘‘efficiencies’’ of coupling binding to gating, and different susceptibilities to potentiation by allosteric modulators, in this case a CMS mutation that acts on M4. GLIC has an extensive aromatic network at this interface that leads to effective M4-M1/M3 interactions along the entire length of M4, rendering the TMD less malleable and less sensitive to M4-targeting modulators. GLIC is insensitive to the potentiating effects of the lipid-facing M4 CMS mutation. GLIC also maintains efficient gating in lipid environments that stabilize an uncoupled nAChR (Labriola et al., 2013). ELIC, with no aromatic interactions in the C-terminal half of M4, exhibits weak M4-M1/M3 interactions in this region. ELIC is more sensitive than GLIC to M4-targeting modulators, such as the CMS mutation and lipids, although aromatic substitutions at the M4-M1/M3 abrogate sensitivity to both (Carswell et al., 2015). The nAChR, with relatively few inter-α-helix aromatic interactions, likely exhibits relatively weak M4-M1/M3 interactions along the entire length of M4, and is even more sensitive than ELIC to both the CMS mutation and lipids. Note that although the *Torpedo* nAChR structure does not exhibit tight interactions between M4 and M1/M3, M4 is not tilted away from M1/M3 as it is in the ELIC structure. The nAChR structure, however, was solved by cryo-electron microscopy using native nAChR membranes (Unwin, 2005; Unwin and Fujiyoshi, 2012), while the ELIC structure was solved by X-ray diffraction using crystals formed from detergent-solubilized ELIC (Hilf and Dutzler, 2008; Pan et al., 2012). In the native *Torpedo* membranes, there are ‘‘activating’’ lipids (cholesterol, anionic lipids, etc.) that stabilize a functional conformation, where M4 may associate effectively with M1/M3.

The chemistry at the M4-M1/M3 interface varies across human nAChR subunits, suggesting that human nAChRs exhibit variable M4-M1/M3 interactions, and thus possibly different sensitivities to allosteric modulators that act on M4. Knowledge of the subunit-specific roles of M4 in nAChR function may prove to be important for understanding the mechanisms by which cholinergic activity is modulated by changes in lipid composition that occur during the course of neurodegenerative disease.

EXPERIMENTAL PROCEDURES

RNA Constructs for Oocyte Expression

GLIC-pMT$_3$ was kindly provided by Dr. Pierre-Jean Corringer (Bocquet et al., 2009). The GLIC coding sequence was transferred to pSP64 without the C-terminal hemagglutinin tag. ELIC-pTLN was kindly provided by Dr. Raimund Dutzler (Zimmermann et al., 2012). A C-terminal Ala, a cloning artifact not present in the GenBank sequence (GenBank: POC7B7), was removed. Both the GLIC and ELIC plasmids have the α7 nAChR signal sequence followed by the GLIC or ELIC coding sequence. ELIC-pTLN and GLIC-pSP64 were linearized by MluI and EcoRI, respectively, and used to produce capped cRNA by in vitro transcription using the mMESSAGE mMACHINE SP6 kit (Ambion). All mutants were created using QuikChange site-directed mutagenesis kits (Agilent) and verified by sequencing.

Electrophysiology

Stage V–VI oocytes were isolated as previously described (Laitko et al., 2006). Oocytes were injected with the indicated amount of mRNA and allowed to incubate for 1 to 4 days at 16°C in ND96 + buffer (5 mM HEPES, 96 mM NaCl, 2 mM KCl, 1 mM MgCl$_2$, 1 mM CaCl$_2$, 2 mM pyruvate). Injected oocytes were placed in a RC-1Z oocyte chamber (Harvard Apparatus) containing the appropriate buffer (see below). Whole-cell currents were recorded using a two-electrode voltage-clamp apparatus (OC-725C oocyte clamp; Harvard Apparatus). The whole-cell currents were recorded while the appropriate buffer flowed through the oocyte chamber at a rate of 5–10 ml/min.

For GLIC, whole-cell currents were recorded from injected oocytes (3–13 ng cRNA) immersed in MES (2-(N-morpholino)ethanesulfonic acid) buffer (140 mM NaCl, 2.8 mM KCl, 2 mM MgCl$_2$, and 10 mM MES). Currents through the plasma membrane in response to pH jumps (pH 7.3 down to the indicated pH values) were measured with the transmembrane voltage clamped at voltages between −10 and −60 mV depending on the level of expression of each mutant GLIC. In the majority of cases, the holding potential was −20 mV. For ELIC, whole-cell currents were recorded from injected oocytes (0.2–10 ng cRNA) immersed in HEPES buffer (150 mM NaCl, 0.5 mM BaCl$_2$ 10 mM HEPES [pH 7.0]). In most cases, currents through the plasma membrane in response to cysteamine concentration jumps (from 0 mM up to the indicated values) were measured with the transmembrane voltage clamped at −40 mV.

Propofol (2,6 diisopropylphenol) was obtained from Aldrich (D126608). A stock solution was made by diluting liquid propofol to 1 M in DMSO. This solution was stored in glass in the dark, and diluted in MES or HEPES buffer immediately before use. Each oocyte was exposed to at most two different propofol concentrations. To avoid cumulative inhibitory effects, GLIC and ELIC IC$_{50}$ values were obtained through repeated measurement of relative inhibition caused by one concentration of propofol on a single oocyte, multiple times. The average inhibitory values at each concentration were used in calculation of the IC$_{50}$ using Prism's log (inhibitor) versus response (three-parameter) analysis.

Dose responses for each mutant were acquired from at least two different batches of oocytes. Each individual dose-response experiment was fit with a variable slope sigmoidal dose response, and the individual EC$_{50}$ and Hill coefficients from each experiment averaged to give the values ± SD. For the presented dose-response curves, the individual dose responses for each experiment were normalized and each data point averaged. Curve fits of the averaged data are presented, with the error bars referring to the SE.

Molecular Dynamics Simulations

Two systems containing GLIC from PDB: 4HFI (Sauguet et al., 2013) were prepared by protonating residues according to their standard states at pH 4.6, followed by either no mutations (WT-GLIC) or five simultaneous mutations (5Ala-GLIC) corresponding to the sites 1, 2, 3, 5, and 6 investigated in the experiments. Resolved lipids in the PDB structure were not included, although after about 50 ns of simulation, lipids bound to WT-GLIC in poses similar to those in PDB: 4HFI. For each system, the intact pentamer was placed in a 110 × 110 Å POPC membrane aligned parallel to the xy plane using CHARMM-GUI Membrane Builder (Jo et al., 2009). The system was solvated with a total height in z of 155 Å and neutralized, for a total of about 175,000 atoms per system. Atomistic molecular dynamics simulations were run with NAMD v2.9 (Phillips et al., 2005). The CHARMM36 force field was used for protein (Best et al., 2012; MacKerell et al., 1998) and phospholipid (Klauda et al., 2010) parameters, with parameters for TIP3P waters (Jorgensen et al., 1983) and ions (Beglov and Roux, 1994) corresponding to those traditionally used with CHARMM-based force fields. All simulations used periodic boundary conditions and particle mesh Ewald electrostatics. For more details, see Supplemental Information.

SUPPLEMENTAL INFORMATION

Supplemental Information includes Supplemental Experimental Procedures, three tables, and four figures and can be found with this article online at http://dx.doi.org/10.1016/j.str.2015.06.020.

AUTHOR CONTRIBUTIONS

All authors contributed to the design of the research. C.L.C., C.H., J.P.D.T., P.F.J., and J.A.S. created and/or characterized the mutants. C.H. also performed the propofol experiments. Molecular dynamics simulations were performed by S.M. and G.B. J.E.B, C.H., G.B., and C.L.C. wrote the paper. C.H., J.P.D.T., G.B., and C.L.C. created the figures.

ACKNOWLEDGMENTS

This research was funded by research grant 111243 to J.E.B. from the Canadian Institutes of Health Research (CIHR) and with support from the CIHR Training Program in Neurodegenerative Lipidomics (TGF-96121), and by research grants MCB1330728 and P01GM55876-14A1 from the National Science Foundation and NIH Research, respectively, to G.B. This project was supported with computational resources from the National Science Foundation XSEDE program through allocation NSF-MCB110149 as well as a local cluster funded by NSF-DBI1126052.

Received: December 18, 2014
Revised: June 1, 2015
Accepted: June 27, 2015
Published: July 30, 2015

REFERENCES

Althoff, T., Hibbs, R.E., Banerjee, S., and Gouaux, E. (2014). X-Ray structures of GluCl in apo states reveal a gating mechanism of Cys-loop receptors. Nature *512*, 333–337.

Antollini, S.S., Xu, Y., Jiang, H., and Barrantes, F.J. (2005). Fluorescence and molecular dynamics studies of the acetylcholine receptor γM4 transmembrane peptide in reconstituted systems. Mol. Membr. Biol. *22*, 471–483.

Baenziger, J.E., Morris, M.L., Darsaut, T.E., and Ryan, S.E. (2000). Effect of membrane lipid composition on the conformational equilibria of the nicotinic acetylcholine receptor. J. Biol. Chem. *275*, 777–784.

Baenziger, J.E., Ryan, S.E., Goodreid, M.M., Vuong, N.Q., Sturgeon, R.M., and daCosta, C.J. (2008). Lipid composition alters drug action at the nicotinic acetylcholine receptor. Mol. Pharmacol. *73*, 880–890.

Baenziger, J.E., Henault, C.M., Therien, J.P., and Sun, J. (2015). Nicotinic acetylcholine receptor-lipid interactions: mechanistic insight and biological function. Biochim. Biophys. Acta *1848*, 1806–1817.

Barrantes, F.J. (2003). Modulation of nicotinic acetylcholine receptor function through the outer and middle rings of transmembrane domains. Curr. Opin. Drug Discov. Devel. *6*, 620–632.

Barrantes, F.J. (2015). Phylogenetic conservation of protein-lipid motifs in pentameric ligand-gated ion channels. Biochim. Biophys. Acta *1848*, 1796–1805.

Beglov, D., and Roux, B. (1994). Finite representation of an infinite bulk system: solvent boundary potential for computer simulations. J. Chem. Phys. *100*, 9050–9063.

Best, R.B., Zhu, X., Shim, J., Lopes, P.E., Mittal, J., Feig, M., and Mackerell, A.D., Jr. (2012). Optimization of the additive CHARMM all-atom protein force field targeting improved sampling of the backbone phi, psi and side-chain chi(1) and chi(2) dihedral angles. J. Chem. Theory Comput. *8*, 3257–3273.

Bocquet, N., Nury, H., Baaden, M., Le Poupon, C., Changeux, J.P., Delarue, M., and Corringer, P.J. (2009). X-ray structure of a pentameric ligand-gated ion channel in an apparently open conformation. Nature *457*, 111–114.

Bouzat, C., Roccamo, A.M., Garbus, I., and Barrantes, F.J. (1998). Mutations at lipid-exposed residues of the acetylcholine receptor affect its gating kinetics. Mol. Pharmacol. *54*, 146–153.

Bouzat, C., Barrantes, F., and Sine, S. (2000). Nicotinic receptor fourth transmembrane domain: hydrogen bonding by conserved threonine contributes to channel gating kinetics. J. Gen. Physiol. *115*, 663–672.

Brannigan, G., Henin, J., Law, R., Eckenhoff, R., and Klein, M.L. (2008). Embedded cholesterol in the nicotinic acetylcholine receptor. Proc. Natl. Acad. Sci. USA *105*, 14418–14423.

Carswell, C.L., Sun, J., and Baenziger, J.E. (2015). Intramembrane aromatic interactions influence the lipid sensitivities of pentameric ligand-gated ion channels. J. Biol. Chem. *290*, 2496–2507.

daCosta, C.J., and Baenziger, J.E. (2009). A lipid-dependent uncoupled conformation of the acetylcholine receptor. J. Biol. Chem. *284*, 17819–17825.

daCosta, C.J., and Baenziger, J.E. (2013). Gating of pentameric ligand-gated ion channels: structural insights and ambiguities. Structure *21*, 1271–1283.

daCosta, C.J., Ogrel, A.A., McCardy, E.A., Blanton, M.P., and Baenziger, J.E. (2002). Lipid-protein interactions at the nicotinic acetylcholine receptor. A functional coupling between nicotinic receptors and phosphatidic acid-containing lipid bilayers. J. Biol. Chem. *277*, 201–208.

daCosta, C.J., Medaglia, S.A., Lavigne, N., Wang, S., Carswell, C.L., and Baenziger, J.E. (2009). Anionic lipids allosterically modulate multiple nicotinic acetylcholine receptor conformational equilibria. J. Biol. Chem. *284*, 33841–33849.

daCosta, C.J., Dey, L., Therien, J.P., and Baenziger, J.E. (2013). A distinct mechanism for activating uncoupled nicotinic acetylcholine receptors. Nat. Chem. Biol. *9*, 701–707.

Duret, G., Van Renterghem, C., Weng, Y., Prevost, M., Moraga-Cid, G., Huon, C., Sonner, J.M., and Corringer, P.J. (2011). Functional prokaryotic-eukaryotic chimera from the pentameric ligand-gated ion channel family. Proc. Natl. Acad. Sci. USA *108*, 12143–12148.

Gonzalez-Gutierrez, G., Lukk, T., Agarwal, V., Papke, D., Nair, S.K., and Grosman, C. (2012). Mutations that stabilize the open state of the *Erwinia chrisanthemi* ligand-gated ion channel fail to change the conformation of the pore domain in crystals. Proc. Natl. Acad. Sci. USA *109*, 6331–6336.

Grutter, T., de Carvalho, L.P., Dufresne, V., Taly, A., Edelstein, S.J., and Changeux, J.P. (2005). Molecular tuning of fast gating in pentameric ligand-gated ion channels. Proc. Natl. Acad. Sci. USA *102*, 18207–18212.

Haeger, S., Kuzmin, D., Detro-Dassen, S., Lang, N., Kilb, M., Tsetlin, V., Betz, H., Laube, B., and Schmalzing, G. (2010). An intramembrane aromatic network determines pentameric assembly of Cys-loop receptors. Nat. Struct. Mol. Biol. *17*, 90–98.

Hamouda, A.K., Sanghvi, M., Sauls, D., Machu, T.K., and Blanton, M.P. (2006). Assessing the lipid requirements of the *Torpedo californica* nicotinic acetylcholine receptor. Biochemistry *45*, 4327–4337.

Henault, C.M., Sun, J., Therien, J.P., daCosta, C.J., Carswell, C.L., Labriola, J.M., Juranka, P.J., and Baenziger, J.E. (2015). The role of the M4 lipid-sensor in the folding, trafficking, and allosteric modulation of nicotinic acetylcholine receptors. Neuropharmacology *96*, 157–168.

Hibbs, R.E., and Gouaux, E. (2011). Principles of activation and permeation in an anion-selective Cys-loop receptor. Nature *474*, 54–60.

Hilf, R.J., and Dutzler, R. (2008). X-ray structure of a prokaryotic pentameric ligand-gated ion channel. Nature *452*, 375–379.

Hilf, R.J., and Dutzler, R. (2009). Structure of a potentially open state of a proton-activated pentameric ligand-gated ion channel. Nature *457*, 115–118.

Hosie, A.M., Wilkins, M.E., da Silva, H.M., and Smart, T.G. (2006). Endogenous neurosteroids regulate GABAA receptors through two discrete transmembrane sites. Nature *444*, 486–489.

Jha, A., Cadugan, D.J., Purohit, P., and Auerbach, A. (2007). Acetylcholine receptor gating at extracellular transmembrane domain interface: the cys-loop and M2-M3 linker. J. Gen. Physiol. *130*, 547–558.

Jo, S., Lim, J.B., Klauda, J.B., and Im, W. (2009). CHARMM-GUI Membrane Builder for mixed bilayers and its application to yeast membranes. Biophys. J. *97*, 50–58.

Jones, O.T., and McNamee, M.G. (1988). Annular and nonannular binding sites for cholesterol associated with the nicotinic acetylcholine receptor. Biochemistry *27*, 2364–2374.

Jorgensen, W.L., Chandrasekhar, J., Madura, J.D., Impey, R.W., and Klein, M.L. (1983). Comparison of simple potential functions for simulating liquid water. J. Chem. Phys. *79*, 926–935.

Klauda, J.B., Venable, R.M., Freites, J.A., O'Connor, J.W., Tobias, D.J., Mondragon-Ramirez, C., Vorobyov, I., MacKerell, A.D., Jr., and Pastor, R.W. (2010). Update of the CHARMM all-atom additive force field for lipids: validation on six lipid types. J. Phys. Chem. B *114*, 7830–7843.

Labriola, J.M., Pandhare, A., Jansen, M., Blanton, M.P., Corringer, P.J., and Baenziger, J.E. (2013). Structural sensitivity of a prokaryotic pentameric ligand-gated ion channel to its membrane environment. J. Biol. Chem. *288*, 11294–11303.

Laitko, U., Juranka, P.F., and Morris, C.E. (2006). Membrane stretch slows the concerted step prior to opening in a Kv channel. J. Gen. Physiol. *127*, 687–701.

Lasalde, J.A., Tamamizu, S., Butler, D.H., Vibat, C.R., Hung, B., and McNamee, M.G. (1996). Tryptophan substitutions at the lipid-exposed transmembrane segment M4 of *Torpedo californica* acetylcholine receptor govern channel gating. Biochemistry *35*, 14139–14148.

LeBard, D.N., Henin, J., Eckenhoff, R.G., Klein, M.L., and Brannigan, G. (2012). General anesthetics predicted to block the GLIC pore with micromolar affinity. PLoS Comput. Biol. *8*, e1002532.

Lee, W.Y., and Sine, S.M. (2005). Principal pathway coupling agonist binding to channel gating in nicotinic receptors. Nature *438*, 243–247.

Lee, Y.H., Li, L., Lasalde, J., Rojas, L., McNamee, M., Ortiz-Miranda, S.I., and Pappone, P. (1994). Mutations in the M4 domain of *Torpedo californica* acetylcholine receptor dramatically alter ion channel function. Biophys. J. *66*, 646–653.

Lee, W.Y., Free, C.R., and Sine, S.M. (2009). Binding to gating transduction in nicotinic receptors: Cys-loop energetically couples to pre-M1 and M2-M3 regions. J. Neurosci. *29*, 3189–3199.

Li, L., Lee, Y.H., Pappone, P., Palma, A., and McNamee, M.G. (1992). Site-specific mutations of nicotinic acetylcholine receptor at the lipid-protein interface dramatically alter ion channel gating. Biophys. J. *62*, 61–63.

Lummis, S.C., Beene, D.L., Lee, L.W., Lester, H.A., Broadhurst, R.W., and Dougherty, D.A. (2005). Cis-trans isomerization at a proline opens the pore of a neurotransmitter-gated ion channel. Nature *438*, 248–252.

MacKerell, A.D., Bashford, D., Bellott, M., Dunbrack, R.L., Evanseck, J.D., Field, M.J., Fischer, S., Gao, J., Guo, H., Ha, S., et al. (1998). All-atom empirical potential for molecular modeling and dynamics studies of proteins. J. Phys. Chem. B *102*, 3586–3616.

Miller, P.S., and Aricescu, A.R. (2014). Crystal structure of a human GABAA receptor. Nature *512*, 270–275.

Mitra, A., Bailey, T.D., and Auerbach, A.L. (2004). Structural dynamics of the M4 transmembrane segment during acetylcholine receptor gating. Structure *12*, 1909–1918.

Nury, H., Van Renterghem, C., Weng, Y., Tran, A., Baaden, M., Dufresne, V., Changeux, J.P., Sonner, J.M., Delarue, M., and Corringer, P.J. (2011). X-ray structures of general anaesthetics bound to a pentameric ligand-gated ion channel. Nature *469*, 428–431.

Pan, J., Chen, Q., Willenbring, D., Yoshida, K., Tillman, T., Kashlan, O.B., Cohen, A., Kong, X.P., Xu, Y., and Tang, P. (2012). Structure of the pentameric ligand-gated ion channel ELIC cocrystallized with its competitive antagonist acetylcholine. Nat. Commun. *3*, 714.

Paradiso, K., Zhang, J., and Steinbach, J.H. (2001). The C terminus of the human nicotinic alpha4beta2 receptor forms a binding site required for potentiation by an estrogenic steroid. J. Neurosci. *21*, 6561–6568.

Phillips, J.C., Braun, R., Wang, W., Gumbart, J., Tajkhorshid, E., Villa, E., Chipot, C., Skeel, R.D., Kale, L., and Schulten, K. (2005). Scalable molecular dynamics with NAMD. J. Comput. Chem. *26*, 1781–1802.

Rienzo, M., Lummis, S.C., and Dougherty, D.A. (2014). Structural requirements in the transmembrane domain of GLIC revealed by incorporation of noncanonical histidine analogs. Chem. Biol. *21*, 1700–1706.

Sauguet, L., Poitevin, F., Murail, S., Van Renterghem, C., Moraga-Cid, G., Malherbe, L., Thompson, A.W., Koehl, P., Corringer, P.J., Baaden, M., et al. (2013). Structural basis for ion permeation mechanism in pentameric ligand-gated ion channels. EMBO J. *32*, 728–741.

Sauguet, L., Shahsavar, A., Poitevin, F., Huon, C., Menny, A., Nemecz, A., Haouz, A., Changeux, J.P., Corringer, P.J., and Delarue, M. (2014). Crystal structures of a pentameric ligand-gated ion channel provide a mechanism for activation. Proc. Natl. Acad. Sci. USA *111*, 966–971.

Shen, X.M., Deymeer, F., Sine, S.M., and Engel, A.G. (2006). Slow-channel mutation in acetylcholine receptor alphaM4 domain and its efficient knockdown. Ann. Neurol. *60*, 128–136.

Tamamizu, S., Guzman, G.R., Santiago, J., Rojas, L.V., McNamee, M.G., and Lasalde-Dominicci, J.A. (2000). Functional effects of periodic tryptophan substitutions in the alpha M4 transmembrane domain of the Torpedo californica nicotinic acetylcholine receptor. Biochemistry *39*, 4666–4673.

Unwin, N. (2005). Refined structure of the nicotinic acetylcholine receptor at 4 Å resolution. J. Mol. Biol. *346*, 967–989.

Unwin, N., and Fujiyoshi, Y. (2012). Gating movement of acetylcholine receptor caught by plunge-freezing. J. Mol. Biol. *422*, 617–634.

Velisetty, P., Chalamalasetti, S.V., and Chakrapani, S. (2014). Structural basis for allosteric coupling at the membrane-protein interface in *Gloeobacter violaceus* ligand-gated ion channel (GLIC). J. Biol. Chem. *289*, 3013–3025.

Wang, H.L., Cheng, X., and Sine, S.M. (2012). Intramembrane proton binding site linked to activation of bacterial pentameric ion channel. J. Biol. Chem. *287*, 6482–6489.

Xu, Y., Barrantes, F.J., Luo, X., Chen, K., Shen, J., and Jiang, H. (2005). Conformational dynamics of the nicotinic acetylcholine receptor channel: a 35-ns molecular dynamics simulation study. J. Am. Chem. Soc. *127*, 1291–1299.

Zimmermann, I., Marabelli, A., Bertozzi, C., Sivilotti, L.G., and Dutzler, R. (2012). Inhibition of the prokaryotic pentameric ligand-gated ion channel ELIC by divalent cations. PLoS Biol. *10*, e1001429.

Supplementary Table S1[a]
Inter-residue interactions significantly affected by the aromatic-to-Ala mutations[b]

M3 Residue	M4 Residue	ΔE (kcal/mol)	Comments
Y254 (3)	F314 (2)	3.6	Interactions display expected behavior for pi-pi stacking in WT-GLIC
Y254 (3)	N307	3.4	Loss of hydrogen bond between residues in 5Ala-GLIC
Y254 (3)	F315 (1)	1.8	Interactions display expected behavior for pi-pi stacking in WT-GLIC
T253	F314 (2)	1.6	Pair residues widely separated in 5Ala-GLIC compared to WT-GLIC; equivalent loss of both electrostatic and van der Waals interactions
M252	F314 (2)	1.1	Hydrophobic interactions reduced significantly in 5Ala-GLIC
M252	F315 (1)	1.1	Electrostatic interactions between terminal dipole on F315A and M252 backbone in 5Ala-GLIC are not present in WT-GLIC, in which F315 interacts more strongly with T253

[a] Table S1 relates to Figure 2.

[b] Pair interactions significantly affected by mutation. Non-bonded energies (van der Waals and electrostatic) were measured for each pair involving a substitution in both WT-GLIC and 5Ala-GLIC simulated receptors and the resulting energy difference $\Delta E = E_{5Ala}-E_{WT}$ was calculated. Those pairs with $|\Delta E| > 1.0$ kcal/mol are listed here, in order of descending effect. Numbers shown in parentheses correspond to the residue numbering scheme in Figure 3.

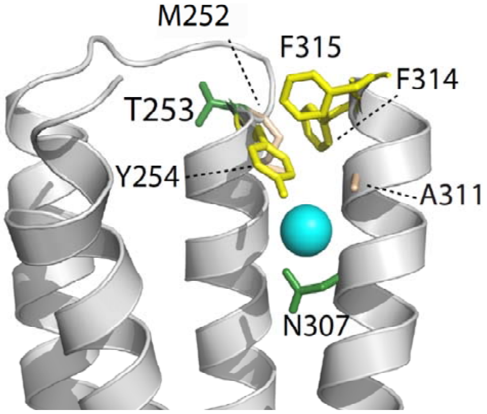

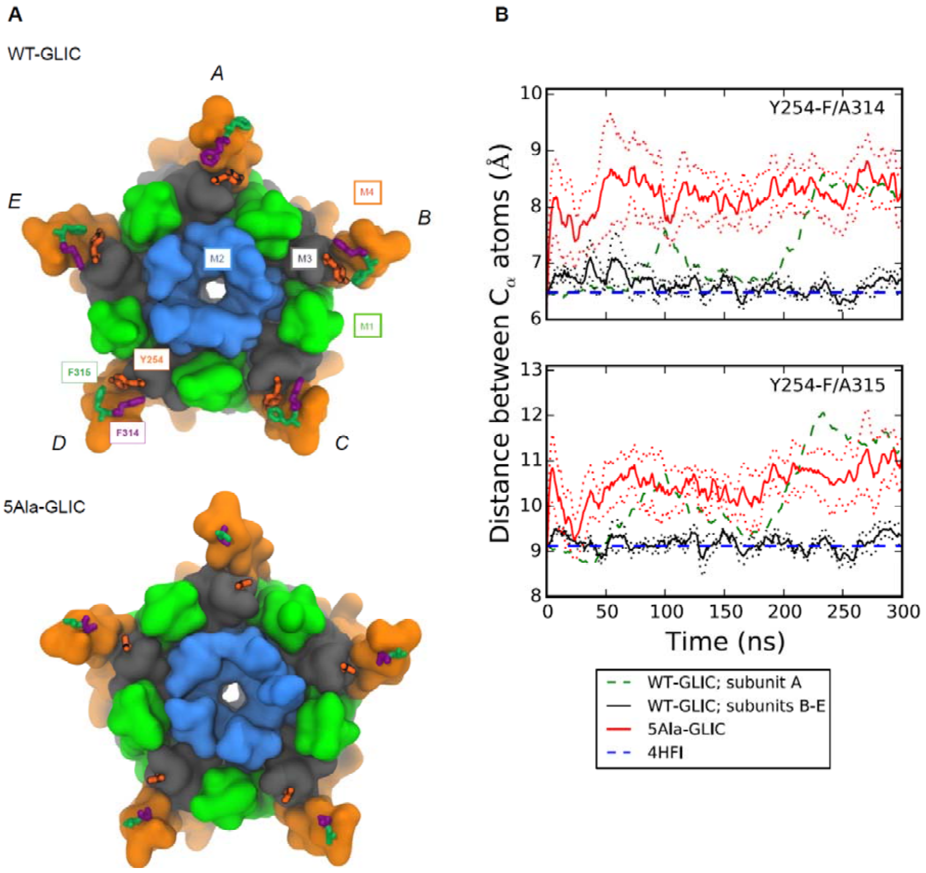

Figure S1. Effects of Ala mutations on the Cα carbon atom separations.

The left column shows the WT-GLIC (top) and 5Ala-GLIC (bottom) homopentameric structures at the end of the 300 ns simulations. Individual TMD α-helices are shown in surface representations with M1, green; M2, blue; M3, gray; and M4, orange; also shown in surface representation is the M2-M3 loop (yellow) and a portion of the ECD (purple) closest to the interface with the TMD. The three residues of the aromatic cluster are shown as sticks. Note that in four of the five subunits of WT-GLIC, the aromatic cluster involving Y254, F314 and F315 is maintained over the time course of the simulations. In the subunit labeled A, M4 rotates slightly so that F314 moves toward Y254, and F315 projects out to interact directly with lipids. The final conformation of M4 in subunit A is similar to that observed in the single subunit TMD simulations shown in Supplementary Figure 3. The panels in the right column show the evolution of the Cα carbon atom separation distances for residues in the C-terminal aromatic cluster over the time course of simulations run for both WT-GLIC (separated into subunit A, in which the aromatic cluster is not preserved, and subunits B-E, in which it is preserved) and 5Ala-GLIC. Dotted lines represent 95% confidence intervals based on deviation across subunits. Figure S1 relates to Figure 2.

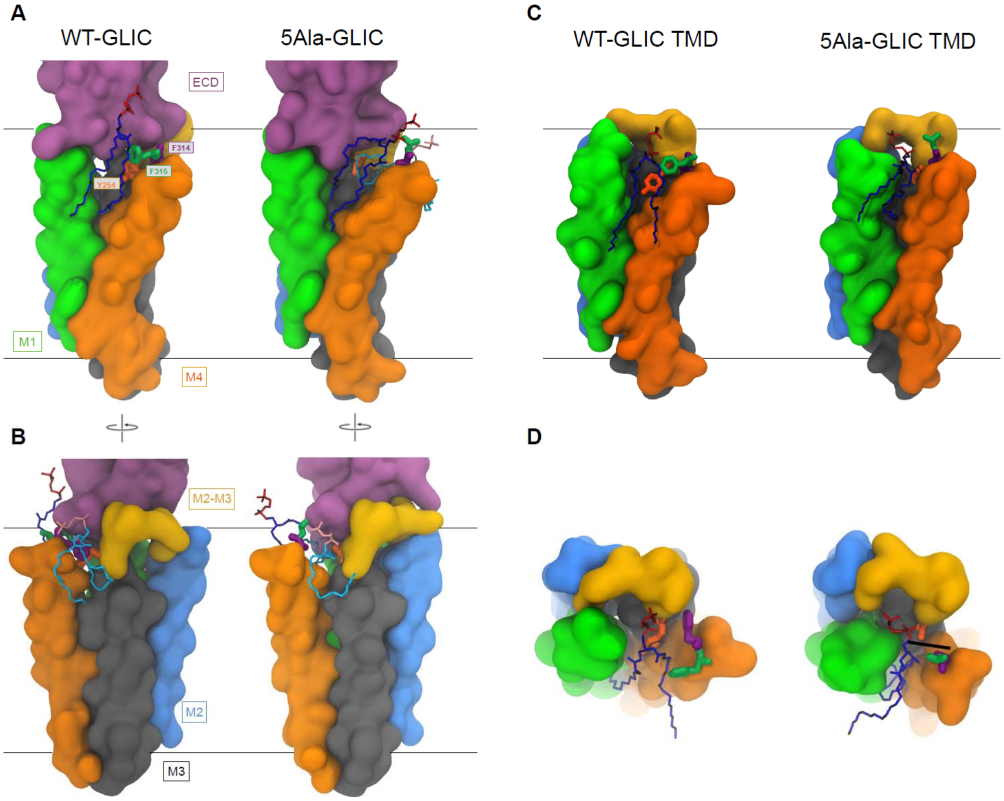

Figure S2. Alanine mutations at the M4-M1/M3 interface lead to altered lipid binding.
A) Side views of a single TMD extracted after the 300 ns simulations of intact homopentamers of WT-GLIC (left) and 5Ala-GLIC (right) , showing the interactions of POPC molecules with M1-M4 interface (top) and M3-M4 interface (bottom), with protein coloring and representation as in Fig. S1. POPC molecules are shown in stick representations, with acyl chains in blue/cyan and PC headgroups in red/pink. The average coordinates of one POPC molecule bound in the WT-GLIC simulations are consistent with the position of the bound PC lipid molecule modeled at the M1-M4 interface in the GLIC crystal structure (PDB code 4HFI). **B)** Same as **(A)**, but with the view rotated ~180°. The simulations suggest that the M4 C-terminal cluster of aromatic residues in the WT- GLIC homopentamer are more effective at preventing the penetration of lipids into the M1/M3/M4 α-helical bundle than the corresponding alanine residues in 5Ala-GLIC. One interpretation is that the strong π-π stacking interactions in WT-GLIC "pull" M4 toward M3 thus preventing lipid binding, whereas mutation of these residues to alanine weakens M4-M1/M3 interactions (see Supplementary Table 1) thus tilting M4 away from M1/M3 allowing the penetration of lipids into the interface. Alternatively or in addition, the aromatic residues in WT-GLIC may sterically prevent lipid penetration into the M4-M1/M3 interface. The increase in free volume that occurs upon mutation of the bulky aromatic side chains to alanine in 5Ala-GLIC may allow lipids to penetrate further into the

interface driving the increase in separation between the M4 and M1/M3. Note, however, that the mutation of the aromatic residues to alanine in 5Ala-GLIC leads almost immediately (within the first 20 ns of the simulations) to an increased separation between the Cα atoms (Supplementary Fig. 1). This equilibration time is much faster than the typical equilibration times for lipids in buried binding sites (~100-150 ns). The rapid movement of M4 thus suggests that the increased distances between M4 and M1/M3 likely results directly from weakened M4-M1/M3 interactions. **C)** Side views and **D)** top down views of a single TMD extracted after the 250 ns from single-subunit-TMD simulations of WT-GLIC (left) and 5Ala-GLIC (right). In the single-subunit-TMD simulations, removal of the ECD allows the POPC molecule to penetrate farther into the TMD α-helical bundle. In WT-GLIC TMD, the bound POPC headgroup interposes between M1 and M3 with the long axis of the glycerol backbone parallel to a line separating the centers of M1 and M3. M4 rotates slightly so that in this conformation, a section of one acyl chain is sandwiched between Y254 and F315, stabilized by hydrophobic interactions. In 5Ala-GLIC TMD, the analogous lipid is oriented with the long axis of the glycerol backbone perpendicular to that observed in WT-GLIC-TMD, parallel to a line pointing from the glycerol backbone center to the subunit center; this deeper conformation is facilitated by the mutation of five bulky aromatic residues into alanine, which leaves increased free volume in the core of the helical bundle. Note that both of these lipid conformations would sterically clash with the ECD, and are consequently highly unfavorable in the intact pentamer. **The importance of the latter simulations is that they show that subtle changes in conformation can dramatically alter lipid binding to the M4-M1/M3 interface.** Figure S2 relates to Figure 2.

.2 Appendix B: A novel bifunctional alkylphenol anesthetic allows characterization of $\mathbf{GABA_AR}$ subunit binding selectivity in synaptosomes.

This chapter involves experimental work conducted by experimentalists in University of Pennsylvania. The results were validated by us using computational techniques and analysis were performed using tcl and python scripts.

⌘ *Author's Choice*

THE JOURNAL OF BIOLOGICAL CHEMISTRY VOL. 291, NO. 39, pp. 20473–20486, September 23, 2016
© 2016 by The American Society for Biochemistry and Molecular Biology, Inc. Published in the U.S.A.

A Novel Bifunctional Alkylphenol Anesthetic Allows Characterization of γ-Aminobutyric Acid, Type A (GABA_A), Receptor Subunit Binding Selectivity in Synaptosomes[*][S]

Received for publication, May 9, 2016, and in revised form, July 25, 2016 Published, JBC Papers in Press, July 26, 2016, DOI 10.1074/jbc.M116.736975

Kellie A. Woll[‡§], Sruthi Murlidaran[¶], Benika J. Pinch[‖], Jérôme Hénin[**], Xiaoshi Wang[‡‡], Reza Salari[¶§§], Manuel Covarrubias[¶¶], William P. Dailey[‖], Grace Brannigan[¶§§], Benjamin A. Garcia[‡‡], and Roderic G. Eckenhoff[‡1]

From the Departments of [‡]Anesthesiology and Critical Care and [§]Pharmacology and the [‡‡]Epigenetics Program, Department of Biochemistry and Biophysics, University of Pennsylvania Perelman School of Medicine, Philadelphia, Pennsylvania 19104, the [¶]Center for Computational and Integrative Biology and [§§]Department of Physics, Rutgers University, Camden, New Jersey 08102, the [‖]Department of Chemistry, University of Pennsylvania School of Arts and Sciences, Philadelphia, Pennsylvania 19104, the [**]Laboratoire de Biochimie Théorique, Institut de Biologie Physico-Chimique, CNRS UMR 8251 and Université Paris Diderot, 5013 Paris, France, and the [¶¶]Department of Neuroscience and Farber Institute for Neuroscience, Sidney Kimmel Medical College, Thomas Jefferson University, Philadelphia, Pennsylvania 19107

Propofol, an intravenous anesthetic, is a positive modulator of the GABA_A receptor, but the mechanistic details, including the relevant binding sites and alternative targets, remain disputed. Here we undertook an in-depth study of alkylphenol-based anesthetic binding to synaptic membranes. We designed, synthesized, and characterized a chemically active alkylphenol anesthetic (2-((prop-2-yn-1-yloxy)methyl)-5-(3-(trifluoromethyl)-3*H*-diazirin-3-yl)phenol, AziP*m-click* (1)), for affinity-based protein profiling (ABPP) of propofol-binding proteins in their native state within mouse synaptosomes. The ABPP strategy captured ~4% of the synaptosomal proteome, including the unbiased capture of five α or β GABA_A receptor subunits. Lack of $\gamma 2$ subunit capture was not due to low abundance. Consistent with this, independent molecular dynamics simulations with alchemical free energy perturbation calculations predicted selective propofol binding to interfacial sites, with higher affinities for α/β than γ-containing interfaces. The simulations indicated hydrogen bonding is a key component leading to propofol-selective binding within GABA_A receptor subunit interfaces, with stable hydrogen bonds observed between propofol and α/β cavity residues but not γ cavity residues. We confirmed this by introducing a hydrogen bond-null propofol analogue as a protecting ligand for targeted-ABPP and observed a lack of GABA_A receptor subunit protection. This investigation demonstrates striking interfacial GABA_A receptor subunit selectivity in the native milieu, suggesting that asymmetric occupancy of heteropentameric ion channels by alkylphenol-based anesthetics is sufficient to induce modulation of activity.

γ-Aminobutyric acid (GABA) is well established as the major inhibitory neurotransmitter within the adult mammalian brain. The majority of GABA inhibitory activity is a consequence of binding to a set of pentameric ligand-gated ion channels called the GABA type A (GABA_A) receptor. GABA_A receptors are largely heteromeric protein complexes composed of five different subunits that form a central pore that mediates chloride flux. Including the multiple isoforms, heterogeneity of the receptor is extensive with potentially more than 800 combinations (1). This complexity can be partially simplified by the degrees of selective cellular localization for some subunits and isoforms. Synaptic GABA_A receptors contribute considerably to the communication between neurons, including influencing presynaptic neurotransmitter release as well as inducing postsynaptic hyperpolarization (1–4). Numerous studies have indicated that synaptic GABA_A receptors are predominantly of a $2\alpha{:}2\beta{:}1\gamma$ stoichiometry (5, 6) that organizes in an alternating order (*e.g.* $\gamma\alpha\beta\alpha\beta$ anti-clockwise as seen from synaptic cleft) (5–7). The resulting complex yields an abundance of potential ligand interaction surfaces within one heteropentamer, including at least four unique subunit interfaces. As such, it is justified that the composition and orientation of subunits are functionally significant, with different pharmacological properties pertaining to different GABA_A receptor complexes (1, 8).

Numerous drugs influence GABA_A receptor activity, including general anesthetics that are used extensively in modern medicine and in scientific research (9). For example, 2,6-diisopropylphenol (propofol[2] ((Fig. 1) has been strongly implicated as a modulator of the GABA_A receptor. Relatively low concentrations of this alkylphenol significantly potentiate GABA-induced current, an action that hyperpolarizes the post-synaptic membrane and thereby likely contributes to hypnosis and possibly other anesthesia phenotypes (10, 11). Furthermore, multiple reports indicate that phasic inhibition is particularly sen-

---

[*] This work was supported by National Institutes of Health Grants GM055876 and GM107174, Department of Defense Grant BC123187P1, and National Science Foundation Graduate Research Fellowship DGE-1321851. The authors declare that they have no conflicts of interest with the contents of this article. The content is solely the responsibility of the authors and does not necessarily represent the official views of the National Institutes of Health.

⌘ *Author's Choice*—Final version free via Creative Commons CC-BY license.

[S] This article contains supplemental Table S1 and S2–S32.

[1] To whom correspondence should be addressed: 311A John Morgan Bldg., 3620 Hamilton Walk, Philadelphia, PA 19104-6112. Tel.: 215-746-8699; Fax: 215-349-5078; E-mail: roderic.eckenhoff@uphs.upenn.edu.

[2] The abbreviations used are: propofol, 2,6-diisopropylphenol; ABPP, affinity-based protein profiling; MD, molecular dynamics; AFEP, alchemical free energy perturbation; 1-AMA, 1-aminoanthracene; MS, mass spectrometry; TMT, tandem mass tag; fropofol, 2-fluoro-1,3-diisopropylbenzene; CI, confidence interval.

Downloaded from http://www.jbc.org/ at Rutgers University on April 15, 2018

sitive to low concentrations of propofol, suggesting that synaptic GABAergic signaling is a critical pathway for the anesthetic's pharmacological effects (12–14).

Investigations have focused on the potential binding sites within heterologously expressed $\alpha\beta\gamma$ GABA$_A$ receptors. A wide range of mutagenesis studies have probed ligand-gated ion channel electrophysiology and have shown that mutation of various residues predicted to reside within subunit interfacial regions alters propofol modulation (9, 15–17). Particular point mutations within β subunits, such as Asn-265, greatly decreased propofol-positive modulation (11, 18). Our previous work using the tritiated photoaffinity ligand (PAL) *meta*-azipropofol demonstrated frequent labeling of interfacial residues within the heterologously expressed Cys loop superfamily of receptors, including $\alpha_1\beta_3\gamma_2$ GABA$_A$ receptors (19). These findings further suggest that subunit interfaces are potentially involved in propofol modulation. Structure-activity relationships applying alkylphenol analogues and/or other chemical derivatives (20, 21), molecular dynamic (MD) simulations (22, 23), as well as other investigations have suggested complex physicochemical interactions between propofol and GABA$_A$ receptors (24). Together, these studies have provided insight regarding the potential mechanism by which propofol perturbs GABA$_A$ receptor protein dynamics. However, in addition to the biased nature of using heterologously expressed receptors, it is recognized that each method has experimental limitations that result in the current uncertainty regarding alkylphenol interactions within the receptor.

Our objective was to advance the current understanding of anesthetic interactions with heteromeric receptors by addressing the interaction(s) of alkylphenols with GABA$_A$ receptors within their native synaptic milieu. Our approach applied a novel chemically active alkylphenol anesthetic for quantitative affinity-based protein profiling (ABPP) of propofol within synaptosomes. By utilizing a native tissue-derived system, the relative GABA$_A$ receptor subunit expression, pentameric composition, protein-protein interactions, and lipid milieu are maintained. We assessed these binding results with independent MD simulations using the alchemical free energy perturbation (AFEP) algorithm (25) to predict potential molecular recognition elements within $\alpha_1\beta_3\gamma_2$ GABA$_A$ receptor-binding sites. Finally, we examined the impact of these molecular recognition elements within the synaptic GABA$_A$ receptors with photoaffinity protection experiments. Our studies led to the unbiased identification of GABA$_A$ receptor subunits in native synaptic membranes as alkylphenol-binding proteins. Our investigation suggested higher affinity interactions for $\beta+/\alpha-$ and $\alpha+/\beta-$ interfacial sites relative to γ-containing subunit interfaces and hydrogen bonding as the major recognition element for the alkylphenol-GABA$_A$ receptor complex.

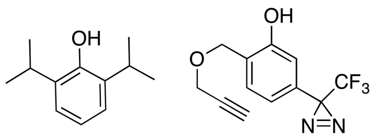

propofol AziP*m-click* (**1**)

FIGURE 1. **Clickable photoactive propofol analogue.** Chemical structures of propofol and AziP*m-click* (**1**).

Results

Synthesis of AziPm-click (1)—To identify the alkylphenol-binding proteins within the synaptic proteome, we developed 2-((prop-2-yn-1-yloxy)methyl)-5-(3-(trifluoromethyl)-3*H*-diazirin-3-yl)phenol, or AziP*m-click* (**1**), a photoaffinity tandem bioorthogonal alkylphenol anesthetic ligand (Fig. 1). AziP*m-click* (**1**) was designed to integrate two chemically active groups that allow for ABPP as follows: 1) a diazirine photoreactive group to covalently label protein interaction sites, and 2) an alkynyl group for covalent attachment of a reporter tag by 1,3-dipolarcycloaddition reaction (*e.g.* "Click Chemistry") to capture and identify photoaffinity labeled proteins within the synaptic proteome.

Synthesis of AziP*m-click* (**1**), shown in Scheme 1 (described in supplemental S2–S7), starts with the previously reported 4-bromo-2-(methoxymethoxy)-1-methylbenzene (**2**) (26). Conversion of **2** to the Grignard reagent using magnesium in THF followed by treatment with pyrrolidine trifluoroacetamide produced trifluoromethyl ketone **3**. Conversion of **3** to the oxime **4** and oxime tosylate **5** followed standard procedures. Treatment of **5** with excess liquid ammonia produced diaziridine **6** that was oxidized to the diazirine **7** using pyridinium dichromate. Benzylic bromination using *N*-bromosuccinimide produced **8,** which was treated with the sodium salt of propargylic alcohol in tetrahydrofuran to provide **9**. Removal of the methoxymethyl protecting group in the presence of the propargylic ether required carefully controlled conditions and was finally accomplished using sodium hydrogen sulfate-impregnated silica gel in methylene chloride (27).

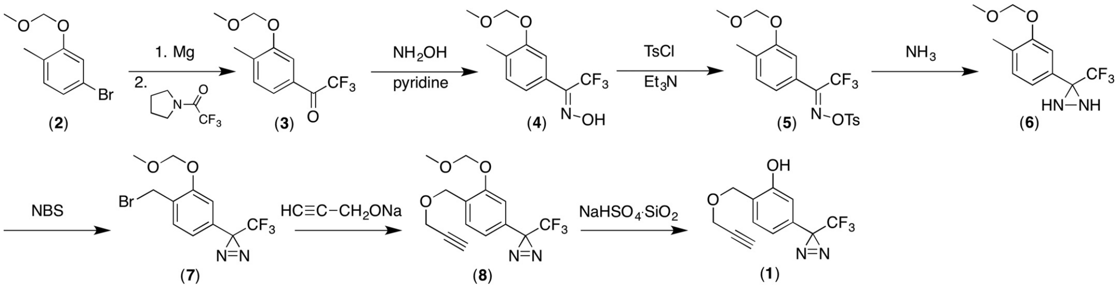

SCHEME 1

Downloaded from http://www.jbc.org/ at Rutgers University on April 15, 2018

TABLE 1

Physicochemical properties

	Mass	Density	clogP
	Da	*g/ml*	
AziP*m-click* (**1**)	270	1.19	3.55
propofol	178	0.96	3.79

TABLE 2

Equilibrium binding parameters

ITC is isothermal calorimetry.

	Propofol		AziP*m-click* (**1**)	
	ITC	1-AMA displacement[a]	ITC	1-AMA displacement[a]
K_D (95% CI; μm)	9 (7.1–11)	2.4 (1.3–4.4)	22 (20- 24)	4.0 (1.8–8.7)
Hill slope (mean ± S.E.)	1[b]	−1.1 ± 0.33	1[b]	−0.97 ± 0.39

[a] K_D indicates fluorescence data derived from the Cheng-Prusoff equation.

[b] Stoichiometry of HS*a*F sites was modeled for one site; therefore, the Hill slope is fixed at 1.

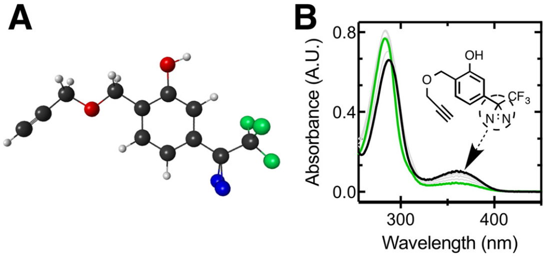

FIGURE 2. **AziPm-*click* (1) geometry and photoreactivity.** *A*, ball and stick structure of AziPm-*click* (**1**) in predicted lowest energy conformation (*gray*, carbon; *red*, oxygen; *blue*, nitrogen, *green*, fluorine). *B*, UV absorption spectra of AziPm-*click* (**1**) (175 μM) in double distilled water (*black line*) over the course of UV irradiation time points (*gray* and *green lines*).

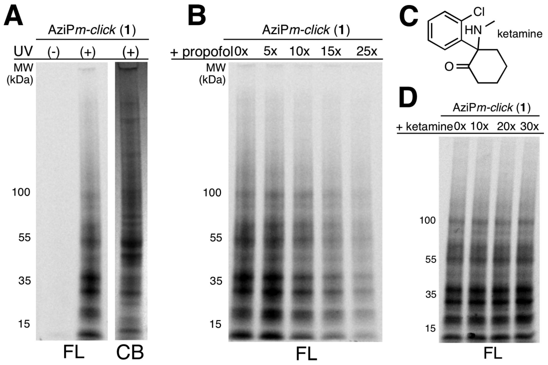

FIGURE 3. **Fluorescent profiling of propofol proteome.** *A*, fluorescent image (*FL*) of SDS-polyacrylamide gel of synaptosomes exposed to AziPm-*click* (**1**) with or without UV irradiation and corresponding Coomassie Blue (*CB*) stain of UV-irradiated synaptosomes. *B*, protection from AziPm-*click* (**1**) labeling of synaptosomes by propofol at 5× (75 μM), 10× (150 μM), 15× (225 μM), and 25× (375 μM). *C*, chemical structure of ketamine. *D*, protection from AziPm-*click* (**1**) labeling of synaptosomes by ketamine at 10× (150 μM), 20× (300 μM), and 30× (450 μM). All experiments were conducted in triplicate.

Physicochemical and Protein-binding Properties—The physicochemical characteristics of propofol and AziP*m-click* (**1**) are summarized in Table 1, and the geometry-optimized structure is shown in Fig. 2*A*. The UV absorption spectrum of AziP*m-click* (**1**) shows a well defined peak between 330 and 400 nm due to the diazirine group (methanol extinction coefficient ($\Sigma_{365\text{ nm}}$) of 580 $\text{M}^{-1}\text{ cm}^{-1}$). Over the course of UV irradiation using a Rayonet RPR-3500 lamp within the aqueous solution, the AziP*m-click* (**1**) diazirine absorbance band decreased intensity indicating photoactivation (Fig. 2*B*). The time-dependent photoreactivity of AziP*m-click* (**1**) in aqueous solution was a single exponential decay with a half-life ($t_{1/2}$) of 25 min (95% CI; 20–33) within a 1-cm path length cuvette and 6 cm from the lamp. To confirm retention of other major molecular recognition features, we compared equilibrium binding affinities of applied alkylphenol general anesthetics with the model protein apoferritin by isothermal calorimetry and 1-aminoanthracene (1-AMA) competition (28, 29). The affinities of alkylphenols for apoferritin have shown to be well correlated with GABA$_A$ receptor potentiation (30–32); results are summarized in Table 2.

Fluorescent Profiling of Alkylphenol-binding Proteins—To confirm the functionality of both the chemically active groups for downstream ABPP, we employed AziP*m-click* (**1**) within mouse synaptosomes using an azide-PEG3-Alexa 488 fluorophore as a reporter tag. The fluorescent labeling of proteins was reliant on UV exposure (Fig. 3*A*). Fluorescent labeling was decreased with increased concentrations of propofol indicating protection of alkylphenol-binding proteins within synaptosomes (Fig. 3*B*). To control for potential "inner filter" of UV light, ketamine was employed as a protecting ligand (Fig. 3*C*), which conferred no changes in fluorescence intensity seen in Fig. 3*D*.

$\alpha_1\beta_2\gamma_{2L}$ GABA$_A$ Receptor Electrophysiology with AziPm-click (1)—AziP*m-click* (**1**) was functionally active on $\alpha_1\beta_2\gamma_{2L}$ GABA$_A$ receptors heterologously expressed in *Xenopus* oocytes. AziP*m-click* (**1**) demonstrated similar positive modulation activity as propofol (Fig. 4, *A* and *B*). The EC$_{50}$ value for propofol-positive modulation (at a GABA EC$_{10}$) in our system was 10 μM (95% CI; 3.3–17). AziP*m-click* (**1**) required a higher concentration for a similar response with an EC$_{50}$ of 49 μM (95% CI; 38–61).

In Vivo Anesthetic Activity and Photoaffinity Labeling—Propofol and AziP*m-click* (**1**) demonstrated similar pharmacological end points within *Xenopus laevis* tadpoles, inducing reversible hypnosis with no observable toxicity summarized in Table 3 and shown in Fig. 4*C*. To indicate photoaffinity labeling of pharmacologically relevant targets, we demonstrated that AziP*m-click* (**1**) produced sustained anesthetic end points (immobility) *in vivo* after UV irradiation (33). *X. laevis* tadpoles were exposed to 12 μM AziP*m-click* (**1**) or 3 μM propofol for 30 min. Tadpoles were then exposed to 10 min of low intensity UV irradiation or were maintained as a 10-min non-UV irradiation control. Similar to our previous reports for *meta*-azipropofol (33), only tadpoles exposed to AziP*m-click* (**1**) and 10-min UV irradiation displayed prolonged immobility after drug washout (Fig. 4, *D* and *E*).

ABPP for Alkylphenol Anesthetics—The ABPP workflow using AziP*m-click* (**1**) with relative quantification is summarized in Fig. 5*A*. Azide-PEG3-biotin was employed as the reporter tag for streptavidin-affinity isolation of photoaffinity labeled protein targets. Tandem mass tag (TMT) isotopic label-

Downloaded from http://www.jbc.org/ at Rutgers University on April 15, 2018

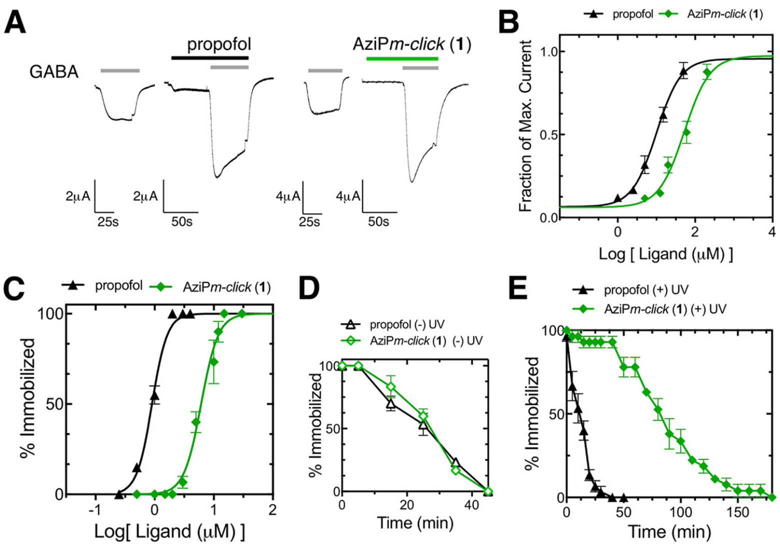

FIGURE 4. **$\alpha_1\beta_2\gamma_{2L}$ GABA$_A$ receptor and anesthetic activity of AziP*m-click* (1).** *A,* representative traces of ligand activity on heterologously expressed $\alpha_1\beta_2\gamma_{2L}$ GABA$_A$ receptors in *X. laevis* oocytes. *Traces* are shown with the oocyte responses to GABA EC$_{10}$ value and corresponding modulation propofol (3 μM) or AziPm-*click* (**1**) (20 μM). *B,* concentration-response curves for propofol (*black circle*) and AziP*m-click* (**1**) (*green diamond*) for the positive modulation of heterologously expressed GABA$_A$ receptor $\alpha_1\beta_2\gamma_{2L}$ in *X. laevis* oocytes. Each point represents the mean of four oocytes ($n = 4$) ± S.E., and data were fitted to a sigmoidal dose-response curve with variable Hill slope. *C,* dose-response curves for propofol ($n = 210$; *black circle*) and AziP*m-click* (**1**) ($n = 300$; *green diamond*) for loss of spontaneous movement in tadpoles. Data were fitted to a sigmoidal dose-response curve with variable Hill slope, and the EC$_{50}$ and Hill slope values are represented in Table 3. *D,* time course of recovery control for *X. laevis* tadpoles following propofol ($n = 30$; *black open circle*) or AziP*m-click* (**1**) ($n = 30$; *green open diamond*) equilibration and 10 min no UV treatment. *E,* time course of recovery for tadpoles following propofol ($n = 30$; *black filled circle*) or AziP*m-click* (**1**) ($n = 30$; *green filled diamond*) equilibration and 10 min of low intensity UV irradiation.

TABLE 3
Tadpole studies

	EC$_{50}$ (95% CI; μm)	Hill slope (mean ± S.E.)
AziP*m-click* (1)	6.1 (5.1–7.4)	3.0 ± 0.54
Propofol	0.90 (0.84–0.97)	3.4 ± 0.31

ing and three-stage mass spectrometry (MS3) (34) were coupled to ABPP for quantitative assessment of capture and propofol protection. The totals for identified proteins are summarized in Fig. 5*B*. The AziP*m-click* (**1**) proteome contained a discernible group of proteins that demonstrated a high degree of capture efficiency with a greater than 10 enrichment factor (Fig. 5*C*). Of the higher capture group, the majority of proteins displayed propofol specificity with a greater than 50% protection and a decrease of at least 5 in enrichment factor (Fig. 5*D* and supplemental Table 1). Five GABA$_A$ receptor subunits ($\alpha_{1,3}$ and β_{1-3}) were identified as propofol-specific proteins. All subunits showed a decrease of at least 10 in enrichment factor with propofol protection. Based on experimental studies in heterologous expression systems, the GABA$_A$ receptor is considered to be an important alkylphenol target. This unbiased ABPP capture of the receptor from a complex biological milieu, derived from native tissue, is to our knowledge the first such demonstration, and it further validates the receptor as a pharmacologically relevant target. To further corroborate the ABPP results of our approach, we examined the apparent subunit-level selectivity binding to this single target with other approaches.

MD Simulations of Dynamic Propofol Interactions with $\alpha_1\beta_3\gamma_2$ GABA$_A$ Receptor—To understand the apparent subunit specificity noted in the above experiments, MD simulations for alkylphenol anesthetic binding were generated with an $\alpha1\beta3\gamma2$ GABA$_A$ model derived from an $\alpha1\beta1\gamma2$ GABA$_A$ model used previously (35). Docking calculations to the entire pentamer identified at least one propofol pose in each subunit interface, $\beta+/\alpha-$ (two sites), $\alpha+/\beta-$, $\alpha+/\gamma-$, and $\gamma+/\beta-$, as shown in Fig. 6*A*. Other than the channel lumen, no alternate sites were consistently detected over multiple docking runs. Docking of AziP*m-click* (**1**) to the same model yielded overlapping sites, demonstrating that AziP*m-click* (**1**) is not sterically hindered from binding to the intersubunit sites, despite the larger molecular size. Furthermore, as shown in Fig. 6, AziP*m-click* docking simulations yield similar orientations to propofol suggesting common favorable interactions.

A receptor-propofol complex was constructed with one propofol molecule in the highest scoring pose for each subunit interface (Fig. 7*A*). The complex was embedded in a fully hydrated phosphatidylcholine membrane and simulated for 270 ns using traditional equilibrium MD with atomic resolution. In addition to allowing the propofol in the intersubunit space to equilibrate before the affinity calculations, we used this simulation to characterize and compare the microscopic interactions between propofol and the binding pocket across subunits.

At the conclusion of the traditional MD simulation, standard binding affinities for propofol in each of the four distinct sites were calculated using separate 24-ns AFEP simulations. The

Downloaded from http://www.jbc.org/ at Rutgers University on April 15, 2018

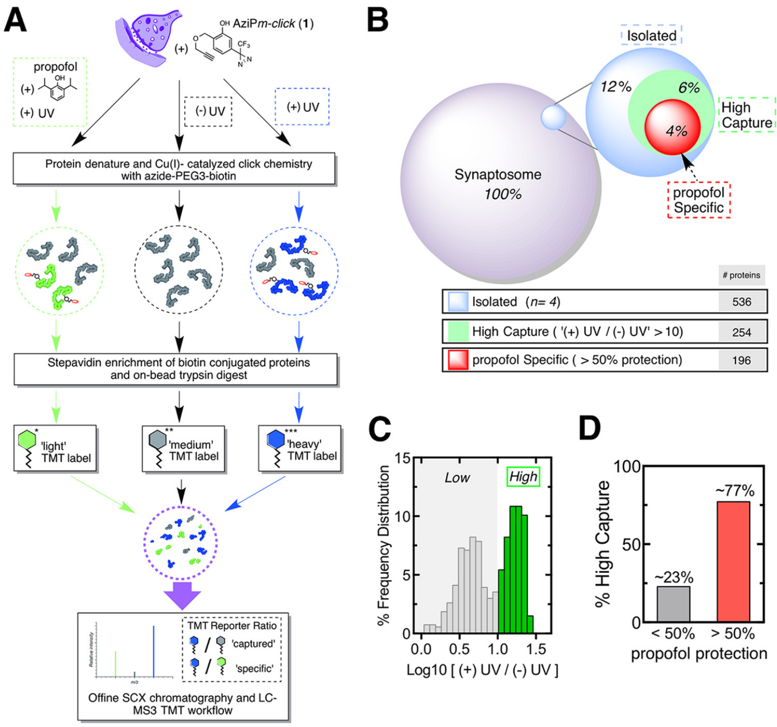

FIGURE 5. **Affinity-based propofol profiling of alkylphenol-binding proteins in native synaptosomes.** *A*, scheme for capture and analysis of AziP*m-click* (**1**) labeling profiles in synaptosomes by biotin-streptavidin methods, TMT, labeling for relative quantification, strong cation exchange chromatography (*SCX*), and Nanoliquid chromatography-three-stage mass spectrometry (NanoLC-MS3) analysis. *B*, distribution of protein groups for the AziP*m-click* (**1**) capture and approximate percentage of full synaptosomal proteome, with a summary of the group's threshold requirements. Proteomic experiments were conducted in quadruplicate; the log2 standard deviation between datasets was calculated as 0.28 for heavy over intermediate TMT-labeled samples and 0.17 for heavy over light TMT-labeled samples. *C*, TMT ratio frequency distribution (log10 scale) of UV *versus* no UV irradiation with high capture efficiency threshold. *D*, percent of high capture group proteins that demonstrated less than or greater than 50% protection by propofol.

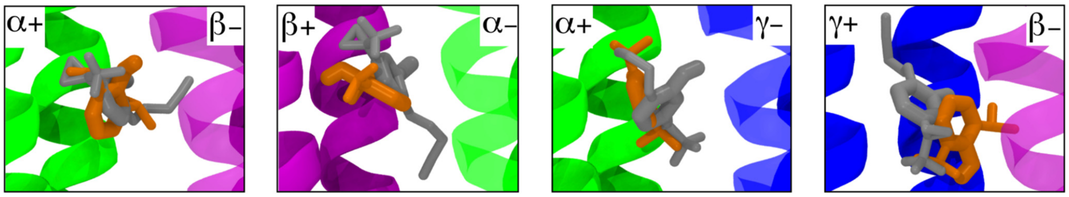

FIGURE 6. **Intersubunit propofol and AziP*m-click* (1) occupancy in an $\alpha_1\beta_3\gamma_2$ GABA$_A$ receptor as predicted by AutoDock Vina simulations.** Helices of the four distinct subunit interface pairs (α_1, *green*; β_3, *magenta*; γ_2, *blue*) with the highest scored docking poses for propofol (*orange*) and AziP*m-click* (**1**) (*gray*).

AFEP method also involves running MD simulations but is designed to facilitate simultaneous calculation of average quantities appearing in the Zwanzig equation (36), an exact expression for the free energy difference between two states (*e.g.* bound and unbound) that inherently accounts for all entropic and enthalpic contributions. The results from the AFEP simulations indicate three higher affinity sites at the $\alpha+/\beta-$ and two $\beta+/\alpha-$ interfaces, with K_D values similar to propofol EC$_{50}$. K_D values for the $\alpha+/\gamma-$ and $+\gamma/\beta-$ interfaces, however, suggest markedly weaker propofol binding to those sites (Table 4).

The particularly low affinity of propofol for the $+\gamma/\beta-$ interfacial cavity, which has one more polar residue than the other interfacial cavities (Fig. 8*A*), seemed potentially contradictory to an essential role for hydrogen bonding. As shown in Fig. 7*B*, however, the pK_D values for different subunit interfaces were found to be strongly correlated ($r^2 = 0.94$) with the probability (P_{hb}) that the propofol hydroxyl would form at least one hydrogen bond with one of the cavity-lining residues. Propofol in either of the two sites with low K_D values ($\alpha+/\beta-$ and $\beta+/\alpha-$) had at least $P_{hb} > 0.8$; for the two low affinity sites, this probability was significantly reduced ($P_{hb} < 0.3$). Thus, although propofol affinity is correlated with propofol hydrogen bonding, propofol is less likely to form hydrogen bonds with the more hydrophilic $+\gamma/\beta-$ interfacial cavity. This result was due to stable hydration of the $+\gamma/\beta-$ cavity, due to interactions of water molecules with γSer-301 and γThr-

Downloaded from http://www.jbc.org/ at Rutgers University on April 15, 2018

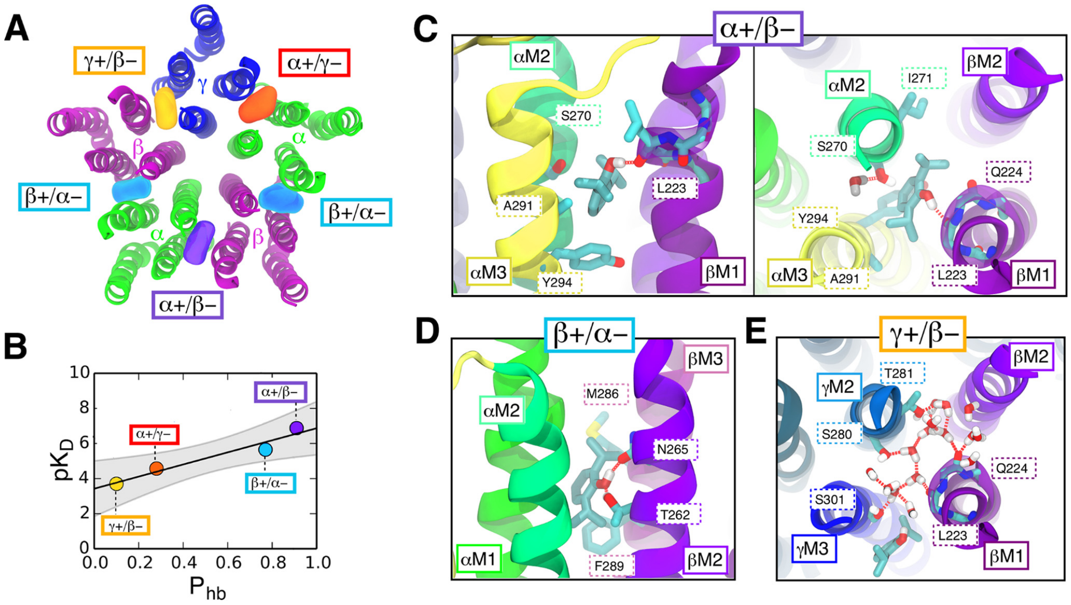

FIGURE 7. **Selectivity of intersubunit propofol binding in an $\alpha_1\beta_3\gamma_2$ GABA$_A$ receptor as predicted by molecular dynamics simulations using the AFEP algorithm.** *A,* five propofol molecules (colored surfaces) docked in the GABA$_A$ receptor subunit interfaces (β+/α− (−2 sites)) are as follows: *cyan,* α+/β−; *violet,* α+/γ−; *red,* γ+/β−, *orange.* The transmembrane domain is viewed from the extracellular side along the pore axis and colored by subunit type; α_1, *green;* β_3, *magenta;* and γ_2, *blue. B,* computational results for propofol pK_D and its likelihood of hydrogen bonding to protein cavity residues (P_{hb}) can be well fit by the line p$K_D = a\,(P_{hb}) + b$, where $a = 3.4 \pm 0.8$ and $b = 3.4 \pm 0.1$, and the 95% confidence band is shown in *gray. C–E,* interactions of propofol and water in the high affinity and low affinity interfacial sites. Hydrogen bonds, *red dashed lines. C,* propofol binding in α+/β− interface that contained seven polar residue side chains (*left,* side view; *right, top view*) forms a persistent hydrogen bonding with a backbone carbonyl group exposed by the M1 helical bulge (βLeu-223). *D,* bound propofol at the β+/α− interfacial site, which contained seven polar residue side chains, (side view) alternates between hydrogen bonds to β+M2:Thr-262 and β+M2:Asn-265. For compactness, the image shows a rare frame in which both hydrogen bonds coexist. *E,* in the γ+/β− interface eight polar residue side chains were present (*top view*); these residues favor hydrogen bonding with a water cluster stabilized by polar residues γ+Thr-281 and γ+Ser-301, which are homologous to hydrophobic residues in α and β subunits (see Fig. 7).

TABLE 4

Binding affinities of propofol bound to one of four GABA$_A$ receptor interfacial sites (shown in Fig. 5, interfaces notated counter-clockwise), calculated using AFEP

Interface	K_D	$K_D\,e^{-\delta/RT} - K_D\,e^{\delta/RT}$ [a]
	μM	μM
α+/β−	0.1	0.02–0.7
β+/α−	2.0	0.4–10
α+/γ−	30	5–200
γ+/β−	200	40–1000

[a] K_D range corresponds to an uncertainty in Δ*G* of δ = 1 kcal/mol. Challenges inherent in determining constants required for correction to laboratory conditions contribute significantly to δ; errors in relative values of K_D are substantially reduced compared with those for absolute K_D.

281 (Fig. 7*E*). The water molecules compete for hydrogen bonding partners and interact unfavorably with the propofol isopropyl groups.

Within the highest affinity site at the α+/β− interface, propofol orients as a hydrogen donor to the carbonyl backbone of Leu-223 within the βM1 transmembrane helix (Fig. 7*C*) where a bulge in backbone hydrogen bonding is observed in crystal structures for both GluCl (37) and the GABA$_A$ receptor β_3 homopentamer (38). Similar behavior was observed in simulations of triiodothyronine bound to interfacial sites (39). In the β+/α− interface, propofol alternates rapidly between serving as a hydrogen acceptor for βM2:Thr-262 and donor for βM2:Asn-265 (Fig. 7*D*). The associated slight reduction in pK_D is consistent with the slight reduction in P_{hb} and the line of best fit.

The AFEP calculations yield an intermediate affinity of propofol for the γ−/α+ interfacial site. Residues of the γ-face, however, are nearly identical to those of the β-face, as shown in Fig. 8, *B* and *C*, and sequence differences among site residues are unable to account for the moderate differences in hydrogen bonding and affinity between γ−/α+ and the higher affinity β−/α+ site. Because hydrogen bonding of propofol to the M1 backbone is frequently observed for β− but not γ−, it is possible that sensitivity of fluctuations in M1 secondary structure to non-cavity residues causes the observed weak sequence dependence. If so, the result suggests a further uncertainty in interpretations of mutagenesis experiments and the underlying assumption that identified residues are contact residues.

Propofol and 2-Fluoro-1,3-diisopropylbenzene (Fropofol) Protection of GABA$_A$ Receptor Subunits—To experimentally evaluate the role of the alkylphenol hydroxyl in selective binding to sites within synaptic GABA$_A$ receptor subunits, we applied the fluorine-substituted analogue fropofol (Fig. 9*A*) within protection experiments (40). Previously, fropofol did not modulate or disrupt propofol potentiation of the GABA$_A$ receptor, and it did not cause immobilization at even 100-fold higher concentrations than propofol. In contrast, fropofol did display similar binding as propofol to protein sites that were not dependent on

Downloaded from http://www.jbc.org/ at Rutgers University on April 15, 2018

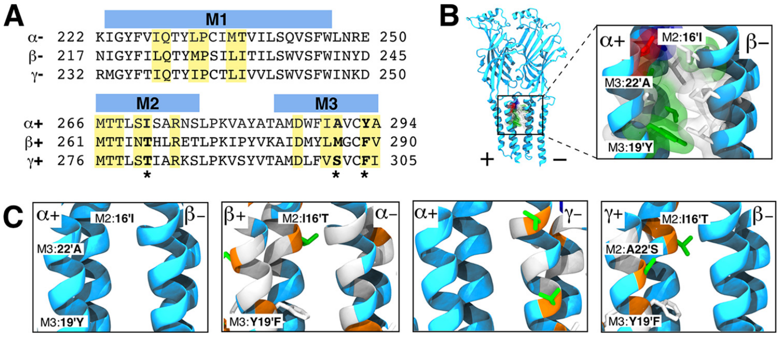
A
M1
α- 222 KIGYFVIQTYLPCIMTVILSQVSFWLNRE 250
β- 217 NIGYFILQTYMPSILITILSWVSFWINYD 245
γ- 232 RMGYFTIQTYIPCTLIVVLSWVSFWINKD 250
M2
M3
α+ 266 MTTLSISARNSLPKVAYATAMDWFIAVCYA 294
β+ 261 MTTINTHLRETLPKIPYVKAIDMYLMGCFV 290
γ+ 276 MTTLSTIARKSLPKVSYVTAMDLFVSVCFI 305
*
*
*
B
α+
β−
M2:16'I
M3:22'A
M3:19'Y
+
−
C
α+
β−
M2:16'I
M3:22'A
M3:19'Y
β+
α−
M2:I16'T
M3:Y19'F
α+
γ−
γ+
β−
M2:I16'T
M2:A22'S
M3:Y19'F

FIGURE 8. **Sequence variation in interfacial binding sites of an $\alpha_1\beta_3\gamma_2$ GABA$_A$ receptor heteropentamer.** *A,* sequence alignment of + and − subunit interfaces that contribute to the formation of interfacial binding sites. Highlighted residues represent residue side chains that directly contribute to the formation of the binding cavity. *Bold* and * residues denote key sequence variations in the interfacial binding sites. *B* and *C,* helices of the four distinct subunit interface pairs with $\alpha+/\beta-$ interface as the reference pair. In all panels, side chains are colored by residue type as follows: polar (*green*), hydrophobic (*white*), acidic (*red*), and basic (*blue*). *B,* extended view and binding site cavity view of the $\alpha+/\beta-$ interface reference pair with all cavity contributing side chain residues represented. *C,* helices of the four distinct subunit interface pairs are colored according to sequence differences with the $\alpha+/\beta-$ interface as the reference subunit pair displaying identical (*light blue*), similar (*white*), and change in residue type (*orange*). Note that for a given interface, coloring of the + and − subunit backbone reflects sequence differences from α_1 and β_3, respectively. Cavity residues are labeled according to a prime-numbering system in which M2:16′ is equivalent to Ile-271, Thr-266, and Thr-281 for $\alpha1$, β_3, and γ_2 subunits, respectively; M3:19′ is Tyr-294, Phe-289, and Phe-304 and M3:22′ is Ala-291, Met-286, and Ser-301 with the same ordering.

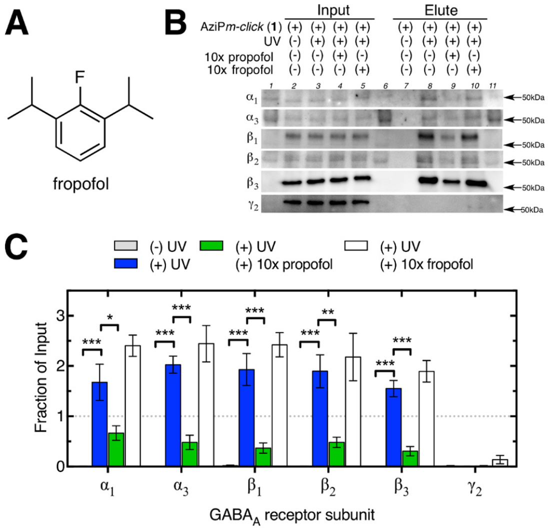

FIGURE 9. **Ligand protection of synaptic GABA$_A$ receptor capture.** *A,* chemical structure of fropofol. *B,* representative Western blots for GABA$_A$ receptor subunits of input (*lanes 2–5*) and the corresponding elution (*lanes 7–10*) for synaptosomal samples exposed to AziP*m-click* (**1**) (10 μM) with or without UV irradiation and with or without co-exposure with propofol (100 μM) or fropofol (100 μM). *Lanes 1, 6,* and *11* contain protein ladders. *B,* comparison of non-UV and UV capture with or without propofol or fropofol protection for each GABA$_A$ receptor subunit; values are represented as the mean of four experiments ± S.E. of the fraction of the corresponding input sample. Data were analyzed by two-way analysis of variance with Tukey's multiple comparison test comparing fraction captured between protection conditions for each subunit. Significant differences compared with UV-irradiated eluate preparation without protection ligand are shown (***, $p < 0.001$; **, $p < 0.01$; *, $p < 0.05$).

hydrogen bond interactions (40). Azide-PEG3-biotin was employed as the reporter tag for streptavidin-affinity isolation of protein targets photoaffinity labeled by AziP*m-click* (**1**) with or without protection ligands propofol or fropofol. Protein levels of GABA$_A$ receptor subunits were determined by Western blotting before (or "input") and after (or "elute") streptavidin capture of biotinylated proteins. All GABA$_A$ receptor subunits were detected within synaptosomes prior to capture (Fig. 9*A*), consistent with synaptic localization of these subunits. After capture, only α and β subunits were detected. All GABA$_A$ receptor α and β subunits showed significant decreases in capture efficiency when propofol was present during UV irradiation. Unlike propofol, fropofol was unable to protect GABA$_A$ receptor α and β subunits from capture (Fig. 9, *A* and *B*).

Discussion

In this study we investigated the molecular mechanisms and placement of alkylphenol anesthetic binding to synaptic GABA$_A$ receptors. This multifaceted study integrated an assessment of total synaptic GABA$_A$ receptor binding relative to the native proteome with a targeted investigation of key molecular recognition elements that contribute to binding affinity. Our approach deployed a novel anesthetic PAL containing a click chemistry moiety for downstream quantitative ABPP, as well as AFEP MD simulations of receptor binding and photoaffinity protection experiments. Together, these studies add to the understanding of propofol pharmacology and the dynamic behaviors of heteropentameric receptors.

Previous work has shown that the ligand-gated receptors, GABA$_A$ receptors in particular, are modulated by propofol. Site-directed mutagenesis within heterologous expression systems and animal models provides the advantage of demonstrating drug activity and pharmacological changes as well as candidate regions of drug binding. The recognized pitfalls of mutagenesis, like the inherent ambiguity of defined interaction regions, perturbation of native protein dynamics and/or genetic compensation, mandates that additional strategies be deployed to complement these investigations. Photoaffinity labeling has been one method used to further the understanding of anesthetic-binding sites (41). Multiple PALs for propofol have been reported (42, 43), including one from our own labo-

Downloaded from http://www.jbc.org/ at Rutgers University on April 15, 2018

ratory (29), and have furthered an understanding of propofol-protein interactions. Previous photoaffinity labeling studies, however, have had their own recognized limitations, particularly reliance on heterologous overexpression and reconstituted systems.

GABA$_A$ Receptor Binding of Alkylphenol-based Anesthetics within the Synaptic Proteome—To respond to these issues, we developed a photoaffinity tandem bioorthogonal ligand, AziP*m-click* (**1**) to evaluate the alkylphenol-based anesthetic-binding proteins within the native synaptosomal proteome using ABPP. Subunits of the GABA$_A$ receptor were identified as AziP*m-click* (**1**)-binding proteins that were shared with propofol. To our knowledge the ABPP strategy has provided the first evidence of direct interaction of alkylphenol anesthetics with native tissue-derived synaptic GABA$_A$ receptors.

We observed that only selected subunits (α and β) within the heteropentameric receptor were identified as AziP*m-click* (**1**)-binding proteins. No γ subunits were captured in the ABPP experiment despite the fact that the γ_2 subunit is estimated to incorporate within 75–80% of all receptor complexes (1), act as an important subunit for synaptic GABA$_A$ receptor eventual translocation to the plasma membrane (8, 45–47), and was easily identified within our input synaptic milieu. Because AziP*m-click* (**1**) demonstrated hypnotic activity and the ability to act as a positive modulator of the GABA$_A$ receptor, the evidence indicates that the orientation(s) of AziP*m-click* (**1**) within the active binding site(s) has the diazirine photoreactive group in close proximity *only* to α and β subunits. The γ_2 subunit apparently does not contribute surface area to an alkylphenol-binding site at the concentrations used here. When combined with previous work implicating interfacial regions within Cys-loop receptors (22, 48, 49) as propofol-binding sites, we more specifically conclude that alkylphenol occupancy of α and β subunit interfacial sites (*e.g.* $\beta+/\alpha-$ and $\alpha+/\beta-$) is *sufficient* to result in positive modulation.

Asymmetrical Propofol Binding to the GABA$_A$ Receptor—To evaluate this hypothesis and determine potential elements that mediate propofol affinity, we employed independent MD simulations using rigorous AFEP calculations that focused on propofol interactions within the $\alpha_1\beta_3\gamma_2$ GABA$_A$ receptor. Beginning with high scoring poses in the five potential transmembrane sites consistently identified by docking to the full pentamer (all of which are at the subunit interfaces), AFEP calculations yielded K_D values at $\beta+/\alpha-$ and $\alpha+/\beta-$ interfaces that were similar to experimental propofol EC$_{50}$ values. In contrast, the K_D values for $\alpha+/\gamma-$ and $\gamma+/\beta-$ interfaces were 1–2 orders of magnitude greater, reaching concentrations of propofol known to be lethal and shown to inhibit the induced positive modulation in electrophysiology studies (50, 51). MD simulations have demonstrated that partial (or asymmetrical) occupancy of the interfacial regions, even in a homomeric pentameric ligand-gated ion channel, has greater effects on pore radius than total (or symmetrical) occupancy (52). Recently, a similar hypothesis was suggested for etomidate and propofol using site-directed mutagenesis of $\alpha_1\beta_2\gamma_2$ GABA$_A$ receptor (48). It is also likely that at propofol concentrations where the lowest affinity interfacial sites are occupied, other sites that cause loss of function (*e.g.* pore blocking site(s)) may be occupied as well.

Hydrogen Bonding Mediates Alkylphenol-based Anesthetic Binding to the GABA$_A$ Receptor—Numerous interactions can contribute to propofol affinity within a protein cavity. These include multiple weak interactions, such as the hydrophobic effect, as well as the potential for stronger interactions, such as hydrogen bonding with the alkylphenol hydroxyl. From the $\alpha_1\beta_3\gamma_2$ GABA$_A$ receptor MD simulations, the higher relative affinities for the $\beta+/\alpha-$ and $\alpha+/\beta-$ interfaces corresponded with increased probability for hydrogen bond interaction(s) for $\beta+$M2 Thr-262 and Asn-265 or β-M1 Leu-223 at a conserved bulge in the M1 backbone. In contrast, the lowest affinity ($\gamma+/\beta-$) interface contains a larger number of potential hydrogen bonding side chains; however, this increases cavity hydration and causes displacement of propofol. Propofol bound to the $\alpha+/\gamma-$ sites yielded an intermediate affinity and likelihood of hydrogen bonding. Although the $\alpha+/\gamma-$ side chains are equivalent to those of the higher affinity $\alpha+/\beta-$ site, we observed that the backbone carbonyl of $\beta-$ M1 Leu-223 was significantly more likely to serve as a hydrogen bond acceptor than in the homologous residue, $\gamma-$ M1 Ile-238. The origin of this difference is likely subtle and dependent on any residues that affect M1 secondary structure, not just cavity residues.

To confirm the contribution of the hydroxyl to the alkylphenol-based anesthetic-binding site within captured synaptic GABA$_A$ receptor subunits and the functional relevance of these sites, we introduced the fluorine-substituted and therefore hydrogen bond-null ligand fropofol into our investigation. With the fluorine replacement of the alkylphenol hydroxyl, fropofol displayed no activity on heterologously expressed $\alpha_1\beta_2\gamma_2$ GABA$_A$ receptors (40). Fropofol does, however, bind to propofol-binding sites that are characterized primarily by the hydrophobic effect (40). We observed that fropofol, unlike propofol, did not protect the α or β subunits from AziP*m-click* (**1**) capture. These results confirm MD simulations that identified hydrogen bonding as a key element contributing to alkylphenol-based anesthetic binding to synaptic GABA$_A$ receptors and that such interfacial sites are likely to contribute to the altered functional activity.

Study Limitations—Although the goal of this investigation was to reconcile propofol pharmacology with a complex binding proteome, some limitations are implicit in our studies, including points for future improvement. First, our analogue AziP*m-click* (**1**) showed a reduced potency for modulating $\alpha_1\beta_2\gamma_2$ GABA$_A$ receptors and a parallel decrease in anesthetic potency as compared with the parent propofol. However, this is well within what has been reported for the alkylphenol chemotype (53), and it is probably a result of the additional bulk and electrostatically active diazirine and ether/alkyne groups, which reduce hydrophobicity. Furthermore, associated docking simulations demonstrated overlapping poses for propofol and AziP*m-click* (**1**). Finally, MD simulations using the AFEP algorithm use the parent compound propofol rather than AziP*m-click* (**1**), but they yield affinities that are consistent with results from AziP*m-click* (**1**).

Second, our current investigation is limited to the employed biological system, a synaptosomal fraction derived from whole brain, and therefore, it is focused on synaptic proteins, including synaptic GABA$_A$ receptors. Propofol has previously been

Downloaded from http://www.jbc.org/ at Rutgers University on April 15, 2018

shown to influence tonic receptor-mediated inhibition that is anticipated to contribute to observed hypnotic sedation and other anesthesia phenotypes, specifically amnesia (13, 14, 54). Because of the lack of extrasynaptic $GABA_A$ receptor subunits within our proteome (data not shown), we could not determine the binding character for these receptors.

Finally, although the presented quantitative ABPP strategy allows the first platform for identifying alkylphenol protein targets relative to a native biological milieu, it does not directly identify the photoaffinity labeled residues. In part, this is a result of the challenging elution/digestion of labeled proteins and large modification size (>600 Da) of the biotin PEG3-conjugated AziP*m-click* (**1**) modification. Currently available cleavable biotin-*X*-azide linkers have variable cleavage efficiency and/or require reagents that perturb downstream quantitative labeling for native tissue-derived systems (55). Our efforts for non-quantifiable capture using cleaved biotin linker and AziP*m-click* (**1**) identified modifications on higher abundance proteins like the voltage-dependent cation channel (data not shown) that corresponded with earlier reports (56); however, residue-level modifications on lower abundance proteins, like the $GABA_A$ receptor, remained undetected. Thus, we cannot confirm an interfacial location of sites in this study, although this location has been demonstrated in heterologous receptors (19). Future development of chemically active alkylphenol anesthetics, cleavable biotin linkers, as well as enhanced peptide enrichment and release methods may allow for increased capture efficiency permitting detection of modifications within the very low abundance photoaffinity labeled peptides.

Additional Alkylphenol-based Anesthetic Synaptic Targets—It is unlikely that a given drug will only bind and act on a single protein target within a proteome. In particular, the small general anesthetic molecules have been shown to bind to many different proteins (57). Although propofol is thought to have higher affinity for specific protein targets relative to volatile anesthetics, the projected affinities for major targets, as we observed with the $GABA_A$ receptor, still remain in the low micromolar range. Therefore, it is not surprising that a number of targets (~200) were captured due to the promiscuous binding associated with the general anesthetic. Whether the activity of every identified protein is altered upon alkylphenol binding is not clear and is not likely. However, some captured targets, in addition to the $GABA_A$ receptor, have been reported as being influenced by propofol. Examples include syntaxin-1A (58), *N*-methyl-D-aspartate receptor (59), potassium/sodium hyperpolarization-activated cyclic nucleotide-gated channel 1 (60), as well as voltage-gated calcium channels (61) and potassium channels (62), all of which may contribute to desirable and/or undesirable pharmacological effects.

Concluding Remarks—Although the $GABA_A$ receptor is considered to be an important target for general anesthetics, the mechanism of $GABA_A$ receptor modulation remains unclear. In this investigation, we aimed to further understand alkylphenol binding to native receptors and to evaluate the molecular recognition elements that mediate affinity. Our results indicate that propofol binds to the assembled receptor in an asymmetric pattern, with greater affinity for $\beta+/\alpha-$ and $\alpha+/\beta-$ interfaces. Hydrogen bonding and cavity hydration were found to be the likely defining factors that contribute to the differential interfacial affinity and functional activity. In addition, this work suggests that the alkylphenol anesthetic proteome is large and complex, providing the opportunity to modulate activity at many targets. Finally, this work adds to current methodologies used for the identification of anesthetic targets and a better understanding of allosteric binding interactions.

Experimental Procedures

General Synthetic Procedures—Reagents and solvents were all used as acquired from commercial sources. ^1H, ^{13}C, and ^{19}F NMR spectra were obtained on either a Bruker DMX 500 MHz or a Bruker DMX 360 MHz nuclear magnetic resonance spectrometer. The detailed synthetic methodology and associated NMR spectra for intermediates and AziP*m-click* (**1**) are provided in the supplemental material. Purity of AziP*m-click* (**1**) was determined using reverse phase-HPLC with a C-18 analytical column with a 60-min gradient from 40 to 70% acetonitrile in 0.1% formic acid at a 1 ml/min flow at ambient temperature (21–22 °C). AziP*m-click* (**1**) was monitored for UV-visible absorbance at 210 and 365 nm. The retention time for AziP*m-click* (**1**) was observed at 22.3 min with a purity of >96%.

Physicochemical Properties—The UV spectrum and extinction coefficient of the AziP*m-click* (**1**) diazirine absorption were obtained from known concentrations in methanolic solutions and gathered from the Varian Cary 300 Bio UV-visible spectrophotometer. Photoactivation of the diazirine was measured by the disappearance of the diazirine UV absorption peaks when exposed to 350 nm light (Rayonet RPR-3500 lamp) ~6 cm from the light source. Maximum water solubility was approximated using the extinction coefficient. Calculated octanol/water partition coefficients were generated using XLOGP3 software 22 with default settings. The geometry-optimized structures for AziPm-*click*(**1**) was calculated at the B3LYP/6–311+G (2*d*,*p*) level of theory using Gaussian 09 (63).

Isothermal Titration Calorimetry—Isothermal titration calorimetry isotherms for binding to soluble protein model horse spleen apoferritin were conducted as reported previously (31) and were resolved using a VP-isothermal titration calorimetry microcalorimeter (MicroCal, Inc., Northampton, MA). Origin 5.0 software was used to best-fit thermodynamic parameters to the heat profiles.

1-AMA Displacement Fluorescence Assay—1-AMA fluorescence inhibition has been reported as a reliable measurement of anesthetic occupation of the horse spleen apoferritin anesthetic site (64). 1-AMA displacement studies were conducted as described previously (29). The fluorescence intensity *versus* concentration data were fitted to variable slope Hill models to obtain the IC_{50} and Hill slope. The K_D value was calculated using the Cheng-Prusoff equation to correct for the presence of the 1-AMA competitors.

Crude Synaptosome Preparation—Mouse crude synaptosomes were prepared as reported previously (65) with modifications. Male C57/B6 mice (8–12 weeks) were deeply anesthetized with isoflurane and intracardially perfused with ice-cold phosphate-buffered saline (PBS; pH 7.4) before decapitation. Brains were extracted and homogenized in ice-cold isolation buffer (IB; 0.32 M sucrose, 2.5 mM HEPES, 1 mM EDTA (pH 7.4))

Downloaded from http://www.jbc.org/ at Rutgers University on April 15, 2018

(10% w/v%) in the presence of protease and phosphatase inhibitors. The homogenate was centrifuged at 1,000 × *g* for 10 min at 4 °C. The resulting supernatant was decanted, and the pellet was homogenized with an equal volume of IB and centrifuged at 1,000 × *g* for 10 min at 4 °C. Both supernatants were pooled and were centrifuged at 1,000 × *g* for 10 min at 4 °C. The supernatant was decanted and centrifuged at 12,000 × *g* for 20 min at 4 °C. The pellet was washed twice by resuspension of the pellet in 2× volumes of IB and centrifuged at 12,000 × *g* for 15 min at 4 °C. The resulting crude preparation of synaptosomes, now entirely free of the euthanizing isoflurane, was used in following experiments. All following protein contents are measured using BCA assay (Thermo Scientific). Animal care and experimental procedures involving mice were carried out according to a protocol approved by the IACUC of the University of Pennsylvania.

Synaptosomal Photoaffinity Labeling—Synaptosomes were resuspended to 1 mg of protein/ml in HEPES buffer medium (in mM: 140 NaCl, 5 KCl, 5 $NaHCO_3$, 1.2 NaH_2PO_4, 1 $MgCl_2$, 10 glucose, and 10 HEPES (pH 7.4)). Concentrations of AziP*m-click* (**1**) with or without the presence of concentrations of competitive ligands (propofol, ketamine, or fropofol) in dimethyl sulfoxide (DMSO) vehicle (<0.3% v/v) were added, and synaptosomes were gently vortexed for 10 s. The samples were allowed to equilibrate for 5 min before being transferred to a parafilm-sealed 1-mm path length quartz cuvette. The sample was then irradiated for 20 min at a peak bandwidth of 350 nm (Rayonet RPR-3500 lamp) ~6 cm from the light source. Non-irradiated samples were left in the dark at ambient temperature (22–25 °C) for 20 min. All remaining procedures were conducted with restricted light exposure.

Fluorophore Conjugation for Proteome Detection—To 150 μg of photolabeled or control synaptosomes, 8 μl of 10% SDS in water and 2 μl of 1 mM dithiothreitol (DTT) in water were added. Samples were vortexed and heated at 65 °C for 10 min. After a brief cooling, final concentrations of 30 μM azide-PEG3-Fluor 488 (Click Chemistry Tools), 2 mM tris(3-hydroxypropyltriazolylmethyl)amine (Sigma), 1 mM ascorbic acid (Sigma), and 1 mM $CuSO_4{\cdot}5H_2O$ (Sigma) were added to each sample and vortexed vigorously. The samples were left in the dark for 1 h. After, 4× volume of chilled methanol, 1.5× of chilled chloroform, and 3× of chilled double distilled H_2O were added and vortexed vigorously. Samples were centrifuged at 1,300 × *g* for 30 min, and both liquid layers were carefully removed. The protein pellet was washed with 500 μl of 1:1 (v/v) methanol/chloroform and centrifuged at 14,000 × *g* for 20 min at 4 °C. Washed pellets were air-dried for 10 min and resuspended in 25 μl of 1% SDS and 1% Triton X-100 in 50 mM Tris base buffer. An equal volume of 2× SDS Laemmli buffer was added, and 25 μg of protein was loaded without boiling to 4–15% SDS-polyacrylamide gel. Proteins were directly visualized within the gel using fluorescence and then stained with Coomassie G-250 stain. Fluorescent studies were normalized to Coomassie stain band intensity.

Heterologous Expression of GABA$_A$ Receptor Subunits and Electrophysiological Recordings—GABA$_A$ receptor expression in *X. laevis* oocytes was completed as described previously (40). cDNAs for GABA$_A$ receptor α_1, β_2, and γ_{2L} subunits were generously provided by Dr. Robert Pearce (University of Wisconsin). All animal care and experimental procedures involving *X. laevis* frogs were carried out according to a protocol approved by the IACUC of Thomas Jefferson University. GABA$_A$ receptor currents expressed in *X. laevis* oocytes were recorded as reported previously (40). Data acquisition and initial analysis were performed using pClamp 9.2/10.3 (Molecular Devices, Sunnyvale, CA). Macroscopic currents were low-pass filtered at 1 kHz and digitized at 2 kHz. Data were fit to a sigmoidal dose-response curve with variable Hill slope.

Hypnotic Activity and in Vivo Photolabeling in X. laevis Tadpoles—Behavioral activity was initially determined in albino *X. laevis* tadpoles (stages 45–47) as described previously (29, 33). All animal care and experimental procedures involving *X. laevis* tadpoles were carried out according to a protocol approved by the IACUC of the University of Pennsylvania.

Biotin Conjugation—To 750 μg of photolabeled or control synaptosome samples, 40 μl of 10% SDS and 2 μl of 5 mM DTT in water were added. Samples were then vortexed, heated for 10 min at 65 °C, and then briefly cooled. Final concentrations of 150 μM azide-biotin (Click Chemistry Tools), 2 mM tris(3-hydroxypropyltriazolylmethyl)amine (Sigma), 1 mM ascorbic acid (Sigma), and 1 mM $CuSO_4{\cdot}5H_2O$ (Sigma) were added to each sample and vortexed vigorously. The samples were left in the dark at ambient temperature (22–25 °C) for 1 h with mild agitation. Directly to each sample 4× volume chilled methanol, 1.5× chilled chloroform, and 3× chilled double distilled H_2O were added. Samples were vortexed vigorously and centrifuged at 1,400 × *g* for 30 min at 4 °C. Both liquid layers were carefully removed, and the protein pellet was washed with 2 ml of 1:1 (v/v) chilled methanol/chloroform. Samples were centrifuged at 3,500 × *g* for 30 min at 4 °C. Protein pellets were briefly air-dried before further processing.

Sample Processing for ABPP Mass Spectrometry Studies—750 μg of biotin-conjugated protein sample was resuspended in 500 μl of 25 mM NH_4HCO_3 and 6 M urea in water. Next, 150 μl of 5% Triton X-100 in water, 50 μl of 10% SDS in water, and 1.5 μl of 0.5 M DTT were added. The samples were heated for 15 min at 65 °C. After briefly cooling, 14 μl of 0.5 M iodoacetamide in water was added, and the sample was left in the dark for 45 min. Insoluble debris was separated by centrifugation for 10 min at 14,000 × *g*. The supernatant was diluted to 4 ml with PBS, and 2 ml of PBS containing 100 μl of 50% streptavidin-agarose resin (Thermo Scientific) was added. Biotinylated proteins within the sample were captured over resin overnight at 4 °C with mild agitation. The resin was first washed with 6 ml of 1% SDS in PBS, and then 7 ml of 0.1 M urea in PBS followed by 10 ml of PBS. The resin underwent a final wash with 0.9 ml of 50 mM Tris-HCl and 1 mM $CaCl_2$ in water (pH 8.0) and then resuspended in 200 μl of 50 mM Tris-HCl, 1 mM $CaCl_2$ in water (pH 8.0), and 2 μg of porcine sequencing grade trypsin (Promega). Samples were digested overnight at 37 °C. Samples were then centrifuged at 2,000 × *g* for 4 min, and digest supernatant was decanted. Beads were washed in 100 μl of PBS centrifuged at 5,200 × *g* for 5 min, and the wash was combined with the digest supernatant. To the combined sample, trifluoroacetic acid (TFA) was added to 0.4% (v/v) or until pH <2. The sample was desalted with Oasis C18 10-mg columns (Waters) as described previously (66). The eluted sample was dried by speed vac and resuspended in 0.1 M HEPES buffer (pH 8.5). Samples were

Downloaded from http://www.jbc.org/ at Rutgers University on April 15, 2018

labeled with Tandem Mass Tag™ 6-plex (TMTsixplex™) (Thermo Scientific) with the UV(+) sample labeled with TMT^6- 128 or 131 reagent, the propofol protection sample labeled with TMT^6- 126 or 129 reagent, and the UV(−) sample labeled with TMT^6- 127 or 130 reagent using product instructions. Appropriate corresponding TMTsixplex™-labeled samples were pooled and dried by speed vac. The combined samples were resuspended in 0.5% acetic acid in water and pH-corrected with acetic acid until pH was <2. 40 μg of protein was desalted with C18 stage tips prepared in-house and dried by speed vac.

Samples were resuspended in 10 mM KH_2PO_4 (pH 2.6), 30% acetonitrile (v/v) in water, and fractionated by off-line strong cation exchange chromatography prior to mass spectrometry (MS) analysis similar to as reported previously (66). The full synaptosome proteome control was prepared similarly without TMTsixplex™ labeling.

Mass Spectrometry Analysis—All TMT samples were analyzed with three-stage mass spectrometry (MS3) TMTsixplex™ quantification workflow as described previously (34). Spectral analysis was conducted using Thermo Proteome Discoverer 2.0 (Thermo Scientific) and mouse non-redundant (gene-centric) FASTA database. Mascot searches allowed for variable oxidation of methionine (+15.9949 *m/z*) and static modifications of cysteine residues (+57.0215 *m/z*; iodoacetamide alkylation) and TMTsixplex™ tags on lysine residues and peptide N termini (+229.162932 *m/z*). To establish the base synaptosomal proteome, searches allowed for variable oxidation of methionine (+15.9949 *m/z*) and static modifications of cysteine residues (+57.0215 *m/z*; iodoacetamide alkylation). All studies maintained trypsin enzyme specificity filtered with no greater than two missed cleavages. The MS2 spectral assignment was restricted to a specified false-positive rate of 1%, and a minimum of two unique peptides was required for protein identifications. Quantification was based on the theoretical *m/z* of the individual TMTsixplex™ reporter ions as reported previously (34). Enrichment factor was defined as the mean (+)UV/(−)UV TMT ratio. Frequency distribution histograms of log2 values were generated using GraphPad Prism 7.0.

Western Blotting for Biotin-conjugated Protein Targets—750 μg of biotin-conjugated protein sample was resuspended via sonication in 500 μl of 25 mM NH_4HCO_3 and 6 M urea in water. Following that, 150 μl of 5% Triton X-100 in water, 50 μl of 10% SDS in water, and 1.5 μl of 0.5 M DTT were added. The samples were heated for 15 min at 65 °C. Insoluble debris was separated by centrifugation for 10 min at 14,000 × *g*. The supernatant was diluted to 1 ml with PBS, and 50 μl was removed for the input sample. An additional 5 ml of PBS containing 100 μl of 50% streptavidin-agarose resin (Thermo Scientific) was added. Biotinylated proteins were captured over resin overnight at 4 °C with mild agitation. The resin was first washed with 6 ml of 1% SDS in PBS and then 7 ml of 0.1 M urea in PBS followed by 10 ml of PBS. The resin underwent a final wash with 0.9 ml of PBS and then was resuspended in 100 μl of 2× SDS Laemmli buffer containing 100 mM DTT. Samples were then incubated with agitation at 37 °C for 30 min, centrifuged at 700 × *g* for 2 min, and heated for 15 min at 90 °C. 50 μl of 2× SDS Laemmli buffer containing 100 mM DTT was joined to the input sample and heated for 5 min at 90 °C. Samples were centrifuged at 14,000 × *g* for 10 min prior to electrophoresis using 4–15% SDS-polyacrylamide gels with 10 μl of each sample introduced into each well. Proteins were then transferred to PVDF membranes. The membranes were blocked for 1 h with 2.5% BSA in Tris-buffered saline containing 0.1% Tween 20 (v/v; TBST). Membranes were incubated with $GABA_A$ receptor subunit antibodies overnight at 4 °C. All antibodies for $GABA_A$ receptor subunits were purchased from Santa Cruz Biotechnology, Inc., and included rabbit or goat polyclonal α1 ((A-20) sc-31405), α3 ((J-23) sc-122603), β1((N-19) sc-7361), β2 ((C-20) sc-7362), and γ2 ((Q-18) sc-101963) antibodies and monoclonal β3 ((D-12) sc-376252) antibody. For $GABA_A$ receptor subunit analysis, membranes were washed three times with TBST prior to a 2-h incubation with appropriate HRP-conjugated secondary antibody at room temperature. All membranes were then washed twice with TBST and once with Tris-buffered saline (TBS) before being developed with Amersham Biosciences ECL select reagent and scanned. Only the net ratio of intensity-detected band(s) between 75 and 50 kDa was considered. The elution intensities were normalized to the corresponding input sample. Samples showing no detectable band elution were set to a net ratio of intensity of 0. Studies were conducted in quadruplicate and are represented as the fraction of the corresponding input.

Molecular Dynamics Simulations—A model of the $\alpha_1\beta_3\gamma_2$ $GABA_A$ receptor was built by mutating 31 residues in the β subunits from an $\alpha_1\beta_1\gamma_2$ $GABA_A$ model 3 reported in Hénin *et al.* (35). The mutations were made using the MUTATOR plugin of VMD (67). AutoDock Vina (68) was used to generate initial coordinates for propofol; default parameters were used, and the search space included the entire pentamer. AutoDock Vina returned at least one pose for each subunit interface; the ligand conformation with the best score was chosen for each site. The complex ($GABA_A$ receptor and five propofol molecules) was then placed in a 109 × 109 Å phosphatidylcholine membrane aligned parallel to the *xy* plane using CHARMM-GUI membrane builder (69). The system was solvated to a total height in *z* of 139 Å, followed by the addition of sodium and potassium ions that neutralized the system and brought the salt concentration to 0.15 M. The complete simulation system contained about 167,000 atoms.

The CHARMM36 force field was used for protein (70, 71) and phospholipid (72) parameters, with parameters for TIP3P waters (73) and ions (74) corresponding to those traditionally used with CHARMM-based force fields. Propofol parameters relied on atom types from CHARMM36, as described in LeBard *et al.* (75), further parameterization and use of a CMAP potential was required to accurately enforce coupling between rotation of the hydroxyl and isopropyl groups due to steric clashes.

Atomistic molecular dynamics simulations were run with NAMD version 2.10 (76). All simulations used periodic boundary conditions and particle mesh Ewald (PME) electrostatics. Interactions between non-bonded atoms were cut off at 12 Å, and bonds involving hydrogen were constrained using the SHAKE/RATTLE algorithm. A Langevin thermostat and barostat were used to maintain a temperature and pressure of 300 K and 1 atm, respectively, and vanishing surface tension was imposed. The simulation time step was 2 fs. Following the system generation, 30,000 minimization steps and a 7-ns

Downloaded from http://www.jbc.org/ at Rutgers University on April 15, 2018

equilibration protocol that gradually softened restraints on the protein and ligand were run. Subsequently, we ran a 200-ns production run with soft harmonic restraints on the Cα atoms ($k = 0.5$ kcal/mol/Å^2). The probability of hydrogen bonding was calculated using a VMD script that measured the fraction of frames in which propofol was hydrogen bonding to any residue in the site, detected using the VMD geometric criterion with a distance cutoff of 3.3 Å and an angle cutoff of 40°. The first 50 ns of the production run were not included in the analysis.

Binding affinities were calculated using the AFEP method, a theoretically exact method that involves gradually decoupling (reducing interaction strength) the ligand and the binding site throughout an MD simulation (44, 77). The decoupling free energy was then corrected by the ligand solvation free energy, as well as the entropic cost of transferring the ligand from the available volume per molecule in the standard state (1,660 Å^3) to the volume of the ligand-binding site, yielding the standard Gibbs free energy of binding, ΔG^0. The dissociation constant K_D was calculated using the relationship $K_D = \exp(-\Delta G^0/RT)$. Implementation of the method was very closely based on the procedure used by LeBard *et al.* (75) for propofol binding to intrasubunit site transmembrane domains of *Gloeobacter* ligand-gated ion channel. Decoupling of propofol from each of four interfaces was carried out in four separate simulations, over 24 windows, with 1 ns/window for a total of 24 ns per interfacial binding site.

The probability of propofol hydrogen bond formation (P_{hb}) was estimated by calculating the frequency that a single hydrogen bond with the propofol hydroxyl was detected over the course of the equilibrium MD simulation. Molecular images in Figs. 6, *A* and *C–E,* and 7 were generated using VMD (67), and the data in Fig. 6*B* was plotted and fit using python scripts.

Statistics—GraphPad Prism 7.0, ChemDraw Professional 15.0, and Microsoft Excel, unless otherwise noted, were used for figure preparation and statistical data analysis.

Supplemental Material—^{1}H, ^{13}C, and ^{19}F NMR spectra and detailed synthetic methods of AziP*m-click* (**1**) are presented in supplemental S2–S32. The identified propofol-specific proteome is presented in supplemental Table 1.

Author Contributions—K. A. W., X. W., B. A. G., J. H., G. B., S. M., R. S., R. G. E., M. C., and W. P. D. participated in research design. K. A. W., J. H., B. J. P., X. W., S. M., W. P. D., and R. S. conducted the experiments. X. W., B. A. G., G. B., R. S., S. M., J. H., W. P. D., and B. J. P. contributed new reagents or analytic tools. K. A. W., X. W., G. B., S. M., J. H., W. P. D., and R. S. performed data analysis. K. A. W., X. W., B. A. G., J. H., G. B., S. M., R. G. E., M. C., and W. P. D. wrote or contributed to the writing of the manuscript.

Acknowledgments—We thank Robert Pearce (University of Wisconsin) and Qiansheng Liang (Thomas Jefferson University) for $GABA_A$ receptor constructs and assistance with oocyte electrophysiology.

References

1. Olsen, R. W., and Sieghart, W. (2008) International union of pharmacology. LXX. Subtypes of γ-aminobutyric acid(A) receptors: classification on the basis of subunit composition, pharmacology, and function. Update. *Pharmacol. Rev.* **60,** 243–260
2. Wu, X., Wu, Z., Ning, G., Guo, Y., Ali, R., Macdonald, R. L., De Blas, A. L., Luscher, B., and Chen, G. (2012) γ-Aminobutyric acid type A (GABA A) receptor α subunits play a direct role in synaptic *versus* extrasynaptic targeting. *J. Biol. Chem.* **287,** 27417–27430
3. Hentschke, H., Benkwitz, C., Banks, M. I., Perkins, M. G., Homanics, G. E., and Pearce, R. A. (2009) Altered GABAA, slow inhibition and network oscillations in mice lacking the GABAA receptor β3 subunit. *J. Neurophysiol.* **102,** 3643–3655
4. Kullmann, D. M., Ruiz, A., Rusakov, D. M., Scott, R., Semyanov, A., and Walker, M. C. (2005) Presynaptic, extrasynaptic and axonal GABA(A) receptors in the CNS: where and why? *Prog. Biophys. Mol. Biol.* **87,** 33–46
5. Baumann, S. W., Baur, R., and Sigel, E. (2001) Subunit arrangement of γ-aminobutyric acid type A receptors. *J. Biol. Chem.* **276,** 36275–36280
6. Baumann, S. W., Baur, R., and Sigel, E. (2002) Forced subunit assembly in α1β2γ2 GABAA receptors. Insight into the absolute arrangement. *J. Biol. Chem.* **277,** 46020–46025
7. Baur, R., Minier, F., and Sigel, E. (2006) A GABA(A) receptor of defined subunit composition and positioning: concatenation of five subunits. *FEBS Lett.* **580,** 1616–1620
8. Luscher, B., Fuchs, T., and Kilpatrick, C. L. (2011) GABA(A)R trafficking-mediated plasticity of inhibitory synapses. *Neuron* **70,** 385–409
9. Olsen, R. W., and Li, G. D. (2011) GABA(A) receptors as molecular targets of general anesthetics: identification of binding sites provides clues to allosteric modulation. *Can. J. Anaesth.* **58,** 206–215
10. Zecharia, A. Y., Nelson, L. E., Gent, T. C., Schumacher, M., Jurd, R., Rudolph, U., Brickley, S. G., Maze, M., and Franks, N. P. (2009) The involvement of hypothalamic sleep pathways in general anesthesia: testing the hypothesis using the GABAA receptor β3N265M knock-in mouse. *J. Neurosci.* **29,** 2177–2187
11. Sanchis-Segura, C., Cline, B., Jurd, R., Rudolph, U., and Spanagel, R. (2007) Etomidate and propofol-hyposensitive GABAA receptor β3(N265M) mice show little changes in acute alcohol sensitivity but enhanced tolerance and withdrawal. *Neurosci. Lett.* **416,** 275–278
12. Eckle, V. S., Rudolph, U., Antkowiak, B., and Grasshoff, C. (2015) Propofol modulates phasic and tonic GABAergic currents in spinal ventral horn interneurones. *Br. J. Anaesth.* **114,** 491–498
13. McDougall, S. J., Bailey, T. W., Mendelowitz, D., and Andresen, M. C. (2008) Propofol enhances both tonic and phasic inhibitory currents in second-order neurons of the solitary tract nucleus (NTS). *Neuropharmacology* **54,** 552–563
14. Nishikawa, K. (2011) Roles of glutamatergic and GABAergic nervous system in hypnotic and analgesic actions of general anesthetics. *Masui* **60,** 534–543
15. Chang, C. S., Olcese, R., and Olsen, R. W. (2003) A single M1 residue in the β2 subunit alters channel gating of GABAA receptor in anesthetic modulation and direct activation. *J. Biol. Chem.* **278,** 42821–42828
16. Eaton, M. M., Cao, L. Q., Chen, Z., Franks, N. P., Evers, A. S., and Akk, G. (2015) Mutational analysis of the putative high-affinity propofol-binding site in human β3 homomeric GABAA receptors. *Mol. Pharmacol.* **88,** 736–745
17. Krasowski, M. D., Nishikawa, K., Nikolaeva, N., Lin, A., and Harrison, N. L. (2001) Methionine 286 in transmembrane domain 3 of the GABAA receptor β subunit controls a binding cavity for propofol and other alkylphenol general anesthetics. *Neuropharmacology* **41,** 952–964
18. Jonsson Fagerlund, M., Sjödin, J., Krupp, J., and Dabrowski, M. A. (2010) Reduced effect of propofol at human α1β2(N289M)γ2 and αβ3(N290M)γ2 mutant GABA(A) receptors. *Br. J. Anaesth.* **104,** 472–481
19. Jayakar, S. S., Zhou, X., Chiara, D. C., Dostalova, Z., Savechenkov, P. Y., Bruzik, K. S., Dailey, W. P., Miller, K. W., Eckenhoff, R. G., and Cohen, J. B. (2014) Multiple propofol-binding sites in a γ-aminobutyric acid type A receptor (GABAAR) identified using a photoreactive propofol analog. *J. Biol. Chem.* **289,** 27456–27468
20. Krasowski, M. D., Hong, X., Hopfinger, A. J., and Harrison, N. L. (2002) 4D-QSAR analysis of a set of propofol analogues: mapping binding sites

Downloaded from http://www.jbc.org/ at Rutgers University on April 15, 2018

for an anesthetic phenol on the GABA(A) receptor. *J. Med. Chem.* **45,** 3210–3221

21. Krasowski, M. D., Jenkins, A., Flood, P., Kung, A. Y., Hopfinger, A. J., and Harrison, N. L. (2001) General anesthetic potencies of a series of propofol analogs correlate with potency for potentiation of γ-aminobutyric acid (GABA) current at the GABA(A) receptor but not with lipid solubility. *J. Pharmacol. Exp. Ther.* **297,** 338–351
22. Olsen, R. W. (2015) Allosteric ligands and their binding sites define γ-aminobutyric acid (GABA) type A receptor subtypes. *Adv. Pharmacol.* **73,** 167–202
23. Bertaccini, E. J., Yoluk, O., Lindahl, E. R., and Trudell, J. R. (2013) Assessment of homology templates and an anesthetic-binding site within the γ-aminobutyric acid receptor. *Anesthesiology* **119,** 1087–1095
24. León, I., Millán, J., Cocinero, E. J., Lesarri, A., Castaño, F., and Fernández, J. A. (2012) Mimicking anaesthetic-receptor interaction: a combined spectroscopic and computational study of propofol.phenol. *Phys. Chem. Chem. Phys.* **14,** 8956–8963
25. Jiang, W., Phillips, J. C., Huang, L., Fajer, M., Meng, Y., Gumbart, J. C., Luo, Y., Schulten, K., and Roux, B. (2014) Generalized scalable multiple copy algorithms for molecular dynamics simulations in NAMD. *Comput. Phys. Commun.* **185,** 908–916
26. Weyermann, P., Gisselbrecht, J. P., Boudon, C., Diederich, F., and Gross, M. (1999) Dendritic iron porphyrins with tethered axial ligands: new model compounds for cytochromes. *Angew. Chem. Int. Ed. Engl.* **38,** 3215–3219
27. Breton, G. W. (1997) Selective monoacetylation of unsymmetrical diols catalyzed by silica gel-supported sodium hydrogen sulfate. *J. Org. Chem.* **62,** 8952–8954
28. Lea, W. A., Xi, J., Jadhav, A., Lu, L., Austin, C. P., Simeonov, A., and Eckenhoff, R. G. (2009) A high-throughput approach for identification of novel general anesthetics. *PLoS ONE* **4,** e7150
29. Hall, M. A., Xi, J., Lor, C., Dai, S., Pearce, R., Dailey, W. P., and Eckenhoff, R. G. (2010) m-Azipropofol (AziPm) a photoactive analogue of the intravenous general anesthetic propofol. *J. Med. Chem.* **53,** 5667–5675
30. McKinstry-Wu, A. R., Bu, W., Rai, G., Lea, W. A., Weiser, B. P., Liang, D. F., Simeonov, A., Jadhav, A., Maloney, D. J., and Eckenhoff, R. G. (2012) *Discovery of Novel General Anesthetic Chemotype Using High-throughput Screening. Anesthesiology* **122,** 325–333
31. Vedula, L. S., Brannigan, G., Economou, N. J., Xi, J., Hall, M. A., Liu, R., Rossi, M. J., Dailey, W. P., Grasty, K. C., Klein, M. L., Eckenhoff, R. G., and Loll, P. J. (2009) A unitary anesthetic-binding site at high resolution. *J. Biol. Chem.* **284,** 24176–24184
32. Liu, R., Loll, P. J., and Eckenhoff, R. G. (2005) Structural basis for high-affinity volatile anesthetic binding in a natural 4-helix bundle protein. *FASEB J.* **19,** 567–576
33. Weiser, B. P., Kelz, M. B., and Eckenhoff, R. G. (2013) *In vivo* activation of azipropofol prolongs anesthesia and reveals synaptic targets. *J. Biol. Chem.* **288,** 1279–1285
34. Ting, L., Rad, R., Gygi, S. P., and Haas, W. (2011) MS3 eliminates ratio distortion in isobaric multiplexed quantitative proteomics. *Nat. Methods* **8,** 937–940
35. Hénin, J., Salari, R., Murlidaran, S., and Brannigan, G. (2014) A predicted binding site for cholesterol on the GABAA receptor. *Biophys. J.* **106,** 1938–1949
36. Zwanzig, R. W. (1954) High-temperature equation of state by a perturbation method. 1. Nonpolar gases. *J. Chem. Phys.* **22,** 1420–1426
37. Hibbs, R. E., and Gouaux, E. (2011) Principles of activation and permeation in an anion-selective Cys-loop receptor. *Nature* **474,** 54–60
38. Miller, P. S., and Aricescu, A. R. (2014) Crystal structure of a human GABAA receptor. *Nature* **512,** 270–275
39. Westergard, T., Salari, R., Martin, J. V., and Brannigan, G. (2015) Correction: interactions of L-3,5,3′-triiodothyronine, allopregnanolone, and ivermectin with the GABAA receptor: evidence for overlapping intersubunit binding modes. *PLoS ONE* **10,** e0142514
40. Woll, K. A., Weiser, B. P., Liang, Q., Meng, T., McKinstry-Wu, A., Pinch, B., Dailey, W. P., Gao, W. D., Covarrubias, M., and Eckenhoff, R. G. (2015) Role for the propofol hydroxyl in anesthetic protein target molecular recognition. *ACS Chem. Neurosci.* **6,** 927–935
41. Weiser, B. P., Woll, K. A., Dailey, W. P., and Eckenhoff, R. G. (2014) Mechanisms revealed through general anesthetic photolabeling. *Curr. Anesth. Rep.* **4,** 57–66
42. Yip, G. M., Chen, Z. W., Edge, C. J., Smith, E. H., Dickinson, R., Hohenester, E., Townsend, R. R., Fuchs, K., Sieghart, W., Evers, A. S., and Franks, N. P. (2013) A propofol-binding site on mammalian GABA receptors identified by photolabeling. *Nat. Chem. Biol.* **9,** 715–720
43. Stewart, D. S., Savechenkov, P. Y., Dostalova, Z., Chiara, D. C., Ge, R., Raines, D. E., Cohen, J. B., Forman, S. A., Bruzik, K. S., and Miller, K. W. (2011) *p*-(4-Azipentyl)propofol: a potent photoreactive general anesthetic derivative of propofol. *J. Med. Chem.* **54,** 8124–8135
44. Woo, H.-J., and Roux, B. (2005) Calculation of absolute protein-ligand binding free energy from computer simulations. *Proc. Natl. Acad. Sci. U.S.A.* **102,** 6825–6830
45. Fang, C., Deng, L., Keller, C. A., Fukata, M., Fukata, Y., Chen, G., and Lüscher, B. (2006) GODZ-mediated palmitoylation of GABA(A) receptors is required for normal assembly and function of GABAergic inhibitory synapses. *J. Neurosci.* **26,** 12758–12768
46. Keller, C. A., Yuan, X., Panzanelli, P., Martin, M. L., Alldred, M., Sassoè-Pognetto, M., and Lüscher, B. (2004) The γ2 subunit of GABA(A) receptors is a substrate for palmitoylation by GODZ. *J. Neurosci.* **24,** 5881–5891
47. Nymann-Andersen, J., Wang, H., Chen, L., Kittler, J. T., Moss, S. J., and Olsen, R. W. (2002) Subunit specificity and interaction domain between GABA(A) receptor-associated protein (GABARAP) and GABA(A) receptors. *J. Neurochem.* **80,** 815–823
48. Maldifassi, M. C., Baur, R., and Sigel, E. (2016) Functional sites involved in modulation of the GABA receptor channel by the intravenous anesthetics propofol, etomidate and pentobarbital. *Neuropharmacology* **105,** 207–214
49. Olsen, R. W., Li, G. D., Wallner, M., Trudell, J. R., Bertaccini, E. J., Lindahl, E., Miller, K. W., Alkana, R. L., and Davies, D. L. (2014) Structural models of ligand-gated ion channels: sites of action for anesthetics and ethanol. *Alcohol Clin. Exp. Res.* **38,** 595–603
50. Hill-Venning, C., Belelli, D., Peters, J. A., and Lambert, J. J. (1997) Subunit-dependent interaction of the general anaesthetic etomidate with the γ-aminobutyric acid type A receptor. *Br. J. Pharmacol.* **120,** 749–756
51. Orser, B. A., Wang, L. Y., Pennefather, P. S., and MacDonald, J. F. (1994) Propofol modulates activation and desensitization of GABAA receptors in cultured murine hippocampal neurons. *J. Neurosci.* **14,** 7747–7760
52. Mowrey, D., Cheng, M. H., Liu, L. T., Willenbring, D., Lu, X., Wymore, T., Xu, Y., and Tang, P. (2013) Asymmetric ligand binding facilitates conformational transitions in pentameric ligand-gated ion channels. *J. Am. Chem. Soc.* **135,** 2172–2180
53. James, R., and Glen, J. B. (1980) Synthesis, biological evaluation, and preliminary structure-activity considerations of a series of alkylphenols as intravenous anesthetic agents. *J. Med. Chem.* **23,** 1350–1357
54. Grasshoff, C., Rudolph, U., and Antkowiak, B. (2005) Molecular and systemic mechanisms of general anaesthesia: the "multi-site and multiple mechanisms" concept. *Curr. Opin. Anaesthesiol.* **18,** 386–391
55. Szychowski, J., Mahdavi, A., Hodas, J. J., Bagert, J. D., Ngo, J. T., Landgraf, P., Dieterich, D. C., Schuman, E. M., and Tirrell, D. A. (2010) Cleavable biotin probes for labeling of biomolecules via azide-alkyne cycloaddition. *J. Am. Chem. Soc.* **132,** 18351–18360
56. Weiser, B. P., Bu, W., Wong, D., and Eckenhoff, R. G. (2014) Sites and functional consequence of VDAC alkylphenol anesthetic interactions. *FEBS Lett.* **588,** 4398–4403
57. Eckenhoff, R. G., Xi, J., and Dailey, W. P. (2010) Inhalational anesthetic photolabeling. *Methods Mol. Biol.* **617,** 437–443
58. Herring, B. E., McMillan, K., Pike, C. M., Marks, J., Fox, A. P., and Xie, Z. (2011) Etomidate and propofol inhibit the neurotransmitter release machinery at different sites. *J. Physiol.* **589,** 1103–1115
59. Orser, B. A., Bertlik, M., Wang, L. Y., and MacDonald, J. F. (1995) Inhibition by propofol-(2.6-di-isopropylphenol) of the *N*-methyl-D-aspartate subtype of glutamate receptor in cultured hippocampal-neurons. *Br. J. Pharmacol.* **116,** 1761–1768
60. Tibbs, G. R., Rowley, T. J., Sanford, R. L., Herold, K. F., Proekt, A., Hemmings, H. C., Jr., Andersen, O. S., Goldstein, P. A., and Flood, P. D. (2013)

Downloaded from http://www.jbc.org/ at Rutgers University on April 15, 2018

HCN1 channels as targets for anesthetic and nonanesthetic propofol analogs in the amelioration of mechanical and thermal hyperalgesia in a mouse model of neuropathic pain. *J. Pharmacol. Exp. Ther.* **345,** 363–373
61. Fassl, J., High, K. M., Stephenson, E. R., Yarotskyy, V., and Elmslie, K. S. (2011) The intravenous anesthetic propofol inhibits human L-type calcium channels by enhancing voltage-dependent inactivation. *J. Clin. Pharmacol.* **51,** 719–730
62. Barber, A. F., Liang, Q., and Covarrubias, M. (2012) Novel activation of voltage-gated K(+) channels by sevoflurane. *J. Biol. Chem.* **287,** 40425–40432
63. Frisch, M. J., Trucks, G. W., Schlegel, H. B., Scuseria, G. E., Robb, M. A., Cheeseman, J. R., Scalmani, G., Barone, V., Mennucci, B., Petersson, G. A., Nakatsuji, H., Caricato, M., Li, X., Hratchian, H. P., Izmaylov, A. F., *et al.* (2009) Gaussian 09, Revision D.01, Wallingford, CT
64. Butts, C. A., Xi, J., Brannigan, G., Saad, A. A., Venkatachalan, S. P., Pearce, R. A., Klein, M. L., Eckenhoff, R. G., and Dmochowski, I. J. (2009) Identification of a fluorescent general anesthetic, 1-aminoanthracene. *Proc. Natl. Acad. Sci. U.S.A.* **106,** 6501–6506
65. Hirata, K., Akita, Y., Povalko, N., Nishioka, J., Yatsuga, S., Matsuishi, T., and Koga, Y. (2008) Effect of L-arginine on synaptosomal mitochondrial function. *Brain Dev.* **30,** 238–245
66. Villén, J., and Gygi, S. P. (2008) The SCX/IMAC enrichment approach for global phosphorylation analysis by mass spectrometry. *Nat. Protoc.* **3,** 1630–1638
67. Humphrey, W., Dalke, A., and Schulten, K. (1996) VMD: visual molecular dynamics. *J. Mol. Graph.* **14,** 27–28
68. Trott, O., and Olson, A. J. (2010) Software news and update autodock vina: improving the speed and accuracy of docking with a new scoring function, efficient optimization, and multithreading. *J. Comput. Chem.* **31,** 455–461
69. Jo, S., Lim, J. B., Klauda, J. B., and Im, W. (2009) CHARMM-GUI membrane builder for mixed bilayers and its application to yeast membranes. *Biophys. J.* **97,** 50–58
70. Best, R. B., Mittal, J., Feig, M., and MacKerell, A. D. (2012) Inclusion of many-body effects in the additive CHARMM protein CMAP potential results in enhanced cooperativity of α-helix and β-hairpin formation. *Biophys. J.* **103,** 1045–1051
71. MacKerell, A. D., Bashford, D., Bellott, M., Dunbrack, R. L., Evanseck, J. D., Field, M. J., Fischer, S., Gao, J., Guo, H., Ha, S., Joseph-McCarthy, D., Kuchnir, L., Kuczera, K., Lau, F. T., Mattos, C., *et al.* (1998) All-atom empirical potential for molecular modeling and dynamics studies of proteins. *J. Phys. Chem. B.* **102,** 3586–3616
72. Klauda, J. B., Venable, R. M., Freites, J. A., O'Connor, J. W., Tobias, D. J., Mondragon-Ramirez, C., Vorobyov, I., MacKerell, A. D., Jr., and Pastor, R. W. (2010) Update of the CHARMM all-atom additive force field for lipids: Validation on six lipid types. *J. Phys. Chem. B.* **114,** 7830–7843
73. Jorgensen, W. L., Chandrasekhar, J., Madura, J. D., Impey, R. W., and Klein, M. L. (1983) Comparison of simple potential functions for simulating liquid water. *J. Chem. Phys.* **79,** 926–935
74. Beglov, D., and Roux, B. (1994) Finite representation of an infinite bulk system: solvent boundary potential for computer simulations. *J. Chem. Phys.* **100,** 9050
75. LeBard, D. N., Hénin, J., Eckenhoff, R. G., Klein, M. L., and Brannigan, G. (2012) General anesthetics predicted to block the GLIC pore with micromolar affinity. *PLoS Comput. Biol.* **8,** e1002532
76. Phillips, J. C., Braun, R., Wang, W., Gumbart, J., Tajkhorshid, E., Villa, E., Chipot, C., Skeel, R. D., Kalé, L., and Schulten, K. (2005) Scalable molecular dynamics with NAMD. *J. Comput. Chem.* **26,** 1781–1802
77. Gilson, M. K., Given, J. A., Bush, B. L., and McCammon, J. A. (1997) The statistical-thermodynamic basis for computation of binding affinities: a critical review. *Biophys. J.* **72,** 1047–1069

Downloaded from http://www.jbc.org/ at Rutgers University on April 15, 2018

Bibliography

Adodra, S., & Hales, T. G. 1995, Department of Anesthesiology, 953

Althoff, T., Hibbs, R. E., Banerjee, S., & Gouaux, E. 2014a, Nature, 512, 333

—. 2014b, Nature, 512, 333

Anahita Nourmahnad, B.S.1,*, Alex T Stern, B.S.1,*, a, Mayo Hotta, B.S.1, a, Deirdre S. Stewart, Ph.D.1, Alexis M. Ziemba, B.A.1, b, Andrea Szabo, B.S.1, and Stuart A. Forman, M.D., P. 2017, 125, 1144

Antkowiak, B. 2001, Naturwissenschaften, 88, 201

Bali, M., & Akabas, M. H. 2004a, Molecular pharmacology, 65, 68

—. 2004b, Molecular pharmacology, 65, 68

Baulac, S., Huberfeld, G., Gourfinkel-An, I., et al. 2001, Nature genetics, 28, 46

Baumann, S. W., Baur, R., & Sigel, E. 2002, J Biol Chem, 277, 46020

Belelli, D., & Lambert, J. J. 2005, Nat Rev Neurosci, 6, 565

Belelli, D., Pistis, M., Peters, J. A., & Lambert, J. J. 1999a, General anaesthetic action at transmitter-gated inhibitory amino acid receptors, doi:10.1016/S0165-6147(99)01405-4

—. 1999b, Neurochem. Int., 34, 447

Beveridge, D. L., & DiCapua, F. M. 1989, Annual Review of Biophysics and Biophysical Chemistry, 18, 431

Bhattacharya, A. A., Curry, S., & Franks, N. P. 2000a, J. Biol. Chem., 275, 38731

Bhattacharya, a. a., Curry, S., & Franks, N. P. 2000b, The Journal of biological chemistry, 275, 38731

Bianchi, M. T., & Song, L. 2002, The Journal of . . . , 22, 5321

Bocquet, N., Nury, H., Baaden, M., et al. 2009, Nature, 457, 111

Bocquet, N., Prado de Carvalho, L., Cartaud, J., et al. 2007, Nature, 445, 116

Boresch, S., Tettinger, F., Leitgeb, M., & Karplus, M. 2003, The Journal of Physical Chemistry B, 107, 9535

Brannigan, G., Hénin, J., Law, R., Eckenhoff, R., & Klein, M. L. 2008, Proc. Natl. Acad. Sci. USA, 105, 14418

Brannigan, G., LeBard, D. N., Hénin, J., Eckenhoff, R. G., & Klein, M. L. 2010, Proceedings of the National Academy of Sciences of the United States of America, 107, 14122

Brejc, K., Van Dijk, W. J., Klaassen, R. V., et al. 2001, Nature, 411, 269

Brooks, B. R., Brooks, C. L., Mackerell, A. D., et al. 2009, Journal of Computational Chemistry, 30, 1545

Calimet, N., Simoes, M., Changeux, J.-P., et al. 2013, Proceedings of the National Academy of Sciences, 110, E3987

Callenberg, K. M., Choudhary, O. P., de Forest, G. L., et al. 2010, PLoS ONE, 5, doi:10.1371/journal.pone.0012722

Campos-Caro, a., Sala, S., Ballesta, J. J., et al. 1996, Proceedings of the National Academy of Sciences of the United States of America, 93, 6118

Chang, Y., Wang, R., Barot, S., & Weiss, D. S. 1996, The Journal of neuroscience : the official journal of the Society for Neuroscience, 16, 5415

Changeux, J.-P., & Christopoulos, A. 2016, Cell, 166, 1084

Changeux, J.-P., & Edelstein, S. 2011, F1000 biology reports, 3

Chen, Q., Kinde, M. N., Arjunan, P., et al. 2015, Scientific Reports, 5, 13833

Cheng, M. H., Coalson, R. D., & Tang, P. 2010, Journal of the American Chemical Society, 132, 16442

Chiara, D. C., Jayakar, S. S., Zhou, X., et al. 2013, The Journal of biological chemistry, 288, 19343

Chiara, D. C., Jounaidi, Y., Zhou, X., et al. 2016, Journal of Biological Chemistry, jbc.M116.753335

Collins, J. G., Kendig, J. J., & Mason, P. 1995, Anesthetic actions within the spinal cord: contributions to the state of general anesthesia, doi:10.1016/0166-2236(95)98377-B

Comer, J., Gumbart, J. C., Hénin, J., et al. 2014, The journal of physical chemistry. B, doi:10.1021/jp506633n

Darve, E., Rodríguez-Gómez, D., & Pohorille, A. 2008, The Journal of chemical physics, 128, 144120

Deng, Y., & Roux, B. 2009, J. Phys. Chem. B, 113, 1

Dilger, J. P., Brett, R. S., & Mody, H. I. 1993, Mol. Pharmacol., 44, 1056

Dolinsky, T. J., Czodrowski, P., Li, H., et al. 2007, Nucleic acids research, 35, W522

Du, J., Lü, W., Wu, S., Cheng, Y., & Gouaux, E. 2015, Nature, 526, 224

Eugène, E., Depienne, C., Baulac, S., et al. 2007, The Journal of neuroscience : the official journal of the Society for Neuroscience, 27, 14108

Farrar, S. J., Whiting, P. J., Bonnert, T. P., & McKernan, R. M. 1999, Journal of Biological Chemistry, 274, 10100

Fiorin, G., Klein, M. L., & Hénin, J. 2013, Molecular Physics, 111, 3345

Forman, S. A., Miller, K. W., & Yellen, G. 1995, Molecular Pharmacology, 48, 574 LP

Franks, N., Jenkins, A., Conti, E., Lieb, W., & Brick, P. 1998, Biophysical Journal, 75, 2205

Franks, N., & Lieb, W. 1996, Temperature dependence of the potency of volatile general anesthetics: implications for in vitro experiments., doi:10.1097/00000542-199603000-00027

Franks, N. P., & Lieb, W. R. 1984, Nature, 310, 599

—. 1994, Nature, 367, 607

Fritsch, S., Ivanov, I., Wang, H., & Cheng, X. 2011, Biophysical Journal, 100, 390

Git, V., Bernardi, R., Bhandarkar, M., et al. 2017

Gonzalez-Gutierrez, G., Cuello, L. G., Nair, S. K., & Grosman, C. 2013, Proceedings of the National Academy of Sciences, 110, 18716

Grosman, C., Salamone, F. N., Sine, S. M., & Auerbach, A. 2000, The Journal of general physiology, 116, 327

Gupta, S., Chakraborty, S., Vij, R., & Auerbach, A. 2017, The Journal of General Physiology, 149, 85

Hales, T. G., Deeb, T. Z., Tang, H., et al. 2006, The Journal of biological chemistry, 281, 17034

Hales, T. G., & Lambert, J. J. 1991, British Journal of Pharmacology, 104, 619

Harris, R. A., Mihic, S. J., Dildy-Mayfield, J. E., & Machu, T. K. 1995a, FASEB J, 9, 1454

—. 1995b, The FASEB journal : official publication of the Federation of American Societies for Experimental Biology, 9, 1454

Hassaine, G., Deluz, C., Grasso, L., et al. 2014, Nature, 512, 276

Hénin, J., & Chipot, C. 2004, The Journal of chemical physics, 121, 2904

Hénin, J., Salari, R., Murlidaran, S., Brannigan, G., & Biology, I. 2014, Biophysical journal, 106, 1938

Hibbs, R. E., & Gouaux, E. 2011a, Nature, 474, 54

—. 2011b, Nature, 474, 54

—. 2011c, Nature, 474, 54

Hilf, R. J., & Dutzler, R. 2009, Nature, 457, 115

Hilf, R. J. C., & Dutzler, R. 2008a, Nature, 452, 375

—. 2008b, Nature, 452, 375

Humphrey, W., Dalke, A., & Schulten, K. 1996, Journal of molecular graphics, 14, 33

Isralewitz, B., Baudry, J., Gullingsrud, J., Kosztin, D., & Schulten, K. 2001, Journal of Molecular Graphics and Modelling, 19, 13

Ivanov, I., Cheng, X., Sine, S. M., & McCammon, J. A. 2007, Journal of the American Chemical Society, 129, 8217

Jaiteh, M., Taly, A., & Hénin, J. 2016, PLOS ONE, 11, e0151934

Jarzynski, C. 1997a, Physical Review E, 56, 5018

—. 1997b, Physical Review Letters, 78, 2690

Jayakar, S. S., Zhou, X., Chiara, D. C., et al. 2014a, The Journal of biological chemistry, 289, 27456

—. 2014b, The Journal of biological chemistry, 289, 27456

Jenkins, A., Franks, N. P., & Lieb, W. R. 1999, Anesthesiology, 90, 484

Jo, S., Lim, J. B., Klauda, J. B., & Im, W. 2009, Biophys J, 97, 50

John Mihic, S., Ye, Q., Wick, M. J., et al. 1997, Nature, 389, 385

Jurd, R., Arras, M., Lambert, S., et al. 2002, The FASEB Journal, 17, 250

—. 2003, The FASEB journal : official publication of the Federation of American Societies for Experimental Biology, 17, 250

Kang, J.-Q., Shen, W., & Macdonald, R. L. 2006, The Journal of neuroscience : the official journal of the Society for Neuroscience, 26, 2590

Kash, T. L., Jenkins, A., Kelley, J. C., Trudell, J. R., & Harrison, N. L. 2003, Nature, 421, 272

Klauda, J. B., Venable, R. M., Freites, J. A., et al. 2010, The journal of physical chemistry. B, 114, 7830

Krasowski, M. D., & Harrison, N. L. 1999, Cell. Mol. Life Sci., 55, 1278

Krasowski, M. D., Jenkins, A., Flood, P., et al. 2001a, The Journal of pharmacology and experimental therapeutics, 297, 338

Krasowski, M. D., Nishikawa, K., Nikolaeva, N., Lin, A., & Harrison, N. L. 2001b, Neuropharmacology, 41, 952

LeBard, D. N., Hénin, J., Eckenhoff, R. G., Klein, M. L., & Brannigan, G. 2012a, PLoS computational biology, 8, e1002532

—. 2012b, PLoS computational biology, 8, e1002532

Lee, W. Y., Free, C. R., & Sine, S. M. 2009, The Journal of neuroscience : the official journal of the Society for Neuroscience, 29, 3189

Lee, W. Y., & Sine, S. M. 2005, Nature, 438, 243

Lev, B., Murail, S., Poitevin, F., et al. 2017, Proceedings of the National Academy of Sciences, 114, E4158

Liu, R., Loll, P. J., & Eckenhoff, R. G. 2005, FASEB journal : official publication of the Federation of American Societies for Experimental Biology, 19, 567

Lummis, S. C. R., Beene, D. L., Lee, L. W., et al. 2005, Nature, 438, 248

Macdonald, R. 2010, The Journal of physiology

Macdonald, R. L., Kang, J.-Q., Gallagher, M. J., & Feng, H.-J. 2006, Adv Pharmacol, 54, 147

MacKerell, A. D., Bashford, D., Bellott, M., et al. 1998, The journal of physical chemistry. B, 102, 3586

Maldifassi, M. C., Baur, R., & Sigel, E. 2016, Neuropharmacology, 105, 207

Mark, A. E. 1998, in Encyclopedia of computational chemistry, Vol. 2 (Chichester, UK: John Wiley & Sons, Ltd), 1070–1083

Miller, K. W. 2002, Br. J. Anaesth., 89, 17

Miller, P. S., & Aricescu, A. R. 2014, Nature, 512, 270

Mitra, A., Cymes, G. D., & Auerbach, A. 2005, Proceedings of the National Academy of Sciences, 102, 15069

Mowrey, D., Cheng, M. H., Liu, L. T., et al. 2013, Journal of the American Chemical Society, 135, 2172

Murail, S., Wallner, B., Trudell, J. R., Bertaccini, E., & Lindahl, E. 2011, Biophys J, 100, 1642

Murlidaran, S., & Brannigan, G. 2018, Physical Accuracy Leads to Biological Relevance: Best Practices For Simulating Ligand-Gated Ion Channels Interacting With General Anesthetics, doi:10.1016/bs.mie.2018.02.001

Murlidaran, S., Salari, R., & Brannigan, G. ????

Nakahiro, M., Yeh, J. Z., Brunner, E., & Narahashi, T. 1989, FASEB J, 3, 1850

Nirthanan, S., Garcia, G., Chiara, D. C., Husain, S. S., & Cohen, J. B. 2008, Journal of Biological Chemistry, 283, 22051

Nishikawa, K., & Harrison, N. L. 2003, The Journal of the American Society of Anesthesiologists, 99, 678

Nury, H., Bocquet, N., Le Poupon, C., et al. 2010, Journal of molecular biology, 395, 1114

Nury, H., Van Renterghem, C., Weng, Y., et al. 2011, Nature, 469, 428

Orser, a., Pennefather, P. S., & Macdonald, J. F. 1994, The Journal of Neuroscience, 74, 7747

O'Shea, S. M., & Harrison, N. L. 2000, The Journal of biological chemistry, 275, 22764

Park, S., & Schulten, K. 2004, Journal of Chemical Physics, 120, 5946

Phillips, J. C., Braun, R., Wang, W., et al. 2005, Journal of computational chemistry, 26, 1781

Pitman, M. C., Suits, F., Mackerell, A. D., & Feller, S. E. 2004, Biochemistry, 43, 15318

Pohorille, A., Jarzynski, C., & Chipot, C. 2010, J Phys Chem B, 114, 10235

Raju, S. G., Barber, A. F., LeBard, D. N., Klein, M. L., & Carnevale, V. 2013, PLoS Computational Biology, 9, e1003090

Ramakrishnan, L., & Hess, G. P. 2004, Biochemistry, 43, 7534

Sanna, E., Garau, F., & Harris, R. A. 1995, Molecular Pharmacology, 47

Sauguet, L., Shahsavar, A., Poitevin, F., et al. 2014, Proceedings of the National Academy of Sciences, 111, 966

Sebel, L. E., Richardson, J. E., Singh, S. P., Bell, S. V., & Jenkins, A. 2006, The Journal of the American Society of Anesthesiologists, 104, 1176

Siegwart, R., Krähenbühl, K., Lambert, S., & Rudolph, U. 2003, BMC pharmacology, 3, 13

Sigel, E. 1997, Trends in Pharmacological Sciences, 18, 425

Sigel, E., & Buhr, A. 1997, Trends in Pharmacological Sciences, 18, 425

Sigel, E., & P. Luscher, B. 2011, Current Topics in Medicinal Chemistry, 11, 241

Sigel, ErwinBuhr, AndreasBaur, R. 1999, Journal of Neurochemistry. Oct99, 73

Smart, O. S., Neduvelil, J. G., Wang, X., Wallace, B. A., & Sansom, M. S. 1996, J Mol Graph, 14, 354

Spurny, R. Ramerstorfer, J. Price, K. Brams, M. Ernst, M. Nury, H. Verheij, M. Legrand, P., Bertrand, D. Bertrand, S. Dougherty, D.A. De Esch, I.J.P. Corringer, P. Sieghart, W., Lummis, S.C.R. Ulens, C. 2012, Proc.Natl.Acad.Sci.USA, 109, E3028

Stern, A. T., & Forman, S. A. 2016, Anesthesiology, 124, 89

Stewart, D. S., Pierce, D. W., Hotta, M., Stern, A. T., & Forman, S. A. 2014a, PloS one

—. 2014b, PLoS ONE, 9, e111470

Tanelian, D. L., Kosek, P., Mody, I., & MacIver, M. B. 1993, Anesthesiology, 78, 757

Tasneem, A., Iyer, L. M., Jakobsson, E., & Aravind, L. 2005, Genome biology, 6, R4

Trott, O., & Olson, A. J. 2010, J Comput. Chem., 31, 455

Unwin, N. 1995, Nature, 373, 37

—. 2005, J. Mol. Biol., 346, 967

Vedula, L. S., Brannigan, G., Economou, N. J., et al. 2009, The Journal of biological chemistry, 284, 24176

Wang, J., Deng, Y., & Roux, B. 2006, Biophysical Journal, 91, 2798

Willenbring, D., Liu, L., Mowrey, D., Xu, Y., & Tang, P. 2011, Biophys. J., 101, 1905

Woll, K. A., Murlidaran, S., Pinch, B. J., et al. 2016a, The Journal of biological chemistry, 291, 20473

—. 2016b, The Journal of biological chemistry, doi:10.1074/jbc.M116.736975

Wu, J., Harata, N., & Akaike, N. 1996, British journal of pharmacology, 119, 1013

Yamakura, T., Bertaccini, E., Trudell, J. R., & Harris, R. a. 2001, Annual review of pharmacology and toxicology, 41, 23

Yip, G. M. S., Chen, Z.-W., Edge, C. J., et al. 2013, Nature chemical biology, 9, 715

Yoluk, O., Brömstrup, T., Bertaccini, E. J., Trudell, J. R., & Lindahl, E. 2013, Biophys J, 105, 640

Zhu, F., & Hummer, G. 2010, Proceedings of the National Academy of Sciences of the United States of America, 107, 19814

Zwanzig, R. W. 1954, Journal of Chemical Physics, 22, 1420